Measurements of thermal properties of phonon bridge adhesion layers, nano-gaps and metal-organic frameworks using frequency-domain thermoreflectance (FDTR)

Submitted in partial fulfillment of the requirements for

the degree of

Doctor of Philosophy

in

Department of Materials Science and Engineering

Minyoung Jeong

B.S., Materials Science and Engineering, Michigan State University
M.S., Materials Science and Engineering, Michigan State University

Carnegie Mellon University
Pittsburgh, PA

August, 2018

Acknowledgements

It is my true pleasure and honor to present my four-year endeavor at Carnegie Mellon University in this thesis. I clearly remember the first day I met my advisor Professor Malen (Jon) at the departmental orientation seminar. We met again that afternoon and when I called him 'Professor Malen' politely as it was my first time seeing him in person, he said upfront, "Just call me Jon". That moment, I realized I met the best professor. I would like to give my sincere gratitude to my committee members Professor James A. Bain, Professor Lisa M. Porter and Professor Vincent M. Sokalski for guiding me up to this point. Also, I would like to acknowledge financial support from the National Science Foundation (NSF CBET 1403447), and the Data Storage Systems Center at Carnegie Mellon University with its associated members.

I enjoyed meeting and working with smart young talents at the Malen laboratory; Wee-liat; Keith; Shub; Justin; Kevin; Lili; William; Dipanjan; and Turga. I will miss my best friends at CMU; Ik-soo; Jaejun; Gunwoo; Dasheng; and Tim. I also appreciate all the prayers and support I got from my friends and pastors at Korea Central Church of Pittsburgh. Pastor Kanghoon Lee, I will never forget how encouraging and sympathetic you are to my family with your heart-warming prayers.

Finally, I would like to give my biggest and deepest gratitude to my family. First, to Mom and Dad. Without your unconditional sacrifice, this degree would have been impossible. As you are proud of me, I am proud of you. To my sister, Jihyun, I owe you more than anything you could ever know. Thank you for being with mom and dad physically and filling my absence in Korea. To my love, Youngeun, I truly appreciate your ongoing love, support and

encouragement. My life motto is “In their hearts humans plan their course, but the LORD establishes their steps”. In hindsight, those steps have been perfect, and I wish the best in my future journeys, too.

Abstract

Thermal conductance measurements across interfaces and nanostructured gaps for future heat-assisted magnetic recording technology and analysis of thermal conductivity change in metal-organic framework single crystals for adsorption applications

by

Minyoung Jeong

Chair : Jonathan A. Malen

To meet the continuing demand for smaller yet faster electronic devices, many of the components are packed closer together while they produce a significant amount of heat. If the generated heat keeps accumulating due to a lack of efficient thermal management, devastating effects such as thermal breakdown could occur. To enhance heat dissipation, higher thermal conductivity and thermal interface conductance are required. In Chapter 2, the effect of inserting thin metal adhesion layers of Cu and Cr between the Au (gold) - Al_2O_3 (sapphire) interface on thermal interface conductance for the heat-assisted magnetic recording (HAMR) application is investigated. It is found that without any adhesion layers, thermal interface conductance between Au and Al_2O_3 layers is approximately 65 ± 10 MW/m^{2}K. With the increasing thicknesses of Cu and Cr adhesion layers between Au and Al_2O_3, this value increases and saturates to 180 ± 20 MW/m^{2}K and 390 ± 70 MW/m^{2}K, respectively. A significant amount of enhancement in thermal interface conductance is observed for both metal adhesion layers even when they are less than 1-nm thick. This is beneficial in terms of reducing the material costs as well as preserving Au's original optical properties required for HAMR application.

Because HAMR heats the magnetic media via a near-field transducer (NFT) which flies above the media with a very short distance of 5 nanometers to locally heat the magnetic domains, the effect of near-field thermal radiation on overall performance of the NFT system is important to understand. Near-field thermal radiation is a phenomenon where the radiative thermal transfer exceeds the predicted blackbody limit with large contributions from evanescent modes generated either by total internal reflection and surface polaritons. The evanescent modes can participate in heat transfer only if the two bodies exchanging thermal energy are separated equal to or less than a given decay length. In Chapter 3, designs and fabrications of thermomechanically stable nanostructured gaps are presented. We successfully fabricate 10 nm and 50nm gaps sandwiched between SiO_2 – SiO_2 and Au-SiO_2 layers via mechanical pressing approach. The samples are heated with the modulated laser, and the heat transfer coefficients across the gap are measured. Based on the clear phase lag differences between the heating pump and temperature-measuring probe lasers in the pillar and the gap regions, it is concluded that the gap with the intended thicknesses did not collapse. Moreover, the fitted heat transfer coefficient values match reasonably well with the analytically predicted values; the 50 nm and 10 nm gaps sandwiched between the Au and SiO_2 layers yielded a value of $9.69 \pm 10.92 \times 10^4$ W/m^{2}K and $4.27 \pm 9.12 \times 10^4$, respectively, in the ambient environment. When the 10 nm gap is placed between the two matching SiO_2 plates, the heat transfer coefficient increases to $1.43 \pm 1.51 \times 10^5$ W/m^{2}K in the ambient environment, which clearly indicates the effect of near-field radiative heat transfer. The issue of large uncertainties involved in each data set is resolved by performing differential analysis for phase lags. Through this approach, we obtain $1.15 \pm 0.34 \times 10^5$ W/m^{2}K and $1.65 \pm 0.49 \times 10^5$ W/m^{2}K for the 10 nm Au-SiO_2 and 10 nm SiO_2-SiO_2 gap samples, respectively.

Not only electronics applications, but also other biological and chemical applications relying on adsorption and desorption of molecules also require faster heat transfer for improved performance because adsorption and desorption processes are exothermic and endothermic respectively. Metal-organic frameworks (MOFs) have been actively considered for such applications because they can hold many molecules inside of their porous structures, but their thermal conductivities, which are important to induce enhanced heat transfer for rapid adsorption / desorption, have been experimentally measured only a few times. Moreover, there is an ongoing debate on how the thermal conductivity of MOFs would change through adsorption / desorption. In Chapter 4, accurate experimental measurements of thermal conductivity of HKUST-1 MOF single crystals before and adsorption of different liquid molecules of ethanol, methanol and distilled water are presented. The pristine HKUST thermal conductivity after thermal activation is measured as 0.68 ± 0.25 W/m·K which matches well with the simulation predicted value. This decreased to approximately 0.29 ± 0.13 W/m·K, 0.15 ± 0.04 W/m·K and 0.2 ± 0.09 W/m·K after full methanol, ethanol and water liquid adsorption, respectively, which suggests that the heat-carrying phonons indeed are scattered more because of pore-occupying liquid molecules. The largest drop in thermal conductivity can be attributed to the lowest thermal conductivity of intrinsic ethanol liquid. Also, the largest kinetic diameter of the liquid ethanol molecule can scatter heat-carrying phonons more effectively than other liquid molecules.

Contents

List of figures

2.S3 Both fitted and experimental dispersion relationships of (a) Au (b) Cu (c) Cr shown on the far-left with the Al_2O_3's dispersion relationship in the middle for comparisons. Solid line and rectangular markers represent the longitudinal branch, and dashed line and circular markers represent the transverse branch. The transmission coefficients of each metal for longitudinal and transverse polarization branches are presented on the far right hand side with respect to frequency, ω. *(Refs.* [37–40] *provided in the main text).* Used and reprinted with permission from American Physical Society [36].

3.1 (a) A schematic of the assembled SiO_2-SiO_2 gap structure where the top membrane with a thickness *t* is attached to the bottom structure with the supporting pillars that are separated by a width of *L* (b) The maximum deflection of the top SiO_2 layer (Δt) as a function of different *t* values for different sizes of *L* when the whole assembly is subjected under 1 atm pressure. A pressure of 1 atm is chosen because the gap will be subjected to a cycle of evacuation and venting to the ambient pressure. The dashed line shows the chosen Δt_{max} critical value of 1 Å, which is chosen for being a fraction of the smallest gap size of 1 nm.

3.2 The calculated phase lag difference when the thermal conductance across the gap changes from 24 KW/m^{2}K to 120 KW/m^{2}K as a function of heating frequency for different *t* values. The 10 μm, 100 μm and 1,000 μm curves are identical to one another.

analysis results on the 10 nm SiO_2-SiO_2 gap sample. Some of the outliers are excluded in fitting.

3.13 Overall analysis results for different gap samples. Both non-differential and differential analysis results are shown in squares and circles, respectively. The open symbols represent the air case and the filled symbols represent the vacuum case. The expect values for the air and vacuum cases are shown for each case.

3.S1 A cantilever beam fixed at both ends with uniform pressure load applied over top surface. Adapted and used with permission from T. Ganapathy.

3.S2 A schematic of a sample assumed in annular fin analysis with effective properties used to describe radial spreading of heat. Here, R represents the material radius; r_0, the laser spot size; and t, the material thickness. The material's outer surface is assumed to be adiabatic with the air assumed at the bottom. Adapted and used with permission from T. Ganapathy.

3.S3 Normalized temperature rise on the 80 nm Au layer due to modulated laser heating, θ, as a function of radial position away from the laser spot, r, for different frequencies, f (0.1 MHz, 1 MHz, 10 MHz) when the air gap has a total heat transfer coefficient of 1.0×10^5 W/m^{2}K.

4.S2 (a) Analytically calculated phase lags as a function of heating frequency for different κ_{trans}. when the MOF thermal conductivity changed from 0.7 W/m·K (solid lines) to 0.1 W/m·K (dashed lines). (b) The difference in phase lags represented with the solid and dashed lines as a function of heating frequency.

4.S3 A histogram of thermal conductivity measurements of HKUST-1 crystals after thermal activation. This data set represents a total of 8 crystals and 21 measurement spots.

List of tables

Introduction

1.1 Motivation

As technologies advance further, many of our devices and structures are getting smaller in size yet stronger in performance. However, as the device gets more compact, heat that is inevitably generated during operation impacts its temperature more profoundly. Thus, optimizing the performance of these small devices requires effective thermal management, even at the level of interfaces, due to the increased surface-to-volume ratio that accompanies reduced dimensions and the use of layered structures for various electronic and optical functions [1–4]. Considering the needs for being 'smaller yet stronger' will continue to increase in the future in almost all technological applications, the issue of efficient thermal management in nano or micro-sized devices requires more attention and understanding.

In addition to electronic applications, many environmental applications can improve their overall efficiencies by controlling the rate of heat transfer. One of them is applications of adsorption for various capture processes, including carbon dioxide (CO_2) capture [1]. Because adsorption processes are exothermic, faster heat removal is critical to control temperature and thus capturing efficiency. Moreover, regeneration of the adsorbents through desorption, which is an endothermic process, also requires enhanced heat transfer to maintain the adsorbent temperature high enough as not to suppress desorption kinetics. Therefore, it is important to accurately measure the thermal properties of an adsorbent and to analyze how it will change under different adsorption conditions to select ideal sets of materials for capture applications.

In this dissertation I present measurements and analyses of the thermal transport properties of metal-dielectric interfaces focused specifically on future heat-assisted magnetic

recording (HAMR) applications and metal-organic framework (MOF) adsorbents via a non-contact optical method called frequency domain thermoreflectance. The main objective is to better understand thermal transport phenomena in various material systems under different conditions to inform potential improvements of thermal management in actual engineering applications.

1.2 Background & Objectives

1.2.1 Thermal management in heat-assisted magnetic recording (HAMR) applications

Hard drive manufacturing companies such as Seagate Technologies and Western Digital have been attempting hard to accommodate the recent rapid increasing need to store digital information that is generated and shared worldwide by increasing their data storage capacity. To achieve a higher storage capacity, the aerial density of hard drives should increase by reducing the size of grains in a bit cell [5]. However, when the grain size becomes very small, thermal fluctuations cause the magnetization of grains to become unstable [6]. This phenomenon is called superparamagnetism. It is reported that in cobalt (Co)-based ferrite magnetic media ($CoFe_2O_4$), the limit for the grain size to avoid superparamagnetism is approximately 6 nm at 300 K [7].

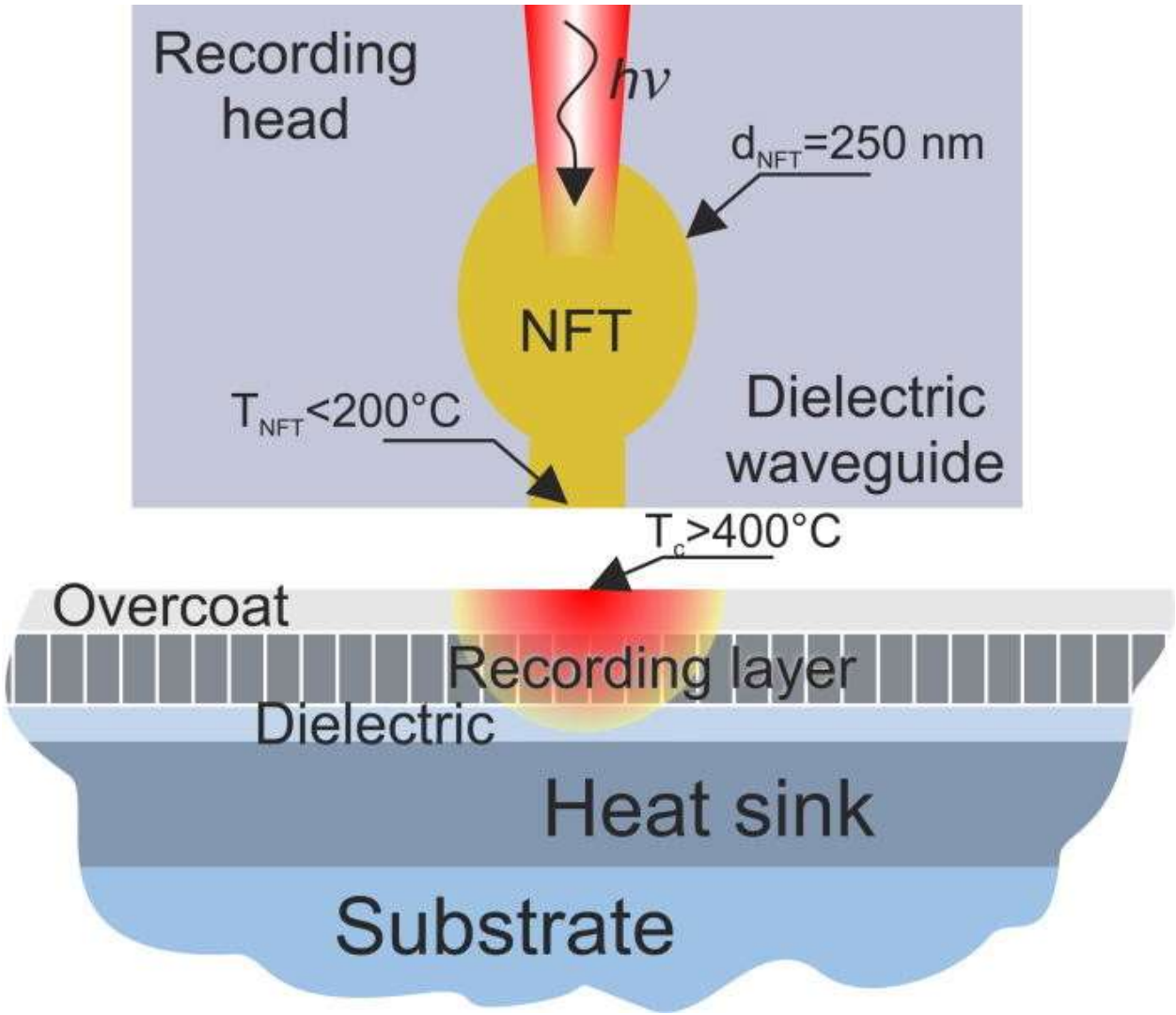

Fig. 1.1. A descriptive schematic of near-field transducer (NFT) and overall recording structure in HAMR system. This reproduced figure, *"HAMR head and media including key spacing and thickness parameters"* by Dieter Weller, is licensed under CC BY 4.0 and can be found in Ref. [8].

To overcome this unstable fluctuation magnetic media with high magnetic anisotropy should be used [9]. Unfortunately, magnetizing such media requires an intense magnetic

switching field [10]. Heat-assisted Magnetic Recording (HAMR) could provide a solution for this issue by locally heating the magnetic media to near its Curie temperature thereby reducing the required magnetic switching field strength [11,12].

In HAMR, a localized heating is enabled by a near-field transducer (NFT) as shown in Fig 1.1. First, guided by optics such as a planar solid immersion mirror (PSIM), the short-wavelength infrared light will be focused and coupled to the Au-NFT. Coupling between the light and the electrons in the Au creates surface plasmon polaritons (SPPs), which travel to the tip of the NFT structure along the Au-dielectric interface as electromagnetic radiation. These SPPs are evanescently confined near the interface and can thus be focused onto a very small spot with high field intensity by controlling the interface dimensions. The intense electric field created at the tip by the SPPs will then create oscillations in the electrons in the media thereby heating it up [13–15].

While the SPPs travel down the Au-dielectric interface a parasitic loss occurs in the Au itself and the heat generated must be dissipated into the surrounding dielectric, which results in peak NFT temperatures that are hundreds of degrees above the ambient temperature [13]. This could potentially lead to thermal breakdown of a HAMR device and thus should be addressed through efficient thermal management. One possible way to solve this problem is to increase the thermal conductivity, κ, of NFT material. Fourier's law of heat conduction defines q'', the heat flux as follows:

$$q'' = -\kappa \nabla T \,, \tag{1.1}$$

where κ is the thermal conductivity of material and ∇T is the temperature gradient. Equation (1.1) clearly indicates that increasing κ will reduce thermal gradients for a given heat flux.

Moreover, because κ changes as a function of temperature, careful selections of ideal materials for a range of temperatures in which they will be used are critical.

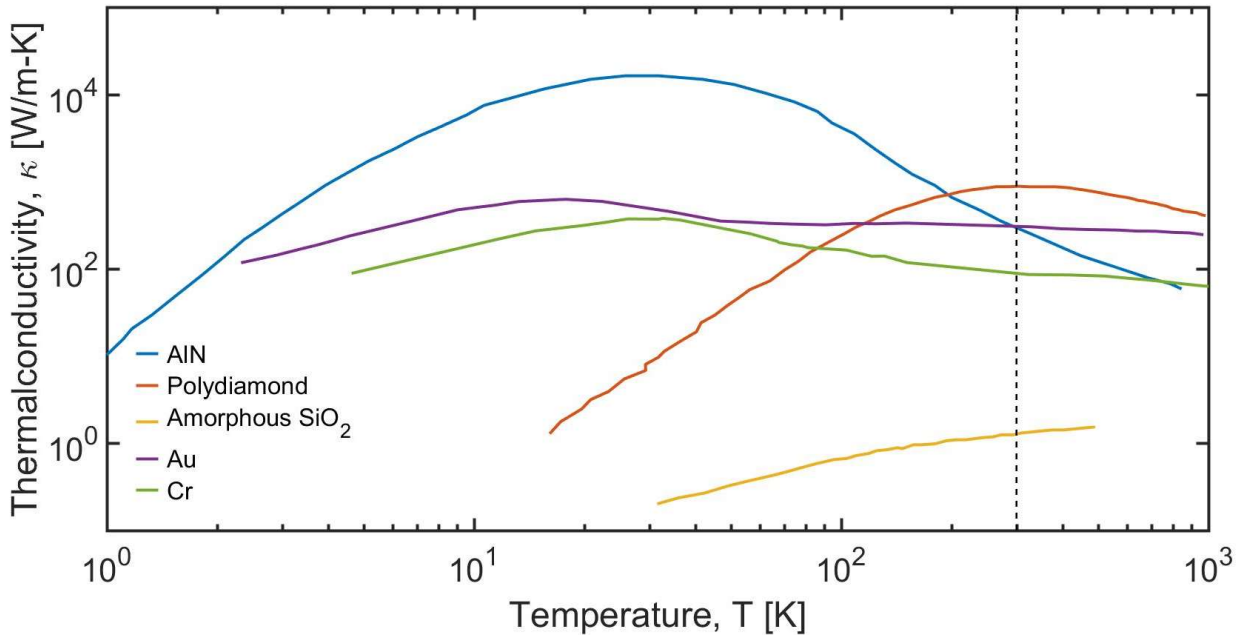

Fig.1.2. κ of various materials that are used in HAMR NFT system as a function of temperature. The chosen materials were aluminum nitride (AlN), Polydiamond, silicon dioxide (SiO_2), gold (Au) and chromium (Cr). The dashed line represents a temperature of 300 K [16–19]. Reprinted and adapted with permission from Cambridge University Press [20].

Fig.1.2 shows κ of several HAMR related materials as a function of temperature. For applications like HAMR where the metal NFT is surrounded by the dielectric heat sink material and recording media has a layered structure, an interface between materials also plays an important role in heat transfer. While there have been many attempts to enhance thermal conductance at the metal-dielectric interface especially with the use of adhesion layers,

systematic studies on the optimal thickness of adhesion layer have not been conducted. Chapter 2 of this dissertation presents both theoretical predictions and experimental measurements of enhancement in thermal interface conductance at the gold (Au) metal- sapphire (Al_2O_3) dielectric interface as a function of thickness of copper (Cu) and chromium (Cr) adhesion layers.

1.2.2 Thermal physics background

1.2.2.1 Thermal transport due to gas molecules

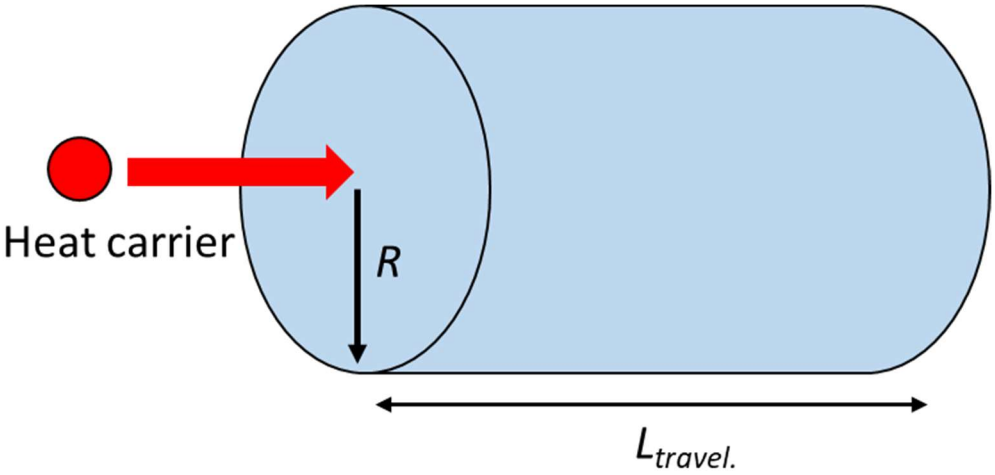

Fig.1.3. An illustrative description of a particle travelling inside a collision volume where the collision events occur. Here, R and $L_{travel.}$ define the radius and length of the collision volume, respectively.

Based on kinetic theory, a following equation can be derived for κ of an ideal gas as:

$$\kappa = \frac{1}{3} C \bar{v} l \ , \tag{1.2}$$

where C is the heat capacity of the gas ($=\frac{3}{2}k_b\eta$ for monatomic molecules, where k_b is Boltzmann's constant and η is number density of molecules), $\bar{v}$ is the average speed of gas molecules and l is the mean free path of molecules. l is the average distance a particle travels between scattering events and can be determined by dividing the length of travelling path by the number of collision events. If we assume the following geometry shown in Fig.1.3 where a particle travels a total length of L_{travel} inside a circular tube with a radius of R, the total volume swept by the particle for a given period of time (τ) before collision will be $\pi R^2 \cdot \bar{v} \cdot \tau$. Then, the total number of collision events that occurs in the collision volume will be defined as the number of particles per unit volume (η) by the collision volume. If the particles are ideal gas molecules, then η can be obtained from the ideal gas law. Because, L_{travel} is the same as $\bar{v} \cdot \tau$, l can be expressed as:

$$l = \frac{\bar{v}\cdot\tau}{\pi R^2 \bar{v}\cdot\tau\cdot\eta} = \frac{1}{\pi R^2\cdot\eta}. \quad (1.3)$$

Accordingly, Equation (1.2) can be re-written for the monoatomic gas molecules as:

$$\kappa = \frac{1}{3}\cdot\left(\frac{3}{2}k_b\eta\right)\cdot\bar{v}\cdot\left(\frac{1}{\pi R^2\cdot\eta}\right) = \frac{1}{2}k_b\cdot\bar{v}\cdot\left(\frac{1}{\pi R^2}\right) \quad . \quad (1.4)$$

According to Equation (1.4), there is no pressure dependence of κ; this regime where κ is independent of pressure is called the diffusive regime. This equation, however, is only valid when intermolecular collisions are dominant. In the other extreme, if l is much larger than the characteristic length scale of the system (L_{char}), then l=L_{char}. In this case, without any intermolecular scattering event, Equation (1.4) should be rewritten as

$$\kappa = \frac{1}{3}\cdot\left(\frac{3}{2}k_b\eta\right)\cdot\bar{v}\cdot L_{char} = \frac{1}{2}k_b\cdot\bar{v}\cdot\left(\frac{P}{k_bT}\right)\cdot L_{char}\left(\because \eta = \frac{P}{k_b\cdot T} \text{ from ideal gas law}\right). \quad (1.5)$$

Here, the pressure dependence exists for κ. This regime where the scattering of heat carrying particles is primarily boundary scattering, not the inter-particle scattering, is called the ballistic regime. Fig.1.3-(a) shows a descriptive illustration of these two different regimes in heat conduction. In the intermediate regime, the Matthiessen rule describes the effective l as $l^{-1} = l_i^{-1} + L_{char}^{-1}$, where the subscript i is for an individual molecule. Fig.1.4 shows how the thermal conductivity of nitrogen (N_2) gas changes as a function of pressure using Equation (1.5) and other parameters given in Refs. [21,22].

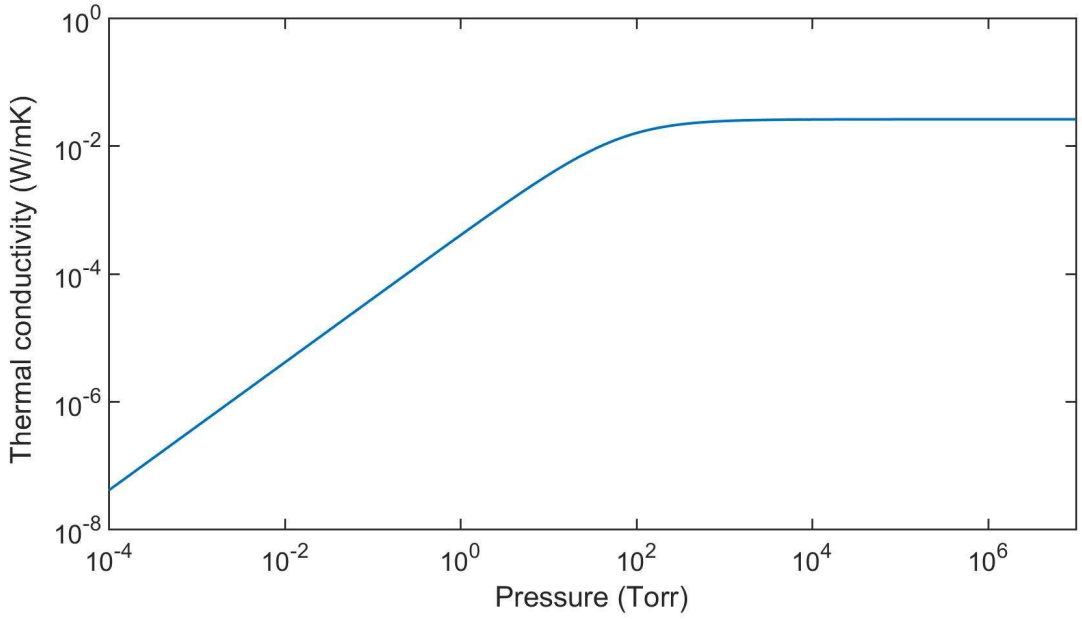

Fig.1.4. κ of N_2 gas molecules as a function of pressure. The parameters used for calculations are provided in Refs. [21,22].

1.2.2.2 Thermal transport due to phonons

Phonons, commonly defined as the quanta of lattice vibrations, can be treated with particle-based models unless feature sizes are on the order of phonon wavelengths. Treating

phonons as a gas of particles, classical description of phonon thermal conductivity can be written similarly as Equation (1.2). Applying the kinetic theory of gases and the Debye model, in which the linear slope is assumed in the phonon dispersion relationship for all the phonon frequencies, ω ($\omega = v_s k$), the thermal conductivity contribution due to phonons can be described as:

$$\kappa = \int \kappa(\omega) d\omega = \frac{1}{3} \int C(\omega) v_s l(\omega) d\omega \,, \tag{1.6}$$

where $C(\omega)$ is the specific heat, v_s is the sound velocity and $l(\omega)$ is the phonon mean free path. The l is defined as the distance a phonon travels between collisions with other phonons, material impurities, or boundaries. Callaway and von Baeyer re-wrote Equation (1.6) as:

$$\kappa = \frac{k_b}{2\pi^2 v_s} \left(\frac{k_b T}{\hbar}\right)^3 \int_0^{\theta/T} \tau_c(x) \frac{x^4 e^x}{(e^x - 1)^2} dx \,, \tag{1.7}$$

where $x = \hbar\omega / k_b T$ and θ is the Debye temperature [23]. The term τ_c in equation (2) is the average phonon relaxation time which describes the average period of time of phonon collisions or scatterings. This term depends on different phonon scattering mechanisms and can be estimated as $\tau_c^{-1} = \tau_P^{-1} + \tau_D^{-1} + \tau_B^{-1}$, where each subscript, *P, D* and *B* represents the phonon-phonon, material defects and boundary scattering mechanism for phonons. Typically, as T approaches θ, phonon-phonon scattering becomes the most dominant [4,24,25].

1.2.2.3 Thermal transport due to electrons

Electrons in metal also carry heat and they have much faster group velocity than phonons (10^6 m/s versus 10^4 m/s), making them the dominant energy carrier [20,26]. Similar to Equation (1.2), the electron thermal conductivity can be written as follows:

$$\kappa_e = \int \frac{1}{3} C_e(E) v_e(E) l_e(E) dE \,, \tag{1.5}$$

where v_e is the electron velocity and l_e is the electron mean free path. Because electrons that can participate in heat transport exist over very narrow ranges (~k_bT) near the Fermi energy [20,27], $v_e(E)$ in Equation (1.5) can be treated as v_F, the Fermi velocity. Usually κ_e can be approximated using the Wiedemann-Franz Law which relates κ_e to σ, electrical conductivity, as $\kappa_e = \sigma L_0 T$ where L_0 is the Lorentz number (2.44×10^{-8}WΩK^{-2}) and T is the temperature [20,28].

1.3 Thermal interface conductance at metal-dielectric interface

Equation (1.1) relates q'' to ∇T for a given material. At an interface between materials, the temperature jump ΔT is related to q'' as

$$q'' = G\Delta T \ , \tag{1.6}$$

where G is the thermal interface conductance. Using both κ and G, the Kapitza length (l_k), which represents a material thickness that generates equivalent thermal resistance as an interface, can be calculated as follows [20,29,30]:

$$l_k = \frac{k}{G} \ . \tag{1.7}$$

Thus, when a material dimension approaches l_k, thermal resistance at the interface becomes commensurate to the intrinsic thermal resistance of the layers and G becomes a critical value in controlling the temperature. One application where the interface plays a critical role is HAMR. As introduced in Section 1.2.1, the NFT in HAMR generates surface plasmon polaritons (SPPs) at the Au-dielectric interface [31,32]. While the SPPs travel down the Au-dielectric interface a parasitic loss occurs in the Au itself and the resultant heat must be dissipated to the

dielectric, which results in peak NFT temperatures that are hundreds of degrees above the ambient temperature [31]. In this situation, the interface between the Au and the dielectric becomes the bottleneck for heat dissipation. For metal-dielectric interfaces, it is typically assumed that electrons first transfer their energy to phonons in the metal with an equivalent conductance of $G_{e\text{-}p}$, and the phonons in the metal then transmit through the interface into the dielectric with G_p. Because these processes represent thermal resistances in series, G becomes $(G_{e\text{-}p} \cdot G_p) / (G_{e\text{-}p} + G_p)$ [33–41]. The ratio of $G_{e\text{-}p}/G_p$ in the Au-Al_2O_3 interface is nearly 5 [33,41,42]. Because $G_{e\text{-}p}$ is larger, as shown by Wang et al. [43], the G_p term becomes a bottleneck in the overall G. Notably, Wang et al. showed that temperature-dependent measurements of the electron-phonon coupling constant in thin films agree with Kagnov's classical theory for bulk materials [41,43,44]. Thus, it is important to increase the phonon thermal conductance across an interface in the HAMR NFT system.

1.4 Near-field vs. Far-field thermal radiation

Heat transfer can occur in three methods; conduction, convection and radiation. In HAMR, a sharp tip of the NFT and narrow gap between the NFT and the recording media (< 10nm) enables coupling of SPPs and strong local heating of the media. This narrow gap also enables heat to radiate back from the media into the NFT. This "back-heating" of the NFT head from the heated media can eventually lead to thermal breakdown. Because the distance where the heat would travel from the media back to the NFT can be as short as 5 nm [20] in HAMR applications, heat transfer exceeding the limit predicted by the black body thermal radiation can occur due to the near-field thermal radiation. Therefore, understanding the extent of near-field thermal radiative transport through a nano-sized gap is important.

Radiative heat transfer occurs when thermal energy is transferred via electromagnetic waves where the spectrum of the emitted electromagnetic waves depends on the temperature of the emitting surfaces. Planck's theory describes the spectral density of thermal radiation of a black body and states that maximum thermal radiation is not possible if the object does not behave like a black body [45,46]. This theory holds true when the radiating bodies or the distance between them is larger than the thermal de Broglie length (λ_b) defined for a specific temperature as $\hbar / \sqrt{(\pi m k_b T)}$ where $\hbar$ is the reduced Planck's constant [45]. This 'larger' dimension case is called the far field thermal radiation limit. On the other hand, when bodies are separated less than λ_b, the radiative heat transfer limit imposed by the Planck's law can be overcome due to the existence of evanescent radiative modes. This phenomenon is referred to as near-field radiative heat transfer and has been experimentally observed with separation distances as small as 2 nm [45,47–49].

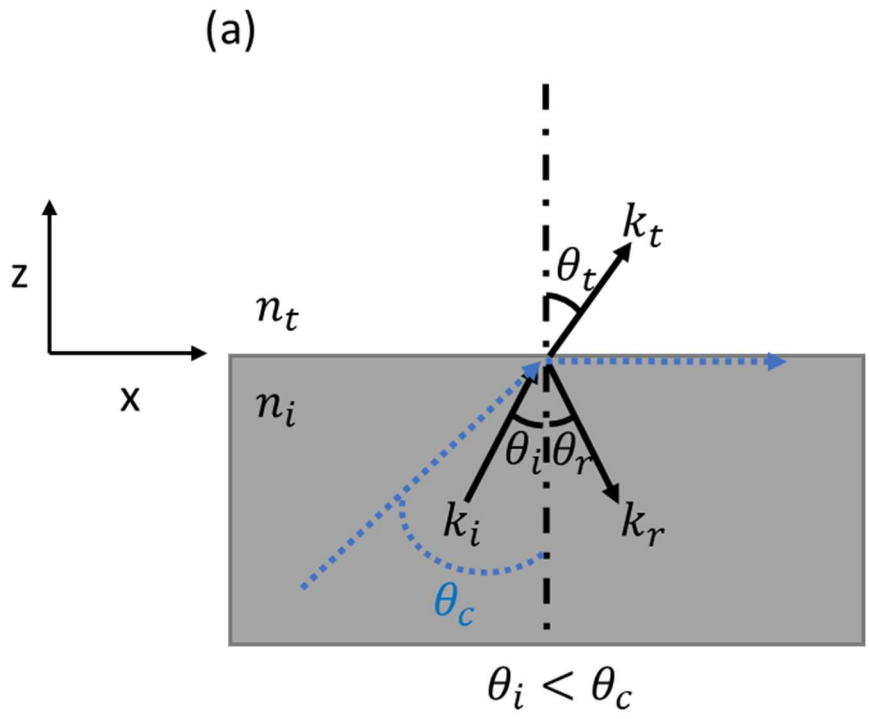
(a)
z
x
n_t
n_i
k_t
θ_t
θ_i
θ_r
k_i
k_r
θ_c
$\theta_i < \theta_c$

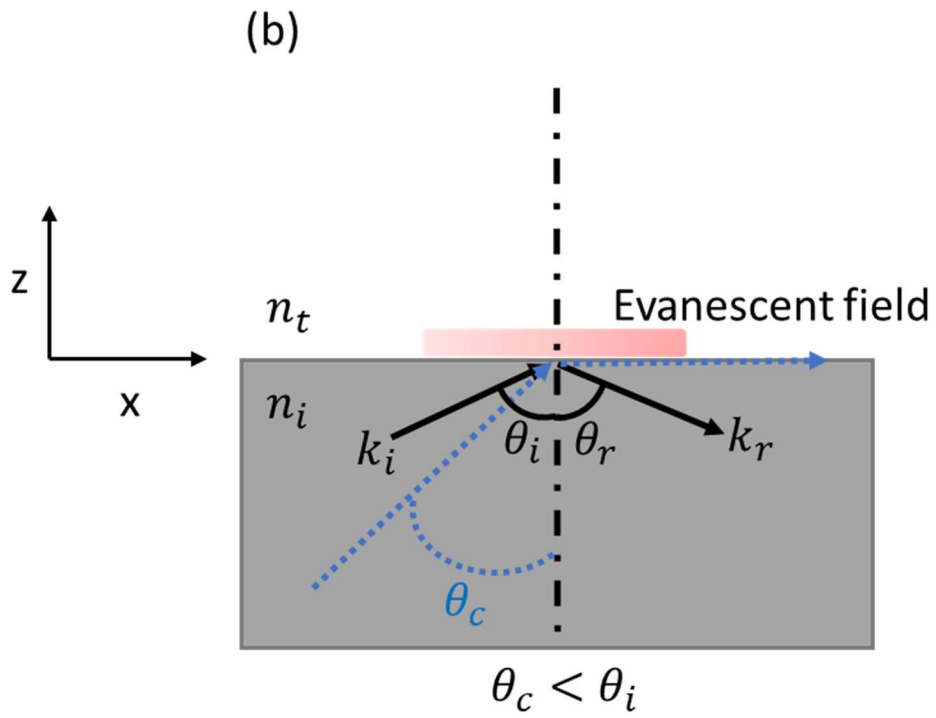
(b)
z
x
n_t
Evanescent field
n_i
k_i
θ_i
θ_r
k_r
θ_c
$\theta_c < \theta_i$

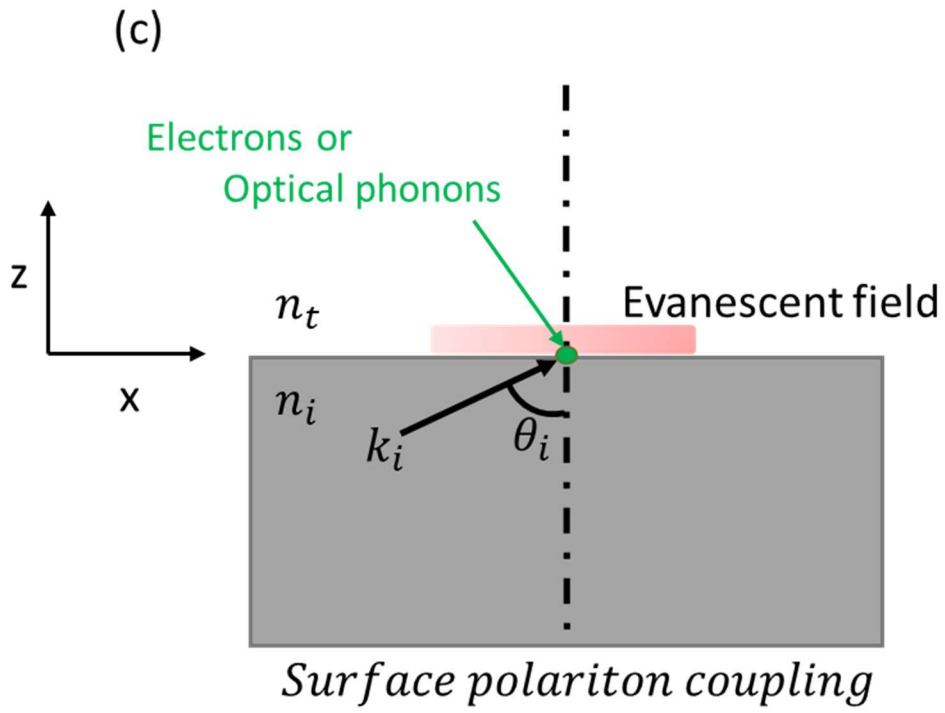

Fig.1.5. Descriptive illustrations of travelling electromagnetic waves when (a) the incident angle, θ_i is smaller than the critical angle θ_c (b) θ_i is larger than θ_c and (c) Coupling of photons in electromagnetic waves with electrons or optical photons occurs. Here, k_i is the incident wave's wavevector with an incident angle of θ_i, and subscript *r* and *t* indicate those for the reflected and transmitted waves, respectively. Adapted from Ref. [50] with permission from The Royal Society of Chemistry.

Electromagnetic waves generated by thermal radiation can travel in propagating and evanescent modes. As shown in Fig.1.5-(a), if we assume an electromagnetic wave with a refractive index of n_i and a wavevector of k_i is incident onto an interface with a surrounding medium with a refractive index of n_t at an incident angle (θ_i), reflection and transmission could

happen. The transmitting portion constitutes the propagating modes. If we write an expression for the parallel component of the transmitted wave's wavevector (k_t), $k_{t,x}$, it becomes as follows

$$k_{t,x} = k_t \sin(\theta_t) = k_t \frac{n_i}{n_t} \sin(\theta_i) \ \ (\because n_i \sin\theta_i = n_t \sin\theta_t \text{ from Snell's law}) , \qquad (1.8)$$

where θ_t is the angle of transmittance. A similar equation for the vertical component can be written as follows

$$k_{t,z} = k_t \cos\theta_t = \pm k_t \sqrt{(1 - \sin^2\theta_t)} \quad (\because \sin^2\theta_t + \cos^2\theta_t = 1)$$

$$= \pm k_t \left(1 - \frac{n_i^2 \sin^2\theta_t}{n_t^2}\right)^{1/2} (\because n_i \sin\theta_i = n_t \sin\theta_t \text{ from Snell's law}). \qquad (1.9)$$

According to this equation, when the radicand becomes negative, $k_{t,z}$ will have both real and imaginary parts. This occurs when total internal reflection occurs; this occurs when θ_i is larger than θ_c, the critical angle, and n_i is larger than n_t as shown in Fig.1.5-(b). θ_c from Snell's law is defined as $\sin^{-1}(n_t/n_i)$. Because $\theta_i > \theta_c$ in total internal reflection, $\sin\theta_i > \sin\theta_c$, which makes the radicand in Equation (1.9) negative. Thus, we can re-write Equation (1.9) for the total internal reflection case as

$$k_{t,z} = \pm k_t \left(1 - \frac{n_i^2 \sin^2\theta_t}{n_t^2}\right)^{1/2} = \pm k_t \cdot \mathrm{i} \cdot \left(\frac{n_i^2 \sin^2\theta_t}{n_t^2} - 1\right)^{1/2} \quad (\because \mathrm{i} = \sqrt{-1})$$

$$= \pm \mathrm{i} \cdot \left[\frac{k_t}{n_t}\left(n_i^2 \sin^2\theta_t - n_t^2\right)^{\frac{1}{2}}\right]$$

$$= \pm \mathrm{i} \cdot \alpha \quad . \qquad (1.10)$$

The plane wave form of the electric field generated due to the transmitted electromagnetic wave can be written as $E_t = E_{0,t} e^{\mathrm{i}(k_t \cdot r - \omega \dot{t})}$ where $E_{0,t}$ is the maximum electric field amplitude in the transmitted wave, r is the position of the wave in $x - z$ plane, ω is frequency and $\dot{t}$ is time. Because there are only x and z directions defined here, $k_t \cdot r$ is expressed only in x and z terms using Equation (1.10) as

$$E_t = E_{0,t} e^{\mathrm{i}(k_t \cdot r - \omega t)} = E_{0,t} e^{\mathrm{i}(k_{t,x} x + k_{t,z} z - \omega t)} \quad (\because k_t \cdot r = k_{t,x} x + k_{t,z} z).$$

$$= E_{0,t} \mathrm{e}^{\mathrm{i}\left(\left(k_t \frac{n_i}{n_t} \sin(\theta_i)\right) \cdot x + (\pm \mathrm{i} \cdot \alpha \cdot z) - \omega t\right)}$$

$$= E_{0,t} e^{\pm \alpha \cdot z} \mathrm{e}^{\mathrm{i}\left(\left(k_t \frac{n_i}{n_t} \sin(\theta_i)\right) \cdot x - \omega t\right)} \tag{1.11}$$

Because an exponentially propagating field to infinity is not possible, the sign of α should be negative. Thus, the wave amplitude will be $E_{0,t} e^{-\alpha \cdot z}$, which shows that there will be a field that will extend vertically in the positive z direction with exponentially decaying amplitude. The depth that the original field intensity (E_t^2) will decay to its $1/e$ value is called penetration depth, d, which can be defined based on Equation (1.10), (1.11) and the definition of wavevector ($k = 2\pi\lambda$) as:

$$d = \frac{\lambda_0}{4\pi} (n_i^2 \sin^2 \theta_i - n_t^2)^{-1/2} , \tag{1.12}$$

where λ_0 is the wavelength of light in vacuum [51]. This shows that if the bodies that are exchanging thermal radiative energy are separated by a distance equal to or less than d, the thermal radiative heat transfer will be enhanced because of the participation of the evanescent modes, in addition to propagating modes such that it can exceed the blackbody radiation limit.

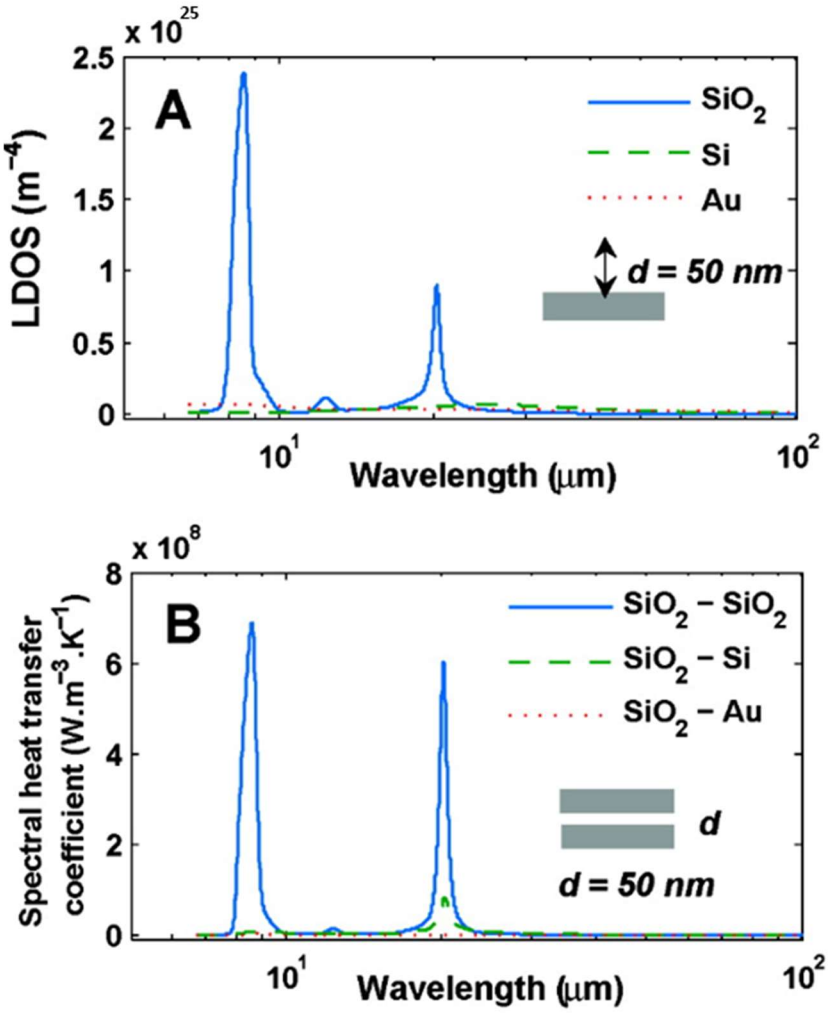

Fig.1.6. (a) Photon LDOS calculated in vacuum at 50 nm above a vacuum-material interface for SiO_2, Si and Au as a function of wavelength. (b) Calculated spectral heat transfer coefficient across a 50 nm vacuum gap located between SiO_2 and SiO_2, SiO_2 and Si, and SiO_2 and Au layers. Reprinted and adapted with permission from Nano Letters 9 (8), pp 2909-2913: *"Surface Phonon Polaritons Mediated Energy Transfer between Nanoscale Gaps"* by Shen et al. Copyright 2009. American Chemical Society [48].

Secondly, evanescent modes can be generated by surface polaritons resulting from interactions of electromagnetic waves (photons) with collective oscillations of free electrons (surface plasmon polaritons, SPPs) or transverse optical phonons (surface phonon polaritons, SPhPs) within the thermal emitter (Fig.1.5-(c)) [45,52,53]. It is well established that surface polaritons generate decaying fields that extend vertically in both $-z\ and\ +z$ directions into media 1 and media 2 respectively with certain penetration depths defined for SPPs (d_{SPP}) and SPhPs (d_{SPhP}) [45,53,54]. Same as the total internal reflection case, if the bodies that are exchanging radiative energy are within the distances of d_{SPP} or d_{SPhP}, the black body-based thermal radiation limit will be exceeded due to strong participation of evanescent modes. Generally, the near-field effect due to SPhP or SPPs is maximized if we have two materials that are similar or identical in terms of dielectric functions [48]. Fig.1.6-(a) presents calculated photon local density of states (LDOS) plotted for different materials (SiO_2, Silicon (Si) and Au) as a function of wavelength, where LDOS were calculated in vacuum at 50 nm above a vacuum-material interface [48,55]. One can see that only SiO_2 exhibits strong peaks; this is because only the polar SiO_2 can have optical phonon modes that can couple with photons. When the spectral heat transfer coefficient (Fig.1.6-(b)) across a vacuum gap sandwiched differently between SiO_2 and SiO_2, SiO_2 and Si or SiO_2 and Au is calculated per wavelength, the highest spectral heat transfer coefficient is observed in the SiO_2-SiO_2 coupled case. This occurs because over the narrow wavelength range of SiO_2's SPhPs, Si and Au's LDOS are small, which negates the strong SPhP resonance on the SiO_2 side [48].

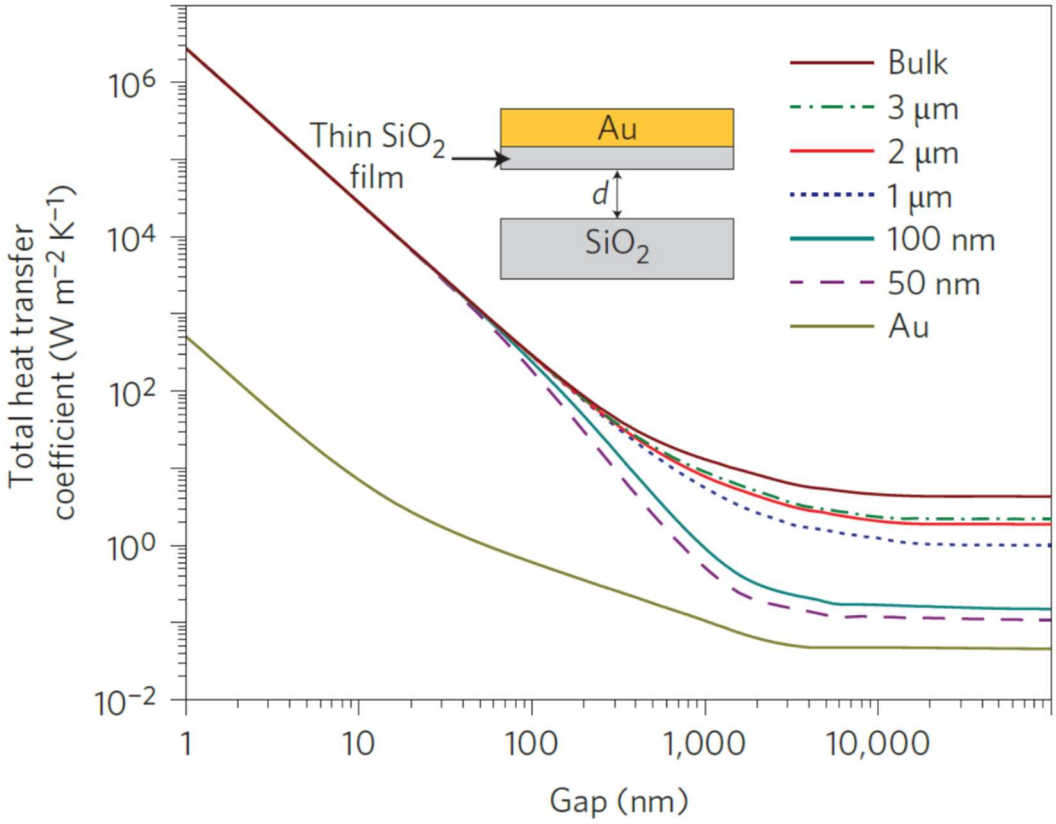

Fig.1.7. The calculated radiative heat transfer coefficients as a function of gap size located between Au and SiO_2 layers or SiO_2 and SiO_2 layers. Used by permission from Springer Nature: Nature Nanotechnology, *"Enhancement of near-field radiative heat transfer using polar dielectric thin films"* by Bai Song et al., 2015 and can be found in Ref. [51].

Another study calculated radiative heat transfer coefficient as a function of gap size located between Au and SiO_2 layers or SiO_2 and SiO_2 layers (Fig.1.7). As already explained, the gap between SiO_2 and SiO_2 layers showed much higher radiative heat transfer coefficients, at least ~10 times higher, than the one between Au and SiO_2 regardless of the gap sizes. In addition, the thickness of the thermal sources should be equal to or larger than the gap spacing to ensure

that all portions of evanescent modes generated across the interface can participate in heat transfer [45,56].

In this dissertation, in an attempt to probe the near-field radiative effect, we measure how large the heat transfer coefficient is across the nanostructured gap that mimics the actual HAMR NFT geometry via optical frequency-domain thermoreflectance (FDTR) technique. Because there have been no experimental measurements of measuring a near-field radiative behavior as a function of temperature, the FDTR's capability to use a cryostat device is beneficial. As shown in Fig.1.7, the near-field radiative effect is not going to be clearly observable unless the gap dimension is less than 50 nm. Therefore, creating a narrowly spaced gap structure is critical. In addition, accurately measuring thermal transport properties across such thin structures and validating them are also important. Thus, while our ultimate goal is accurately measuring the temperature-dependent near-field radiative behavior, we focused heavily on designs and fabrications of nanoscale gap structures as well as developing an analytical method to accurately report the gap thermal properties in this study. Detailed descriptions of sample designs and fabrications along with the preliminary measurements are presented in Chapter 3.

1.5 Importance of thermal conductivity in adsorption and desorption

Adsorption is a process where molecules in multi-component fluids such as gases or liquids are attached to the solid adsorbent (the solid that adsorbs the incoming gas or liquid) surface via weak physical or strong chemical attachment [1,57]. Desorption is the opposite process where the attached molecules are released to the ambient environment. Ideal solid adsorbents or desorbents will have large surface area and high porosity to capture incoming molecules and to release them more efficiently.

During adsorption, when an atom or a molecule is located on the surface, the atom has higher free energy than the one inside the bulk material. Therefore, the unbonded atoms on the surface want to lower their free energy by forming bonds, making them readily accept a part of atoms or molecules in gas or liquid that enter the solid. This surface attraction governs overall gas-solid or liquid-solid adsorption processes [57]. Thermodynamically, entropy of freely moving atoms or molecules in gas or liquid also decreases when they are adsorbed to solid surface along with the free energy. Based on the fundamental Gibbs free energy equation, $\Delta H = \Delta \dot{G} + T\Delta S$, the decrease in both free energy, $\dot{G}$, and entropy S will entail decrease in enthalpy, H, meaning that the adsorption process is exothermic even though there are a very few reported endothermic processes. Consequently, the desorption process will be endothermic [57]. Therefore, efficient heat exchange in the solid adsorbent is conducive to better control overall rate of adsorption and desorption processes for actual molecule capturing or releasing applications. For this, developing higher thermal conductivity solid adsorbents or desorbents based on accurate thermal property analysis is very important. Of all the currently studied materials, metal-organic frameworks (MOFs) have been actively considered for their ultra-high porosity, large surface area, controllable properties, and uniform structure [58,59].

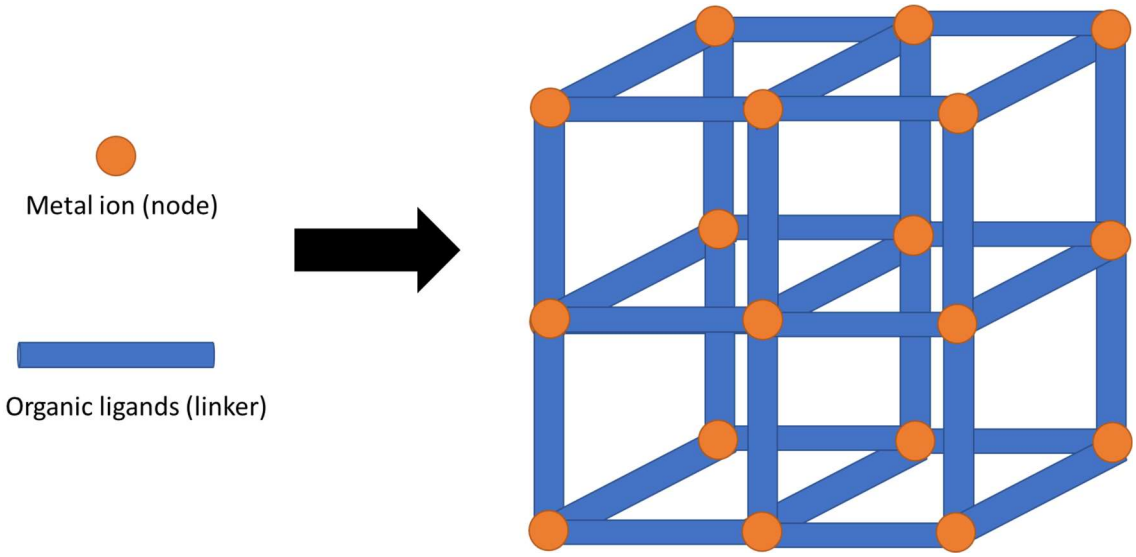

Fig.1.8. A descriptive illustration of metal-organic framework (MOF) structure

As shown in Fig.1.8, MOFs are organic-inorganic hybrid materials that are composed of metal ions and organic ligands linked together by coordination bonds [60,61]. There have been numerous reports on possibilities of using MOFs for chemical separations, hydrogen storage, drug delivery, water treatment and sensing [59,62–66]. Despite promising opportunities with MOFs, there have been a limited number of experimental measurements on their thermal conductivities. Huang et al., presented that MOF-5 in a single crystal form has a thermal conductivity of 0.32 W/mK at 300K and showed temperature-dependent measurement data in 2007 [67]. In 2012, Liu et al. reported the thermal conductivity measurement results of a composite composed of MOF-5 and expanded natural graphite (ENG) at 300K, followed by Gunatilleke et al.'s work on the MOF-1 thermal conductivity measured as a function of temperature from 12K to 300K in 2017 [68]. Other interesting studies based on MOF-5 nanofluids and thin-film MOFs have also been reported but the variety of studied MOFs is narrow and the number of reports is still limiting [69,70].

This lack of accurate and a sufficient amount of experimental work on MOF thermal conductivity leads to a scientific debate in the MOF simulation community whether the thermal conductivity of MOFs should increase or decrease after adsorption; while one group simulated that the thermal conductivity will decrease due to increased phonon scattering with adsorbates sitting inside a porous structure, other group expect that it will increase because the adsorbates will provide a better heat conduction channel than empty voids in MOFs. Thus, it was our objective to settle this ongoing debate by accurately measuring thermal conductivity of MOF samples before and after adsorption. Chapter 4 presents the results of thermal conductivity measurements of HKUST-1 MOF samples in a single crystal form before and after various organic liquid adsorption and gives a possible explanation why the result turns out to be a decrease in thermal conductivity after adsorption.

1.6 Measurements of thermal properties using frequency-domain thermoreflectance (FDTR)

In our laboratory, nanoscale thermal transport is measured by frequency domain thermoreflectance (FDTR) technique. In this technique, a 488nm continuous wave (CW) pump laser is intensity modulated by an electrooptic modulator over a range of frequencies. Upon absorbing the modulated pump beam the sample surface is heated periodically at the same modulation frequency as the pump beam. Because of this periodic heating, the temperature at the surface changes which causes periodic changes in surface optical reflectance (i.e. thermoreflectance). This optical response is detected by a 532nm CW probe laser beam that is co-aligned with the pump at the sample surface since the thermoreflectance of Au is peaked at 532 nm, the probe beam will be modulated in intensity. The temperature and reflectivity at the

Au surface will have a phase lag relative to the pump beam, depending on the sample's thermal transport properties [71–75]. Fig.1.9 shows a schematic of the FDTR set up [6].

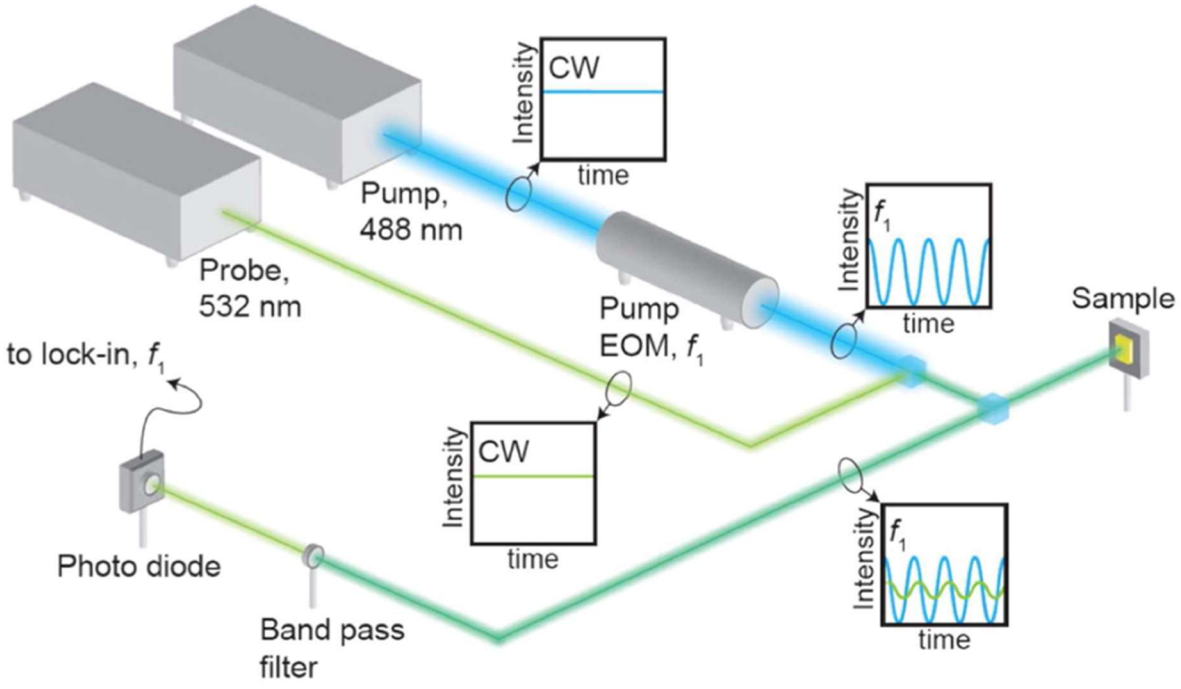

Fig.1.9. The experimental setup of FDTR. Reprinted and adapted with permission from "*Temperature Dependent Thermal Conductivity and Thermal Interface Resistance of Pentacene Thin Films with Varying Morphology*", J. Epstein et al., ACS Appl. Mater. Interfaces 8, 29, 19168-19174. Copyright 2016 American Chemical Society [76].

[1] K.Y. Foo and B.H. Hameed: *Chem. Eng. J.*, 2010, vol. 156, pp. 2–10.

[2] S. Jaćimovski and D. Raković: *Acta Phys. Pol. A*, 2011, vol. 120, pp. 231–33.

[3] Xin Liang, Y. F. Wang, R. Z. Zhang, A. Kosuga, R. Funahashi, Y. S. Ba, K. Koumoto, B. M. Foley, C. H. Lee, Y. Zhu, A. W. Lichtenberger, J. E. Moore, D. A. Muller, D. G. Schlom, P. E. Hopkins, A. Majumdar, R. Ramesh, and M. A. Zurbuchen: *Phys. Chem. Chem. Phys.*, 2015, vol. 17, pp. 27889–93.

[4] C Kittel: *Introduction to Solid State Physics*, 2005.

[5] S. N. Piramanayagam and Tow C. Chong: *Developments in Data Storage: Materials Perspective*, John Wiley & Sons, n.d.

[6] Thomas Tsakalakos, Ilya A. Ovid'ko, and Asuri K. Vasudevan: *Nanostructures: Synthesis, Functional Properties and Applications*, Springer Science & Business Media, 2003.

[7] Venkatesha N, Veena Hegde, and Chandan Srivastava: *IET Nanobiotechnology*, 2014, vol. 8, pp. 184–89.

[8] Dieter Weller, Gregory Parker, Oleksandr Mosendz, Andreas Lyberatos, Dmitriy Mitin, Nataliia Y. Safonova, and Manfred Albrecht: *J. Vac. Sci. Technol. B, Nanotechnol. Microelectron. Mater. Process. Meas. Phenom.*, 2016, vol. 34, p. 060801.

[9] G. Moulas, A. Lehnert, S. Rusponi, J. Zabloudil, C. Etz, S. Ouazi, M. Etzkorn, P. Bencok, P. Gambardella, P. Weinberger, and H. Brune: *Phys. Rev. B*, 2008, vol. 78, p. 214424.

[10] Dror Sarid and William Challener: *Modern Introduction to Surface Plasmons: Theory, Mathematica Modeling, and Applications*, Cambridge University Press, n.d.

[11] Shaomin Xiong, Jeongmin Kim, Yuan Wang, Xiang Zhang, and David Bogy: *J. Appl. Phys.*, 2014, vol. 115, p. 17B702.

[12] Alexander Q. Wu, Yukiko Kubota, Timothy Klemmer, Tim Rausch, Chubing Peng, Yingguo Peng, Darren Karns, Xiaobin Zhu, Yinfeng Ding, Eric K. C. Chang, Yongjun Zhao, Hua Zhou, Kaizhong Gao, Jan-Ulrich Thiele, Mike Seigler, Ganping Ju, and Edward Gage: *IEEE Trans. Magn.*, 2013, vol. 49, pp. 779–82.

[13] W A Challener, Chubing Peng, A V Itagi, D Karns, Wei Peng, Yingguo Peng, XiaoMin Yang, Xiaobin Zhu, N J Gokemeijer, Y.-T. Hsia, G Ju, Robert E Rottmayer, Michael A Seigler, and E C Gage: *Nat. Photonics*, 2009, vol. 3, pp. 220–24.

[14] Zhi-Min Yuan, Jianzhong Shi, Chun Lian Ong, Pantelis Sophoclis Alexopoulos, Chunling Du, Anmin Kong, Shiming Ang, Budi Santoso, Siang Huei Leong, Kheong Sann Chan, Yibin Ng, Kui Cai, Jack Tsai, Hanxiang Ng, and Hang Khume Tan: *IEEE Trans. Magn.*, 2015, vol. 51, pp. 1–7.

[15] Liwen Huang, Barry Stipe, Matteo Staffaroni, Takuichi Hirano, Erhard Schreck, and F.Y. Huang: n.d., pp. 1–2.

[16] Y S Touloukian, R W Powell, C Y Ho, and P G Klemens: 1971.

[17] Arden L. Moore and Li Shi: *Mater. Today*, 2014, vol. 17, pp. 163–74.

[18] M Kazan: *J. Heat Transfer*, 2011, vol. 133, p. 112401.

[19] Glen A. Slack, R.A. Tanzilli, R.O. Pohl, and J.W. Vandersande: *J. Phys. Chem. Solids*, 1987, vol. 48, pp. 641–47.

[20] James A. Bain, Jonathan A. Malen, Minyoung Jeong, and Turga Ganapathy: *MRS Bull.*, 2018, vol. 43, pp. 112–18.

[21] Lien Chin Wei, Lili E. Ehrlich, Matthew J. Powell-Palm, Colt Montgomery, Jack Beuth, and Jonathan A. Malen: *Addit. Manuf.*, 2018, vol. 21, pp. 201–8.

[22] Shinobu Masamune and J. M. Smith: *Ind. Eng. Chem. Fundam.*, 1963, vol. 2, pp. 136–43.

[23] Joseph Callaway and Hans C. von Baeyer: *Phys. Rev.*, 1960, vol. 120, pp. 1149–54.

[24] J. M. (John M.) Ziman: *Electrons and Phonons : The Theory of Transport Phenomena in Solids*, Clarendon Press, 2001.

[25] Marc J. Madou: *Fundamentals of Microfabrication and Nanotechnology*, CRC Press, 2012.

[26] Ankit Jain and Alan J. H. McGaughey: *Phys. Rev. B*, 2016, vol. 93, p. 081206.

[27] Daryoosh Vashaee and Ali Shakouri: n.d.

[28] F Völklein, H Reith, T W Cornelius, M Rauber, and R Neumann: 2009.

[29] E T Swartz and R O Pohl: *Rev. Mod. Phys.*, 1989, vol. 61, pp. 605–68.

[30] Jean-Louis Barrat and Francois Chiaruttini: *Mol. Phys.*, 2003, vol. 101, pp. 1605–10.

[31] W. a. Challener, Chubing Peng, a. V. Itagi, D. Karns, Wei Peng, Yingguo Peng, XiaoMin Yang, Xiaobin Zhu, N. J. Gokemeijer, Y.-T. Hsia, G. Ju, Robert E. Rottmayer, Michael a. Seigler, and E. C. Gage: *Nat. Photonics*, 2009, vol. 3, pp. 303–303.

[32] M.H. Kryder, E.C. Gage, T.W. McDaniel, W.A. Challener, R.E. Rottmayer, Ganping Ju, Yiao-Tee Hsia, and M.F. Erden: *Proc. IEEE*, 2008, vol. 96, pp. 1810–35.

[33] J Lombard, F Detcheverry, and S Merabia: *J. Phys. Condens. Matter*, 2015, vol. 27, p. 015007.

[34] Yan Wang, Xiulin Ruan, and Ajit K. Roy: *Phys. Rev. B*, 2012, vol. 85, p. 205311.

[35] Arun Majumdar and Pramod Reddy: *Appl. Phys. Lett.*, 2004, vol. 84, p. 4768.

[36] R. E. Jones, J. C. Duda, X. W. Zhou, C. J. Kimmer, and P. E. Hopkins: *Appl. Phys. Lett.*, 2013, vol. 102, p. 183119.

[37] Patrick E. Hopkins, John C. Duda, Bryan Kaehr, Xiao Wang Zhou, C.-Y. Peter Yang, and Reese E. Jones: *Appl. Phys. Lett.*, 2013, vol. 103, p. 211910.

[38] Piyush Singh, Myunghoon Seong, and Sanjiv Sinha: *Appl. Phys. Lett.*, 2013, vol. 102, p. 181906.

[39] R. B. Wilson, Brent a. Apgar, Wen-Pin Hsieh, Lane W. Martin, and David G. Cahill: *Phys. Rev. B*, 2015, vol. 91, pp. 1–7.

[40] Edward Dechaumphai, Dylan Lu, Jimmy J. Kan, Jaeyun Moon, Eric E. Fullerton, Zhaowei Liu, and Renkun Chen: *Nano Lett.*, 2014, vol. 14, pp. 2448–55.

[41] Minyoung Jeong, Justin P. Freedman, Hongliang Joe Liang, Cheng-Ming Chow, Vincent M. Sokalski, James A. Bain, and Jonathan A. Malen: *Phys. Rev. Appl.*, 2016, vol. 5,

p. 014009.

[42] A. V. Sergeev: *Phys. Rev. B*, 1998, vol. 58, pp. R10199–202.

[43] Wei Wang and David G. Cahill: *Phys. Rev. Lett.*, 2012, vol. 109, p. 175503.

[44] I M Lifshits M. I. Kaganov: *Sov. Physics, JETP*, 1957, vol. 31.

[45] Mathieu Francoeur: *Nat. Nanotechnol.*, 2015, vol. 10, pp. 206–8.

[46] Arvind Narayanaswamy, Sheng Shen, Lu Hu, Xiaoyuan Chen, and Gang Chen: *Appl. Phys. A*, 2009, vol. 96, pp. 357–62.

[47] Emmanuel Rousseau, Alessandro Siria, Guillaume Jourdan, Sebastian Volz, Fabio Comin, Joël Chevrier, and Jean-Jacques Greffet: *Nat. Photonics*, 2009, vol. 3, pp. 514–17.

[48] Sheng Shen, Arvind Narayanaswamy, and Gang Chen: *Nano Lett.*, 2009, vol. 9, pp. 2909–13.

[49] Kyeongtae Kim, Bai Song, Víctor Fernández-Hurtado, Woochul Lee, Wonho Jeong, Longji Cui, Dakotah Thompson, Johannes Feist, M. T. Homer Reid, Francisco J. García-Vidal, Juan Carlos Cuevas, Edgar Meyhofer, and Pramod Reddy: *Nature*, 2015, vol. 528, pp. 387–91.

[50] Mathias Schnippering, Simon R. T. Neil, Stuart R. Mackenzie, and Patrick R. Unwin: *Chem. Soc. Rev.*, 2011, vol. 40, pp. 207–20.

[51] M L Martin-Fernandez, C J Tynan, and S E D Webb: *J. Microsc.*, 2013, vol. 252, pp. 16–22.

[52] Keunhan Park and Zhuomin Zhang: *Front. Heat Mass Transf.*, 2013, vol. 4.

[53] H. (Heinz) Raether: *Surface Plasmons on Smooth and Rough Surfaces and on Gratings*, Springer-Verlag, 1988.

[54] J.D. McMullen: *Solid State Commun.*, 1975, vol. 17, pp. 331–36.

[55] Karl Joulain, Ré Mi Carminati, Jean-Philippe Mulet, and Jean-Jacques Greffet: 2003.

[56] Bai Song, Yashar Ganjeh, Seid Sadat, Dakotah Thompson, Anthony Fiorino, Víctor Fernández-Hurtado, Johannes Feist, Francisco J Garcia-Vidal, Juan Carlos Cuevas, Pramod Reddy, and Edgar Meyhofer: 2015.

[57] Stephen Brunauer and L. E. Copeland: in *Symp. Prop. Surfaces*, ASTM International, 100 Barr Harbor Drive, PO Box C700, West Conshohocken, PA 19428-2959, 1963, pp. 59-59–21.

[58] Ahmed Rezk, Raya Al-Dadah, Saad Mahmoud, and Ahmed Elsayed: *Int. J. Heat Mass Transf.*, 2012, vol. 55, pp. 7366–74.

[59] Jian-Rong Li, Ryan J. Kuppler, and Hong-Cai Zhou: *Chem. Soc. Rev.*, 2009, vol. 38, p. 1477.

[60] Filipe A. Almeida Paz, Jacek Klinowski, Sérgio M. F. Vilela, João P. C. Tomé, José A. S.

Cavaleiro, and João Rocha: *Chem. Soc. Rev.*, 2012, vol. 41, pp. 1088–1110.

[61] Rob Ameloot, Frederik Vermoortele, Wim Vanhove, Maarten B. J. Roeffaers, Bert F. Sels, and Dirk E. De Vos: *Nat. Chem.*, 2011, vol. 3, pp. 382–87.

[62] Nak Cheon Jeong, Bappaditya Samanta, Chang Yeon Lee, Omar K. Farha, and Joseph T. Hupp: *J. Am. Chem. Soc.*, 2012, vol. 134, pp. 51–54.

[63] Yuanjing Cui, Yanfeng Yue, Guodong Qian, and Banglin Chen: *Chem. Rev.*, 2012, vol. 112, pp. 1126–62.

[64] Patricia Horcajada, Christian Serre, María Vallet-Regí, Muriel Sebban, Francis Taulelle, and Gérard Férey: *Angew. Chemie Int. Ed.*, 2006, vol. 45, pp. 5974–78.

[65] Xuerui Wang, Linzhi Zhai, Yuxiang Wang, Ruitong Li, Xuehong Gu, Yi Di Yuan, Yuhong Qian, Zhigang Hu, and Dan Zhao: *ACS Appl. Mater. Interfaces*, 2017, vol. 9, pp. 37848–55.

[66] Myunghyun Paik Suh, Hye Jeong Park, Thazhe Kootteri Prasad, and Dae Woon Lim: *Chem. Rev.*, 2012, vol. 112, pp. 782–835.

[67] B.L. Huang, Z. Ni, A. Millward, A.J.H. McGaughey, C. Uher, M. Kaviany, and O. Yaghi: *Int. J. Heat Mass Transf.*, 2007, vol. 50, pp. 405–11.

[68] D. Liu, J.J. Purewal, J. Yang, A. Sudik, S. Maurer, U. Mueller, J. Ni, and D.J. Siegel: *Int. J. Hydrogen Energy*, 2012, vol. 37, pp. 6109–17.

[69] Manjula I. Nandasiri, Jian Liu, B. Peter McGrail, Jeromy Jenks, Herbert T. Schaef, Vaithiyalingam Shutthanandan, Zimin Nie, Paul F. Martin, and Satish K. Nune: *Sci. Rep.*, 2016, vol. 6, p. 27805.

[70] Kristopher J. Erickson, François Léonard, Vitalie Stavila, Michael E. Foster, Catalin D. Spataru, Reese E. Jones, Brian M. Foley, Patrick E. Hopkins, Mark D. Allendorf, and A. Alec Talin: *Adv. Mater.*, 2015, vol. 27, pp. 3453–59.

[71] Wee-Liat Ong, Sara M. Rupich, Dmitri V. Talapin, Alan J. H. McGaughey, and Jonathan A. Malen: *Nat. Mater.*, 2013, vol. 12, pp. 410–15.

[72] Jonathan A. Malen, Kanhayalal Baheti, Tao Tong, Yang Zhao, Janice A. Hudgings, and Arun Majumdar: *J. Heat Transfer*, 2011, vol. 133, p. 081601.

[73] Aaron J Schmidt, Xiaoyuan Chen, and Gang Chen: *Rev. Sci. Instrum.*, 2008, vol. 79, p. 114902.

[74] Keith T Regner, Daniel P Sellan, Zonghui Su, Cristina H Amon, Alan J H McGaughey, and Jonathan A Malen: *Nat. Commun.*, 2013, vol. 4, p. 1640.

[75] K. T. Regner, S. Majumdar, and J. a. Malen: *Rev. Sci. Instrum.*, 2013, vol. 84.

[76] Jillian Epstein, Wee-Liat Ong, Christopher J. Bettinger, and Jonathan A. Malen: *ACS Appl. Mater. Interfaces*, 2016, vol. 8, pp. 19168–74.

Enhancement of thermal interface conductance across metal-dielectric interfaces using nanometer metal adhesion layers

2.1 Abstract

We show that the use of subnanometer adhesion layers significantly enhances the thermal interface conductance at metal-dielectric interfaces. A metal-dielectric interface between Au and sapphire (Al_2O_3) is considered using Cu (low optical loss) and Cr (high optical loss) as adhesion layers. To enable high throughput measurements, each adhesion layer is deposited as a wedge such that a continuous range of thicknesses could be sampled. Our measurements of thermal interface conductance at the metal-Al_2O_3 interface made using frequency-domain thermoreflectance show that a 1-nm-thick adhesion layer of Cu or Cr is sufficient to enhance the thermal interface conductance by more than a factor of 2 or 4, respectively, relative to the pure Au-Al_2O_3 interface. The enhancement agrees with the diffuse-mismatch-model-based predictions of accumulated thermal conductance versus adhesion-layer thickness assuming that it contributes phonons with wavelengths less than its thickness, while those with longer wavelengths transmit directly from the Au.

2.2 Introduction

Among many technologies where the nanoscale heat transport has been a key subject of discussion is heat assisted magnetic recording (HAMR). Hard drive manufacturing companies such as Seagate Technologies and Western Digital have been attempting hard to accommodate the recent rapid increasing need to store digital information that is generated and shared

worldwide strongly by increasing their data storage capacity. To achieve a higher storage capacity, the aerial density of hard drives should increase by reducing the size of grains in a bit cell [1]. However, when the grain size becomes very small, thermal fluctuations cause the magnetization of grains to be unstable [2]. This phenomenon is called superparamagnetism. It is reported that in Mn-Zn ferrite magnetic media, the limit for the grain size to avoid superparamagnetism is approximately 10 nm at 300 K [3]. To overcome this unstable fluctuation magnetic media with high magnetic anisotropy should be used [4]. Unfortunately, magnetizing such media requires an intense magnetic switching field [5]. Heat-assisted Magnetic Recording (HAMR) could provide a solution for this issue by locally heating the magnetic media to near its Curie temperature thereby reducing the required magnetic switching field strength (Fig. 2.1) [6,7].

(a)

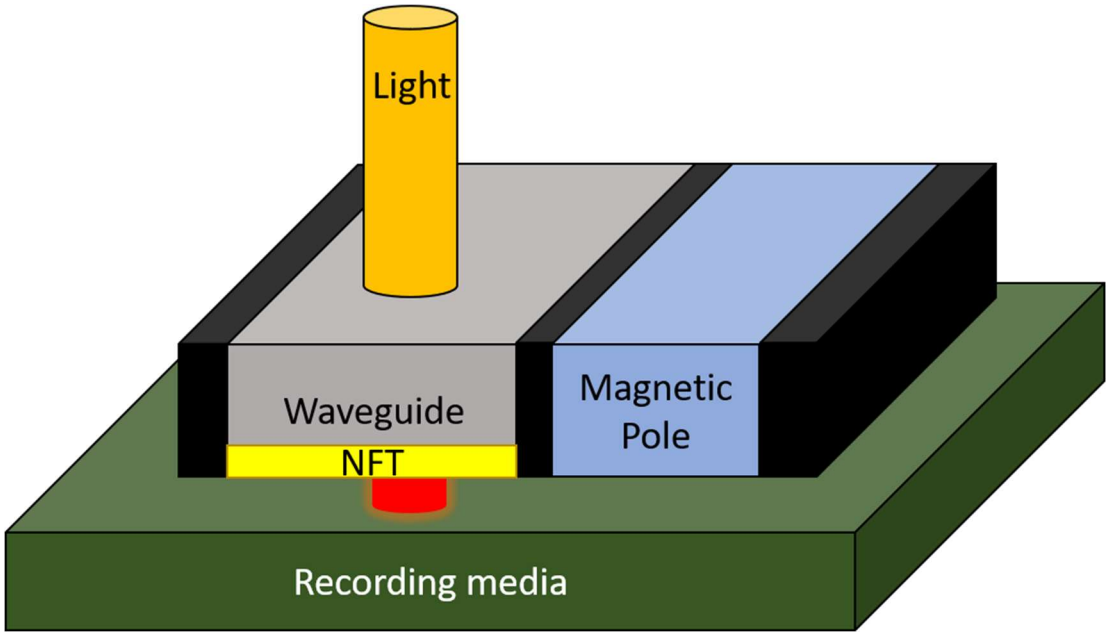

(b)

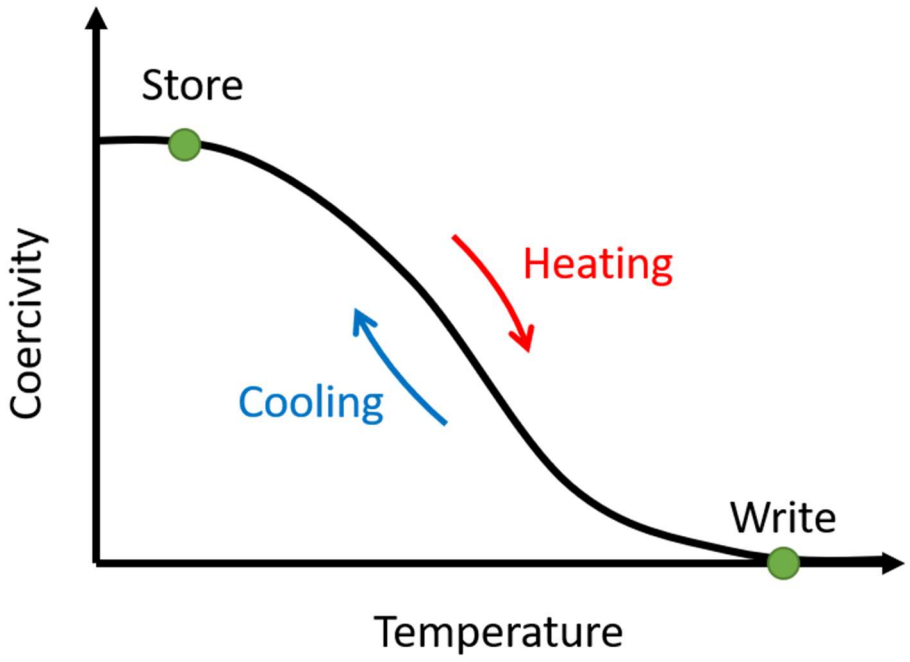

Fig. 2.1. (a) Schematic of HAMR system (b) Schematic of HAMR recording process [8]. These adapted figures, *"FIG. 2. (Color online) (a) Typical HAMR head-media recording image and (b) temperature dependent FePt media coercivity."* by Dieter Weller, are licensed under CC BY 4.0 and can be found in Ref. [8].

In HAMR, a localized heating is enabled by a near-field transducer (NFT). First, guided by optics such as a planar solid immersion mirror (PSIM), the short-wavelength infrared light will be focused and coupled to the Au-NFT. Then, the photons in this light source will be able to be coupled with electrons in the metal layer at a certain resonance frequency. This coupling creates surface plasmon polaritons (SPPs), which will travel to the tip of the NFT structure along the Au-dielectric interface as electromagnetic radiation. These SPPs have an ability to be confined onto a very small spot with significantly high field intensity. The intense electric field

created at the tip by the SPPs will then create oscillations in the electrons in the media thereby heating it up [9–11].

While the SPPs travel down the Au-dielectric interface a parasitic loss occurs in the Au itself and dissipated to the dielectric, which results in peak NFT temperatures that are hundreds of degrees above the ambient temperature [9]. This could potentially lead to thermal breakdown of a HAMR device and thus should be addressed through efficient thermal management. In this perspective, using a dielectric material that has a high thermal conductivity (κ) such as aluminum nitride (AlN) or sapphire (Al_2O_3) is preferred over low thermal conductivity dielectrics like SiO_2. However, the interface between the Au and the dielectric, then becomes the bottleneck for heat dissipation, and thus it is important to increase the thermal conductance across an interface in the HAMR NFT system.

The thermal interface conductance (G) denotes the rate of heat transfer across the interface. It is defined as $G = \frac{q''}{\Delta T}$, where q'' is the heat flux across an interface per unit area, and ΔT is the temperature difference across the interface [12]. We chose the Au/Al_2O_3 interface in our study because it represents a practical HAMR NFT system considered by various hard drive manufacturing companies. For the Au/Al_2O_3 interface, G values are reported to range from 22MW/m^2-K to 66MW/m^2-K, at 300 K, which is relatively low compared to other metal-dielectric interfaces. [13–15]

Heat is carried by electrons in metals and phonons in crystalline dielectrics. Various studies have proposed that electrons first transfer their energy to phonons in the metal with an equivalent conductance of G_{e-p} and then the phonons in the metal transmit into the dielectric with G_p through interface. Since these processes happen in series, G becomes ($G = G_{e-p}$ ·

G_p)/(G_{e-p}+G_p) [16–23]. It is previously reported that the ratio of G_{e-p}/G_p in the Au-Al_2O_3 interface is nearly 5 [16,24]. The larger G_{e-p} value leads the G_p term to become a bottleneck in the overall G and hence the focus of my study. The general equation for phonon flux from side 1 to side 2 across an interface, $q_{1\to2}$, is defined as follows under the assumptions of isotropic phonon dispersion and diffuse scattering:

$$q_{1\to2} = \frac{1}{8\pi^2}\sum_j \int_{k_{j,1}>0} \hbar\omega_{j,1}(k_{j,1}){k_{j,1}}^2 \zeta_{1\to2}\left|v_{j,1}(k_{j,1})\right| n_0 dk_{j,1} , \qquad (2.1)$$

where k is the wavevector, $\hbar$ is the reduced Planck's constant, ω the frequency, ζ is the transmission coefficient indicating the probability of phonon transmission across the interface, v is the group velocity, and n_0 is the phonon Bose-Einstein distribution function $n_0 = \frac{1}{\left[\exp\left(\frac{\hbar\omega}{k_B T}\right)-1\right]}$.[24] The subscript $j, 1$ indicates the properties are defined for the material on side 1 for the j phonon polarization.[24] Since G is defined as $\frac{q_{1\to2}}{\Delta T_{1\to2}}$ where $\Delta T_{1\to2}$ is the change of temperature across the interface, the highest G results when $q_{1\to2}$ is maximum, which occurs when ζ is maximum for all phonon modes.

The DMM (Diffuse Mismatch Model) is one of the various models suggested to estimate ζ. The main assumption of the DMM is that all of the incident phonons will scatter elastically and diffusely at the interface into the other side irrespective of theinterface details. In other words, they will lose 'memory' of their origins once they reach the interface [12,25]. This leads us to set up an equation $\zeta_{1\to2} = 1 - \zeta_{2\to1}$ because phonons that are reflected back at an interface will be viewed the same as those transmitting through. In addition, according to the principle of detailed balance, heat flux from side 1 to 2 should be equal to that from side 2 to 1 ($q_{1\to2} = q_{2\to1}$). Another well-known model is Acoustic Mismatch Model (AMM). In this model, phonons

which are treated as plane waves, and assumed to elastic-scatter specularly at the interface due to acoustic impedance discrepancies between dissimilar materials [12,26,27]. The AMM is the acoustic equivalent of Snell's law. However, the specular scattering of phonons across the interface is more likely to happen when the temperature is low (below 7 K) and the interface roughness is small compared to phonon wavelengths [12,27]. Because this is not common in modern electronic devices like HAMR-NFT, we use the DMM.

If our system reaches equilibrium, there will be a net phonon flux of zero across the interface, and thus $q_{1\to2} = q_{2\to1}$. If we apply the detailed balance on the phonon flux defined in Equation (2.1) above, all common terms will be cancelled out and Equation (2.1) becomes:

$$\zeta_{1\to2}(k_1) = \frac{\sum_j \int_{k_{k,2>0}} \omega_{j,2} {k_{j,2}}^2 \zeta_{2\to1} v_{j,2} dk_{j,2}}{\sum_j \int_{k_{k,1>0}} \omega_{j,1} {k_{j,1}}^2 v_{j,1} dk_{j,1}} . \tag{2.2}$$

We already defined the relationship, $\zeta_{1\to2}$=1-$\zeta_{2\to1}$, under the diffuse scattering condition in DMM. Furthermore, we only consider elastic scattering in DMM in which phonons are assumed to preserve their frequency upon scattering ($\omega_{j,1}(k_{j,1}) = \omega_{j,2}(k_{j,2})$). Thus, Equation (2.2) finally reduces to

$$\zeta_{1\to2}(k_1) = \frac{\sum_j {k_{j,2}}^2 v_{j,2} dk_{j,2}}{\sum_j {k_{j,1}}^2 v_{j,1} dk_{j,1} + \sum_j {k_{j,2}}^2 v_{j,2} dk_{j,2}} . \tag{2.3}$$

The integrals over wavevector space are not needed anymore because elastic phonon scattering means phonon transport occurs on a per frequency basis. Given that the group velocity v is defined as $v(k) = \frac{d\omega(k)}{dk}$, Equation (2.3) above can be rearranged as follows in terms of phonon frequency, ω :

$$\zeta_{1\to2}(\omega) = \frac{\sum_j {k_{j,2}(\omega)}^2}{\sum_j {k_{j,1}(\omega)}^2 + \sum_j {k_{j,2}(\omega)}^2} . \tag{2.4}$$

Since three dimensional phonon density of states, $D(\omega)$ is defined as $D(\omega) = \left(\frac{Vk^2}{2\pi^2}\right)\left(\frac{dk}{d\omega}\right)$, where V is the volume of the specimen [28], Equation (2.4) above can be interpreted as a relationship between the phonon density of states for each material on side 1 and 2. Hence, according to the DMM, greater overlap in the density of states between two materials leads to a higher value of ζ, and thus G.

The materials of our interest are Au and Al_2O_3 to mimic the actual HAMR-NFT system. We hypothesized that inserting materials as adhesion layers that have a better Debye temperature match with the Al_2O_3 than Au will improve thermal transport across the Au-Al_2O_3 interface since it is known that similar Debye temperatures in different materials leads to a better overlap in their density of states, and thus better thermal interface conductance [14,15,29]. In addition, there have already been studies utilizing adhesion layers for enhanced thermal transport at the interface level [30]. Thus, even though the naming of adhesion layer suggests that we attempt to enhance *G* by promoting adhesion between the Au and Al_2O_3, the purpose of adhesion layer is rather bridging the dissimilar phonon properties between those two.

Therefore, good candidate materials should possess similar Debye temperatures to the substrate as well as strong adhesion, and affordable cost. For HAMR applications, the optical properties of an adhesion layer are critical because the interference with plasmon generation and propagation at Au-dielectric interface should be minimized. In this perspective, Cu and Cr adhesion layers are deemed appropriate because they represent low and high optical loss metals in the near-infrared (IR), yet both have more similar Debye temperatures with Al_2O_3 than Au. Therefore, we aimed to study the enhancement of thermal interface conductance at the Au-Al_2O_3 interface with Cu and Cr adhesion layers, and furthermore determine how thick those metal adhesion layers need to be to realize such enhancement.

In our laboratory, nanoscale thermal transport is measured by frequency domain thermoreflectance (FDTR) technique. The detailed information about FDTR is provided in Chapter 1.6. In this technique, a 488nm continuous wave (CW) pump laser is intensity modulated by an electrooptic modulator over a range of frequencies. Upon absorbing the modulated pump beam the sample surface is heated periodically at the same modulation frequency as the pump beam. Because of this periodic heating, the temperature at the surface changes which causes periodic changes in surface optical reflectance (i.e. thermoreflectance). This optical response is detected by a 532nm CW probe laser beam that is co-aligned with the pump at the sample surface since the thermoreflectance of Au is peaked at 532 nm, the probe beam will be modulated in intensity. The temperature and reflectivity at the Au surface will have a phase lag relative to the pump beam, depending on the sample's thermal transport properties [31–34].

The phase-lag data between the reflected pump and the probe beams at various positions on the sample are collected using a lock-in amplifier. In our study, minimum of 20 data points spanning a range of frequencies (200 kHz to 10 MHz) are obtained, and then fit to an analytical solution of the heat diffusion equation [35]. In this fitting, the only unknown parameter is the thermal property of the interested material and we vary this parameter until the highest coefficient of determination (R^2) value is achieved.

2.3 Experimental procedures

All the film depositions are conducted on 3-inch Al_2O_3 c-plane (0001) wafers by DC magnetron sputtering from 5-inch targets in an argon atmosphere with a base pressure

maintained at $< 2\times 10^{-7}$ Torr. Before deposition, the substrates are cleaned acetone in an ultrasonic bath for 10 minutes then rinsed with isopropyl alcohol (IPA). The deposition rates for Cr and Cu are 0.67 Å/sec at 5mTorr and 2.25 Å/sec at 2.5mTorr, respectively. Metal adhesion layers with a targeted thickness gradient between 0 and 6~8 nm are prepared by moving the substrate into the target's deposition window at a controlled velocity before reversing direction so that the leading edge is exposed to the plasma longer than the trailing edge. A 70 nm uniform Au transducer layer is deposited on each of the adhesion layers without breaking vacuum. Additional Cu and Cr samples are fabricated without Au for AFM analysis. The spatially varying thickness of each adhesion layer and the Au layer are measured by x-ray reflectivity (XRR) with the uncertainty of $\pm$ 0.3 nm, estimated from error analysis. [36]

2.4 Results and Discussion

XRR measurements of the thicknesses of Cu and Cr adhesion layers on the Al_2O_3 substrate are shown in Fig. 2.2. The x-axis, 'Distance from Flat Edge" indicates positions on the substrate in terms of the normal distance from the flat edge on the Al_2O_3 substrates. The XRR-determined thicknesses of Au layers are 71 $\pm$ 2 nm and 70 $\pm$ 2 nm with maximum adhesion layer thicknesses of 7.3 $\pm$ 0.3 nm and 8.2 $\pm$ 0.3 nm at the thickest thickness point. The inset of Fig. 2.5 shows one of the XRR fits at an intermediate position on the Cu wedge. The thickness profile is non-linear, which we attribute to variations in the deposition rate across the sputtering target shutter opening. The data are fit with a third order polynomial ($R^2 > 0.99$) to extract the adhesion layer thicknesses as a function of position on the substrate.

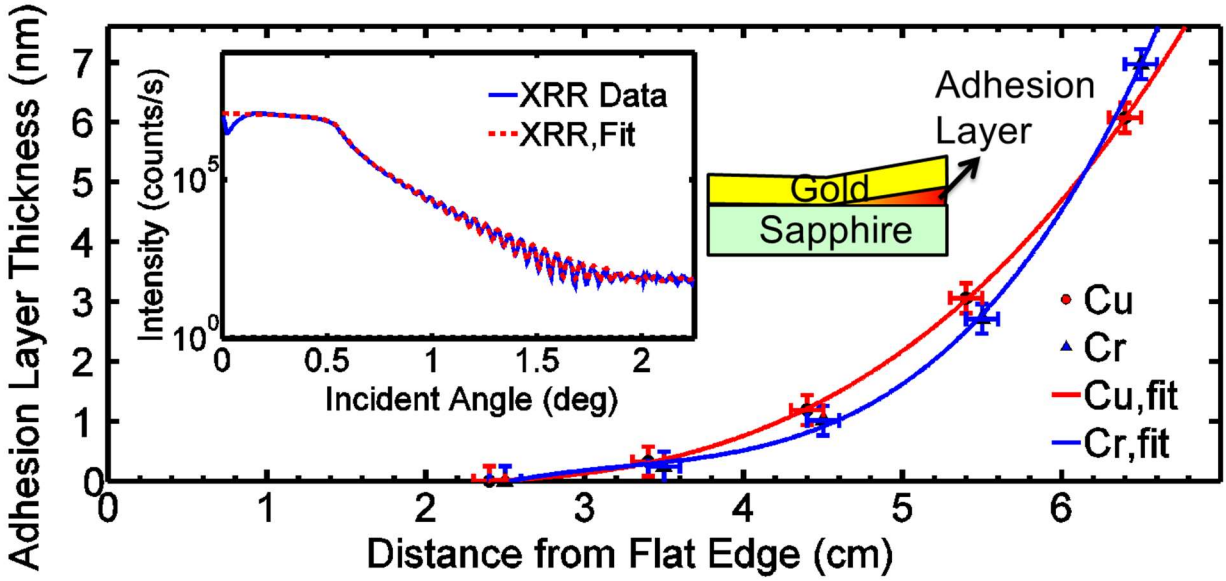

Fig. 2.2. The thicknesses of wedge-shaped Cu and Cr adhesion layers as a function of position on the substrate. Third order polynomial fits for experimental data are shown as solid lines. The inset schematic shows the adhesion layer wedge. The inset plot shows XRR data and fits for a 1.2nm thick position on the Cu wedge. Used and reprinted with permission from American Physical Society [36].

The thermal interface conductance of Cu and Cr samples measured by FDTR as a function of normal distance from the flat part of the Al_2O_3 substrate are shown in Fig.2.3-(a). The uncertainties shown in error-bars come from propagations of uncertainties in fitting parameters such as laser spot size (2.8 ± 0.1 μm) material density (± 2%), specific heat, thermal conductivity and thickness (± 0.25 nm). In the region where only the Au-Al_2O_3 interface is present, average G values of 70 ± 10 MW/m^2-K and 60 ± 10 MW/m^2-K for Cu and Cr samples are measured. This is in good agreement with previous measurements of a Au-Al_2O_3 interface reported by Stoner and Maris [14]. The values saturated finally at ~400 MW/m^2-K and at ~190MW/m^2-K. The inset plot shows variations in fitting the phase lag data to the frequency

when the interfacial thermal conductance changed to +20% and -20% of the original thermal conductance while other fitting parameters are left invariant. As seen in the appreciable differences between each fit, our fitting process has a good control over sensitivity, and this also allows us to set up the confidence level in our analysis.

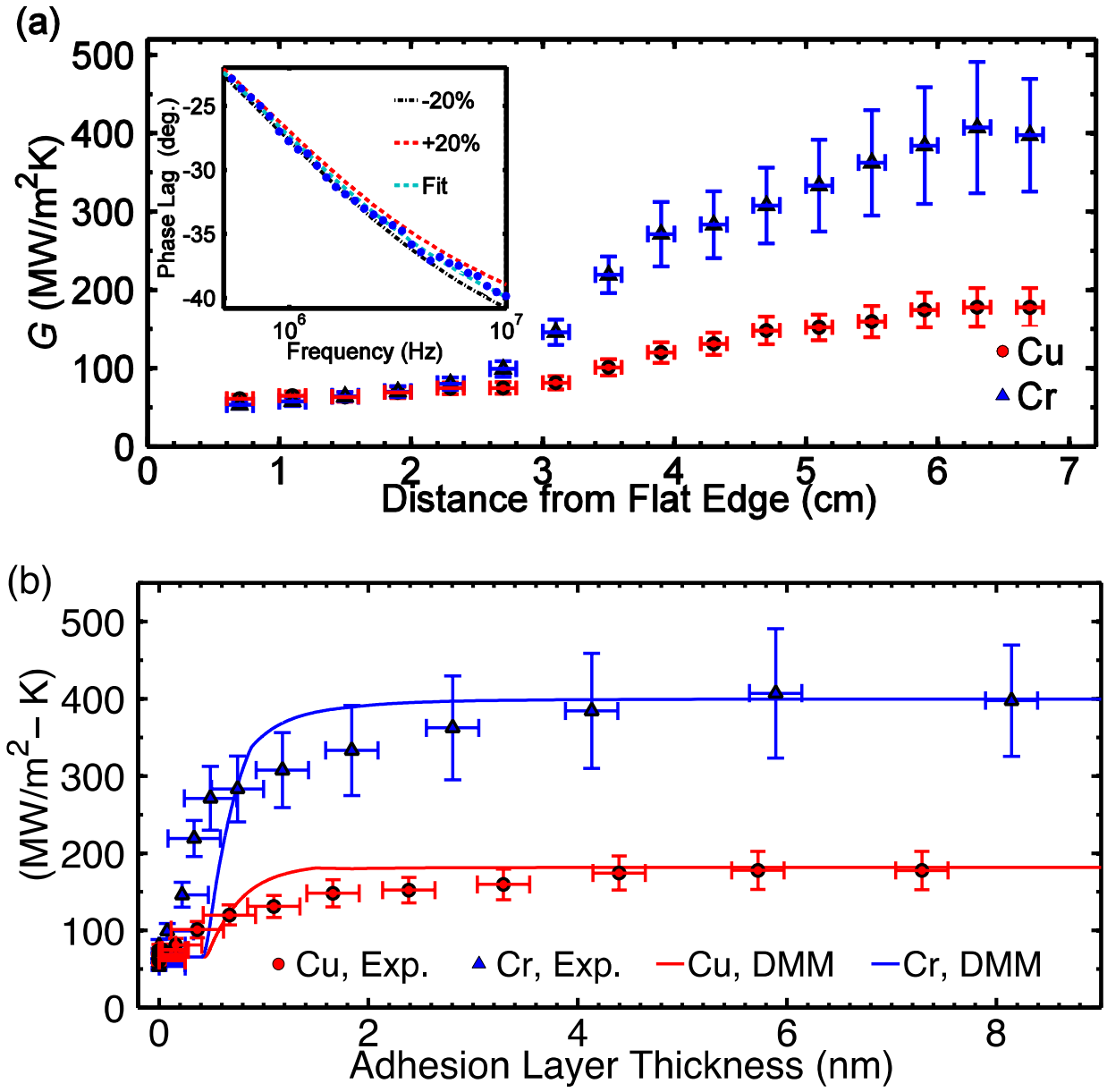

Fig. 2.3. (a) Thermal interface conductance as a function of positions on the wafer. The inset plot shows how sensitive our fitting is in terms of ± 20 % of G. The Cr sample showed a higher

enhancement in G than the Cu sample, and both exhibited a saturating behavior as the layer becomes thicker (b) The experimentally obtained G is compared with the predictions of $G_{\text{accum.}}$ based on the DMM. Used and reprinted with permission from American Physical Society [36].

The data points in Fig. 2.3-(b) represent the experimental G as a function of adhesion layer thicknesses obtained by XRR. In this plot, it is shown that when the adhesion layer thickness is only approximately 1 nm, two and four-fold enhancements of G between the Au-Al_2O_3 layers with Cu and Cr are observed. Once the layer thickness reached approximately 5 nm, the measured G saturated at 180 ± 20MW/m^2-K and 390 ± 70MW/m^2-K, for Cu and Cr adhesion layers respectively. From a plasmonic technological standpoint, this is critical because the optical performance at the plasmonic will be disrupted less with thinner layers. This can solely be attributed to enhancement in G_p, not G_{e-p}, because maximum increase in G due to an increase in G_{e-p} would only be ~20% if we assume $G_{e-p} \cong 5$.

Because the DMM is based on bulk phonon properties, it is invoked to determine whether phonon properties alone could validate observed experimental enhancements in G with just 1nm-thick adhesion layer. A general expression for G_p can be expressed as follows

$$G_p = \frac{1}{8\pi^2}\sum_j \int_{k_{j,1}} \hbar\omega_{j,1}(k_{j,1}){k_{j,1}}^2 \zeta_{1\to2} \left|v_{j,1}(k_{j,1})\right| \frac{\partial n_0}{\partial T} dk_{j,1} \quad . \tag{2.5}$$

Because $v_{j,1}(k_{j,1}) = \frac{d\omega_{j,1}}{dk_{j,1}}$, substitution into Equation (2.5) results in the following Equation (2.6)

$$G_p = \frac{1}{8\pi^2}\sum_j \int_{\omega_{j,1}} \hbar\omega_{j,1}({k_{j,1}}^2){k_{j,1}}^2 \zeta_{1\to2} \frac{\partial n_0}{\partial T} d\omega_{j,1} = \sum_j \int_{\omega_{j,1}} g_{j,1}(\omega) d\omega_{j,1} \quad , \tag{2.6}$$

where $g_{j,1}(\omega)$ is a spectral thermal interface conductance defined per unit ω.

Accurate calculation of G_p using Equation (2.5) and (2.6) requires us to define a relationship between ω and k. Therefore, we used real dispersion relationships for our materials (Au, Cu, Cr and Al_2O_3). The real dispersion relationships are formulated by fitting a fourth-order polynomial to experimentally reported values as a function of their wavevectors for each polarization [37–40]. The phonon propagation directions are chosen according to Al_2O_3 wafer manufacturer's description as well as prior studies on preferential growths of Cu and Cr on the c-plane of Al_2O_3; Γ- L [111] in Cu and Au, Γ- N [110] in Cr, and Γ- Z [0001] for Al_2O_3 [41–44]. By making the isotropic assumption we introduce an approximation.

For meaningful comparisons of our theoretical predictions based on DMM with the experimental results as a function of adhesion layer thickness, we need to estimate G_p in terms of phonon wavelengths (λ), rather than frequency, ω. Only phonons with λ less than the adhesion layer thickness (t) are assumed to exist in the adhesion layer, ignoring any possible changes to the phonon dispersion in very thin adhesion layers. If we set $\lambda_{\max}$ equal to t, it enables us to relate our result with the accumulation of G_p with λ.

The thermal interface conductance accumulation function as a function of ω is suggested recently as follows [45] :

$$G_{p,\text{accum.}}^{1\to2}(\omega_\alpha) = \sum_j \int_0^{\omega_\alpha} g_{j,1}(\omega) d\omega_{j,1} \tag{2.7}$$

The spectral thermal conductance defined per unit ω, $g_{j,1}(\omega)$, can be converted to $g_{j,1}(\lambda)$ through change of variables as follows:

$$G_{p,\text{accum.}}^{1\to2}(\lambda_\alpha) = \sum_j \int_{\lambda_{\min}}^{\lambda_\alpha} -g_{j,1}(\omega) \frac{d\omega_{j,1}}{d\lambda_{j,1}} = \sum_j \int_{\lambda_{\min}}^{\lambda_\alpha} g_{j,1} d\lambda_{j,1} \quad , \tag{2.8}$$

where $\lambda_{\min}$ is the shortest phonon wavelength at the Brillouin zone edge where k is maximum. Based on the relationship between ω and k defined in the real dispersions and λ and k through

$k = \frac{2\pi}{\lambda}$, the term $\frac{d\omega}{d\lambda}$ can be analytically evaluated. The evaluated $g_{j,1}(\lambda)$ for each polarization branch in our metals is shown in Fig. 2.4. Most of the contributions come from relatively short λ in a range of 0.4 nm to 1 nm because the phonon density of states is highest for short λ, outweighing relatively lower $v_{j,1}(k_{j,1})$ in the short λ region. Discontinuous features in Fig. 2.4 occur because different ranges of frequency are spanned by each polarization branch in calculating $\zeta_{1\to2}$.

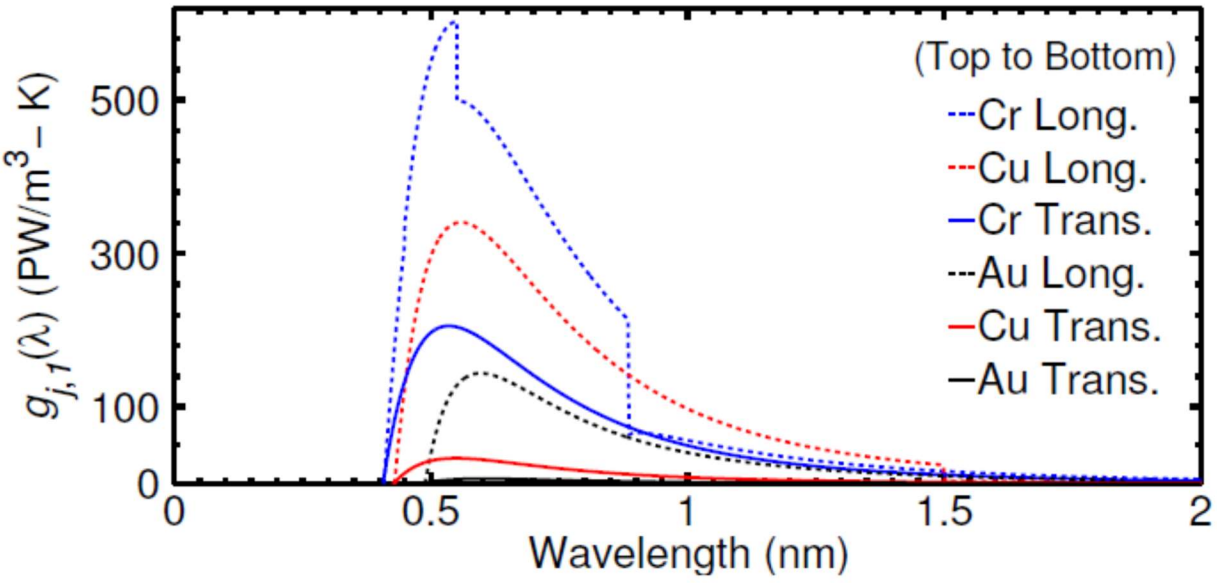

Fig. 2.4. The spectral thermal interface conductance as a function of wavelength, $g_{j,1}(\lambda)$, for each polarization branch in our metallic materials calculated using equation (6). Used and reprinted with permission from American Physical Society [36].

To account for the Au layer on top of Cu and Cr layers in G_p calculation, an additional assumption that phonons with λ greater than the adhesion layer thickness, t, directly come from

the Au layer is made. In this perspective, $G_p(t)$, the accumulated G_p as a function of the adhesion layer thickness, can be expressed as:

$$G_p(t) = G_{p,\text{accum.}}^{\text{AL}\rightarrow\text{Al}_2\text{O}_3}(t) + \left(G_{p,\text{Au}\rightarrow\text{Al}_2\text{O}_3} - G_{p,\text{accum.}}^{\text{Au}\rightarrow\text{Al}_2\text{O}_3}(t)\right) , \quad (2.9)$$

where $G_{p,\text{accum.}}^{\text{AL}\rightarrow\text{Al}_2\text{O}_3}(t)$ is the accumulated G_p as a function of adhesion layer thickness, and $G_{p,\text{Au}\rightarrow\text{Al}_2\text{O}_3}$ is the maximum value of $G_{p,\text{accum.}}^{\text{Au}\rightarrow\text{Al}_2\text{O}_3}(t)$.

The solid lines in Fig. 2.3-(b) show the calculated $G_p(t)$ using Equation (12) at 300 K. The predicted $G_p(t)$ started saturating once adhesion layer thicknesses becomes greater than 2 nm. The plateaued values are 180MW/m^2-K and 400MW/m^2-K for Cu and Cr respectively, which are in reasonable agreement with our experimentally saturated values. Therefore, the DMM is able to predict G with good confidence even for very thin adhesion layers. The enhanced bonding effect due to adhesion layers cannot be verified considering the uncertainties in our measurements are rather large. However, given that we are able to represent the experimentally obtained values closely with the DMM alone, a clear explanation on bonding effect is deemed unnecessary.

2.5 Interdiffusion effect on thermal interface conductance

A significant amount of enhancement is observed in thermal interface conductance across the metal Au – dielectric Al_2O_3 layer by simply inserting 1nm-thick Cu or Cr adhesion layer. However, even though a significant increase in thermal interface conductance is achieved by inserting an adhesion layer between a metal and dielectric Al_2O_3 interface, if the adhesion layer properties change due to interdiffusion between the adhesion layer and the metal, such increase cannot be sustained and could even reduce thermal conductance. Therefore, it is important to

understand how diffusion would evolve between the selected adhesion layer and the metal layer and how it affects *G*. In a separate study, we similarly deposited a Cu adhesion layer with varying thicknesses from 0 to 8 nm between the top 40-nm Au thin-film layer and the Al_2O_3 substrate. The sample is subjected to different degrees of interdiffusion by annealing it at temperatures ranging from room temperature (as deposited) to 520K for durations of 30 minutes. The change in the composition of Au and Cu as interdiffusion occurred is analyzed with X-ray photoelectron spectroscopy (XPS) using the reference sample which had an Au-Cu layer on a molybdenum (Mo) substrate. Fig.2.5-(a) and (b) show how the Au and Cu compositions changed in the 8-nm Cu / 40-nm Au sample as a function of the XPS measurement depth for different annealing temperatures. It is shown that up to 360K, no significant interdiffusion is observed for both atoms. However, after 440K, Cu atoms diffused into the Au layer rapidly and alloyed with Au with 8 at% Cu. At 520K, the Cu atoms completely intermixed with the Au layer. The faster diffusion of Cu into Au is expected because its diffusivity is much higher than that of Au into Cu [46].

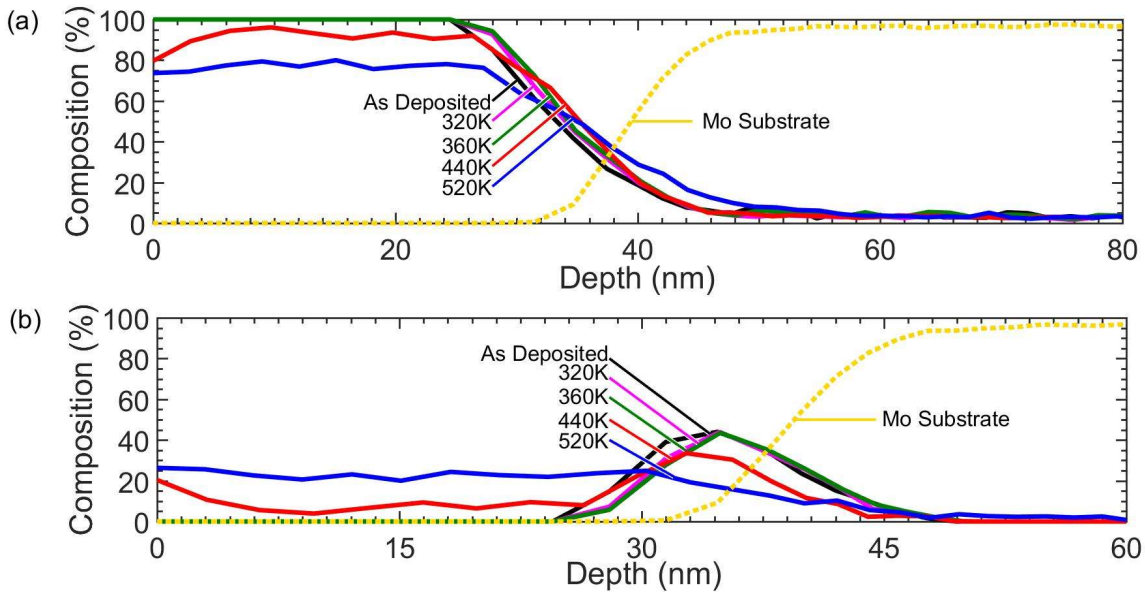

Fig.2.5. The X-ray photoelectron spectroscopy (XPS) compositional analysis for (a) gold (Au) and (b) copper (Cu) atoms in the 40-nm Au and 8-nm Cu layer sample deposited on molybdenum (Mo) substrate. Mo was chosen because both Cu and Au do not interdiffuse with Mo at an elevated temperature [47–49]. Different lines represent different 30-minute annealing temperatures. Work submitted to ACS AMI and used with permission from Dipanjan Saha.

The estimated diffusion length, <*r*>, that can be estimated by $\sqrt{\widetilde{D}t}$, where $\widetilde{D}$ is the interdiffusion coefficient and t is diffusion time. At 440K, when the compositions of both elements start to change appreciably, <*r*> is approximately 1.52 nm when using the reported value of $\widetilde{D}$ of 10^{-17} cm^2/sec for Cu diffusing through Au at 440K and t of 30 minutes. This is much shorter than the thickness of our Cu layer [51]. However, it was found that grain boundary diffusion which can enhance $\widetilde{D}$ by three or four orders of magnitude is significant at relatively low temperatures [52.53]. Given the high degree of interdiffusion we observed at the low annealing temperatures (440 K and 520 K), we can expect that the grain boundary diffusion or other diffusion mechanisms through surface or defects is active in our system [52].

The change in *G* as a function of annealing temperature and the Cu adhesion layer thickness is presented in Fig. 2.6. As explained and confirmed in the previous sections, *G* generally increased with an increasing Cu layer thickness. This data newly shows that *G* decreased with more enhanced interdiffusion associated with increasing annealing temperatures. As the interface loses Cu which has better 'matching' phonon dispersion properties with Al_2O_3 than Au as described in the previous sections, *G* would decrease with more Au atoms added at the interface. The experimental results of the as deposited and completely intermixed samples matched well with the values reported in Ref. [36] and Ref. [50], respectively.

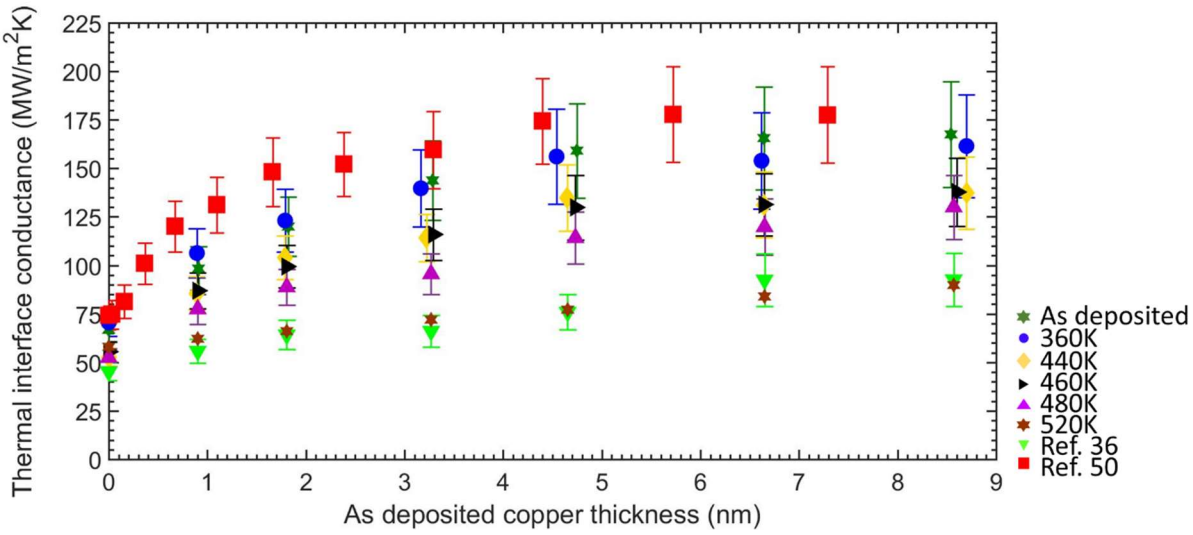

Fig.2.6. Thermal interface conductance as a function of the thickness of the deposited Cu layer between the Au and sapphire (Al_2O_3) layers for different annealing temperatures. The reference values are also shown. Work submitted to ACS AMI and used with permission from Dipanjan Saha.

2.6 Conclusions

We observed strong enhancement in *G* at the metal-dielectric Au/Al_2O_3 interface by inserting Cu and Cr adhesion layers. Both Cu and Cr show a saturation (390 ± 70 in Cr and 180 ± 20 in Cu) of *G* once the adhesion layer thickness reached 5 nm. This result shows that only a little amount of metals is needed to enhance *G* which can help to preserve materials' original properties and to save material costs. The DMM-based calculations match very well with the experimental data, suggesting that the phonon alignment at the interface is indeed a dominant mechanism in increasing *G*. The interdiffusion study confirms that *G* decreases as more

interdiffusion between Au and Cu occurs. It can be attributed to a loss of phonon alignment with Cu leaving the interface rapidly due to enhanced diffusivity at higher temperatures.

2.7 Supporting information

2.7.1

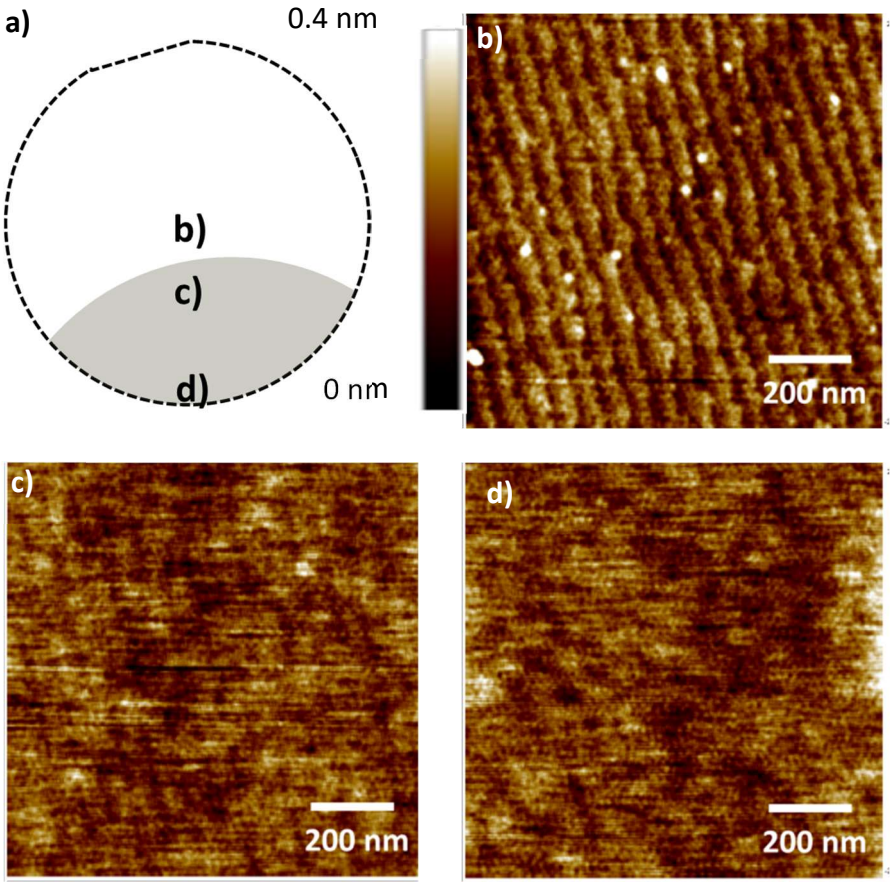

Fig. 2.S1. AFM scans of thin adhesion layers of Cr (no Au overlayer). a) Diagram showing the location of the scans, b) off-wedge, c) leading edge of wedge (< 1 nm thickness), and d) trailing edge of wedge (> 5 nm thickness). Used and reprinted with permission from American Physical Society [36].

2.7.2

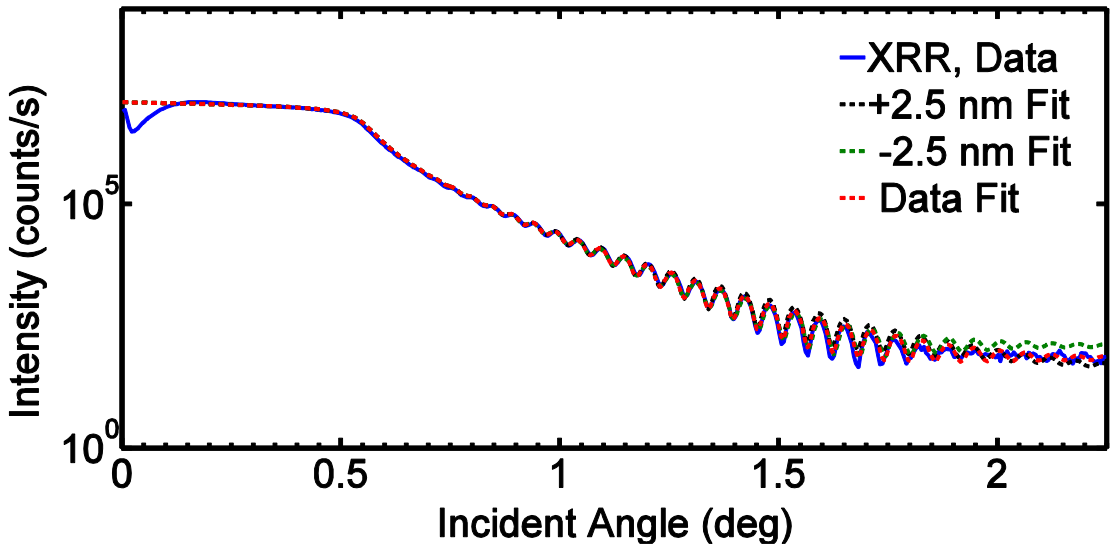

Fig. 2.S2. The XRR scan results of the Cu sample at the position 4.4cm away from the flat edge. By examining how much the fits deviate when the thickness is varied , the uncertainty in XRR-thickness can be determined. In our study, a ± 0.25nm change in the thickness causes an appreciable deviation from the original data fit curve beyond the incident angle of 1.5 degrees. Used and reprinted with permission from American Physical Society [36].

2.7.3

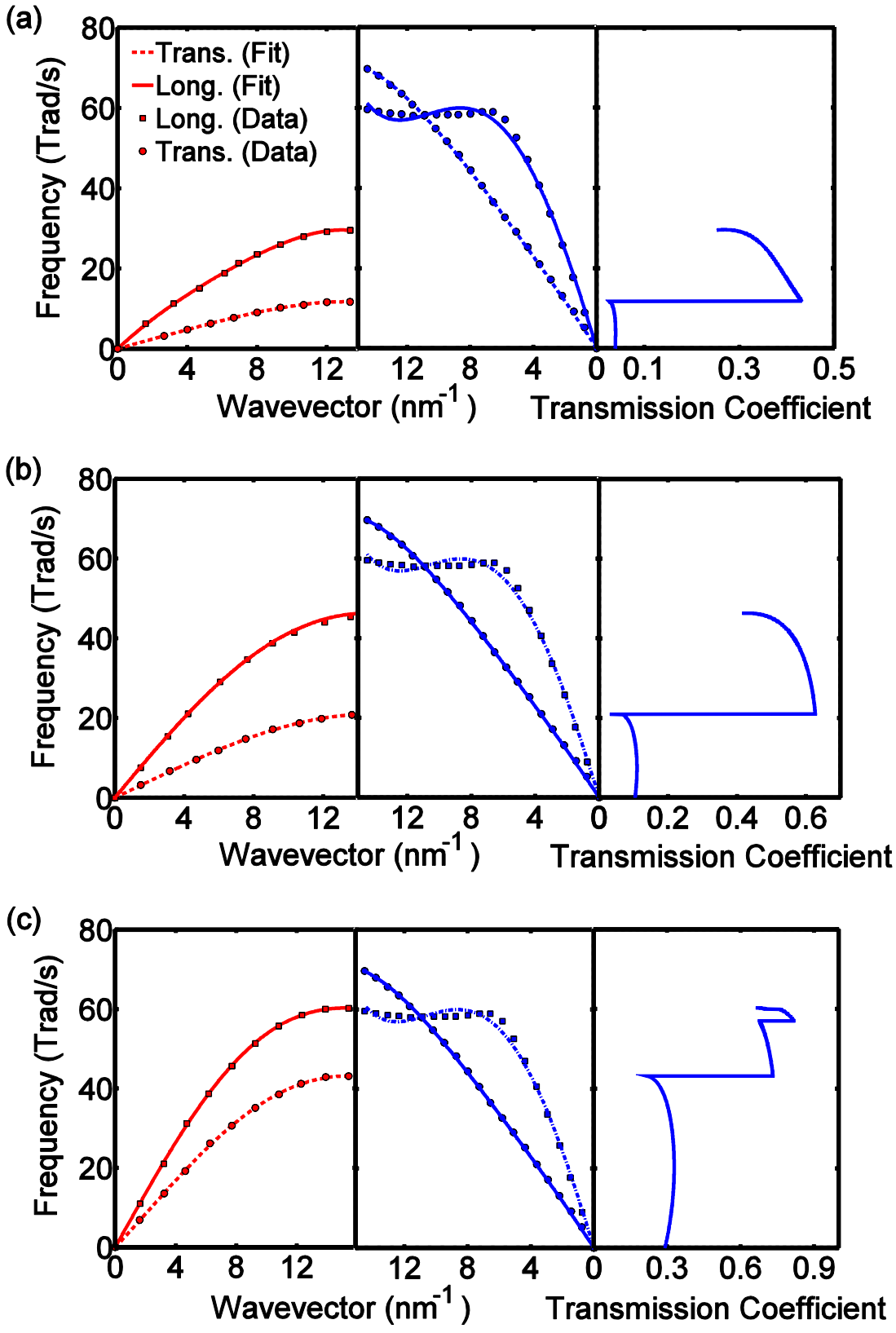
(a)
Trans. (Fit)
Long. (Fit)
Long. (Data)
Trans. (Data)
Frequency (Trad/s)
Wavevector (nm-1)
Transmission Coefficient
(b)
Frequency (Trad/s)
Wavevector (nm-1)
Transmission Coefficient
(c)
Frequency (Trad/s)
Wavevector (nm-1)
Transmission Coefficient

Fig. 2.S3. Both fitted and experimental dispersion relationships of (a) Au (b) Cu (c) Cr shown on the far-left with the Al_2O_3's dispersion relationship in the middle for comparisons. Solid line and rectangular markers represent the longitudinal branch, and dashed line and circular markers represent the transverse branch. The transmission coefficients of each metal for longitudinal and transverse polarization branches are presented on the far right hand side with respect to frequency, ω. *(Refs.* [37–40] *provided in the main text).* Used and reprinted with permission from American Physical Society [36].

[1] S. N. Piramanayagam and Tow C. Chong: *Developments in Data Storage: Materials Perspective*, John Wiley & Sons, n.d.

[2] Thomas Tsakalakos, Ilya A. Ovid'ko, and Asuri K. Vasudevan: *Nanostructures: Synthesis, Functional Properties and Applications*, Springer Science & Business Media, 2003.

[3] Venkatesha N, Veena Hegde, and Chandan Srivastava: *IET Nanobiotechnology*, 2014, vol. 8, pp. 184–89.

[4] G. Moulas, A. Lehnert, S. Rusponi, J. Zabloudil, C. Etz, S. Ouazi, M. Etzkorn, P. Bencok, P. Gambardella, P. Weinberger, and H. Brune: *Phys. Rev. B*, 2008, vol. 78, p. 214424.

[5] Dror Sarid and William Challener: *Modern Introduction to Surface Plasmons: Theory, Mathematica Modeling, and Applications*, Cambridge University Press, n.d.

[6] Shaomin Xiong, Jeongmin Kim, Yuan Wang, Xiang Zhang, and David Bogy: *J. Appl. Phys.*, 2014, vol. 115, p. 17B702.

[7] Alexander Q. Wu, Yukiko Kubota, Timothy Klemmer, Tim Rausch, Chubing Peng, Yingguo Peng, Darren Karns, Xiaobin Zhu, Yinfeng Ding, Eric K. C. Chang, Yongjun Zhao, Hua Zhou, Kaizhong Gao, Jan-Ulrich Thiele, Mike Seigler, Ganping Ju, and Edward Gage: *IEEE Trans. Magn.*, 2013, vol. 49, pp. 779–82.

[8] Dieter Weller, Gregory Parker, Oleksandr Mosendz, Andreas Lyberatos, Dmitriy Mitin, Nataliia Y. Safonova, and Manfred Albrecht: *J. Vac. Sci. Technol. B, Nanotechnol. Microelectron. Mater. Process. Meas. Phenom.*, 2016, vol. 34, p. 060801.

[9] W A Challener, Chubing Peng, A V Itagi, D Karns, Wei Peng, Yingguo Peng, XiaoMin Yang, Xiaobin Zhu, N J Gokemeijer, Y.-T. Hsia, G Ju, Robert E Rottmayer, Michael A Seigler, and E C Gage: *Nat. Photonics*, 2009, vol. 3, pp. 220–24.

[10] Zhi-Min Yuan, Jianzhong Shi, Chun Lian Ong, Pantelis Sophoclis Alexopoulos, Chunling Du, Anmin Kong, Shiming Ang, Budi Santoso, Siang Huei Leong, Kheong Sann Chan, Yibin Ng, Kui Cai, Jack Tsai, Hanxiang Ng, and Hang Khume Tan: *IEEE Trans. Magn.*, 2015, vol. 51, pp. 1–7.

[11] Liwen Huang, Barry Stipe, Matteo Staffaroni, Takuichi Hirano, Erhard Schreck, and F.Y. Huang: n.d., pp. 1–2.

[12] E T Swartz and R O Pohl: *Rev. Mod. Phys.*, 1989, vol. 61, pp. 605–68.

[13] Yibin Xu, Haitao Wang, Yoshihisa Tanaka, Masato Shimono, and Masayoshi Yamazaki: *Mater. Trans.*, 2007, vol. 48, pp. 148–50.

[14] R. J. Stoner and H. J. Maris: *Phys. Rev. B*, 1993, vol. 48, pp. 16373–87.

[15] Robert J. Stevens, Andrew N. Smith, and Pamela M. Norris: *J. Heat Transfer*, 2005, vol. 127, p. 315.

[16] J Lombard, F Detcheverry, and S Merabia: *J. Phys. Condens. Matter*, 2015, vol. 27, p. 015007.

[17] Yan Wang, Xiulin Ruan, and Ajit K. Roy: *Phys. Rev. B*, 2012, vol. 85, p. 205311.

[18] Arun Majumdar and Pramod Reddy: *Appl. Phys. Lett.*, 2004, vol. 84, p. 4768.

[19] Patrick E. Hopkins, John C. Duda, Bryan Kaehr, Xiao Wang Zhou, C.-Y. Peter Yang, and Reese E. Jones: *Appl. Phys. Lett.*, 2013, vol. 103, p. 211910.

[20] Piyush Singh, Myunghoon Seong, and Sanjiv Sinha: *Appl. Phys. Lett.*, 2013, vol. 102, p. 181906.

[21] R. B. Wilson, Joseph P. Feser, Gregory T. Hohensee, and David G. Cahill: *Phys. Rev. B*, 2013, vol. 88, p. 144305.

[22] Edward Dechaumphai, Dylan Lu, Jimmy J. Kan, Jaeyun Moon, Eric E. Fullerton, Zhaowei Liu, and Renkun Chen: *Nano Lett.*, 2014, vol. 14, pp. 2448–55.

[23] R. E. Jones, J. C. Duda, X. W. Zhou, C. J. Kimmer, and P. E. Hopkins: *Appl. Phys. Lett.*, 2013, vol. 102, p. 183119.

[24] A. V. Sergeev: *Phys. Rev. B*, 1998, vol. 58, pp. R10199–202.

[25] John C Duda, Thomas E Beechem, Justin L Smoyer, Pamela M Norris, and Patrick E Hopkins: *J. Appl. Phys.*, 2010, vol. 108, p. 73515.

[26] J. D. N. Cheeke, H. Ettinger, and B. Hebral: *Can. J. Phys.*, 1976, vol. 54, pp. 1749–71.

[27] Pamela M. Norris and Patrick E. Hopkins: *J. Heat Transfer*, 2009, vol. 131, p. 043207.

[28] C Kittel: *Introduction to Solid State Physics*, 2005.

[29] Timothy S. English, John C. Duda, Justin L. Smoyer, Donald A. Jordan, Pamela M. Norris, and Leonid V. Zhigilei: *Phys. Rev. B*, 2012, vol. 85, p. 035438.

[30] J. C. Duda, C.-Y. P. Yang, B. M. Foley, R. Cheaito, D. L. Medlin, R. E. Jones, and P. E. Hopkins: *Appl. Phys. Lett.*, 2013, vol. 102, p. 081902.

[31] Wee-Liat Ong, Sara M. Rupich, Dmitri V. Talapin, Alan J. H. McGaughey, and Jonathan A. Malen: *Nat. Mater.*, 2013, vol. 12, pp. 410–15.

[32] Jonathan A. Malen, Kanhayalal Baheti, Tao Tong, Yang Zhao, Janice A. Hudgings, and Arun Majumdar: *J. Heat Transfer*, 2011, vol. 133, p. 081601.

[33] Aaron J Schmidt, Xiaoyuan Chen, and Gang Chen: *Rev. Sci. Instrum.*, 2008, vol. 79, p. 114902.

[34] Keith T Regner, Daniel P Sellan, Zonghui Su, Cristina H Amon, Alan J H McGaughey, and Jonathan A Malen: *Nat. Commun.*, 2013, vol. 4, p. 1640.

[35] David G. Cahill: *Rev. Sci. Instrum.*, 2004, vol. 75, pp. 5119–22.

[36] Minyoung Jeong, Justin P. Freedman, Hongliang Joe Liang, Cheng-Ming Chow, Vincent M. Sokalski, James A. Bain, and Jonathan A. Malen: *Phys. Rev. Appl.*, 2016, vol. 5, p. 014009.

[37] H. Schober, D. Strauch, and B. Dorner: *Zeitschrift For Phys. B Condens. Matter*, 1993, vol. 92, pp. 273–83.

[38] Ruqing Xu, Hawoong Hong, Paul Zschack, and T.-C. Chiang: *Phys. Rev. Lett.*, 2008, vol. 101, p. 085504.

[39] J. W. Lynn, H. G. Smith, and R. M. Nicklow: *Phys. Rev. B*, 1973, vol. 8, pp. 3493–99.

[40] W. M. Shaw and L. D. Muhlestein: *Phys. Rev. B*, 1971, vol. 4, pp. 969–73.

[41] Takeo Sasaki, Katsuyuki Matsunaga, Hiromichi Ohta, Hideo Hosono, Takahisa Yamamoto, and Yuichi Ikuhara: *Sci. Technol. Adv. Mater.*, 2003, vol. 4, pp. 575–84.

[42] Z. Boekelheide and F. Hellman: *Appl. Phys. Lett.*, 2013, vol. 102, p. 141601.

[43] S. Tsukimoto, F. Phillipp, and T. Wagner: *J. Eur. Ceram. Soc.*, 2003, vol. 23, pp. 2947–54.

[44] Christine Marie Montesa, Naoya Shibata, Tetsuya Tohei, Kazuhiro Akiyama, Yoshirou Kuromitsu, and Yuichi Ikuhara: *Mater. Sci. Eng. B*, 2010, vol. 173, pp. 234–38.

[45] Ramez Cheaito, John T. Gaskins, Matthew E. Caplan, Brian F. Donovan, Brian M. Foley, Ashutosh Giri, John C. Duda, Chester J. Szwejkowski, Costel Constantin, Harlan J. Brown-Shaklee, Jon F. Ihlefeld, and Patrick E. Hopkins: *Phys. Rev. B*, 2015, vol. 91, p. 035432.

[46] H G Tompkins and M R Pinnel: *J. Appl. Phys. J. Appl. Phys. Copp. J. Appl. Phys. Copper-Silver Copper-Gold Syst. J. Phys. Chem. Ref. Data*, 1976, vol. 47.

[47] J.-W. He, D.Wayne Goodman, D.G. Naugle, and D.L. Cocke: *Mater. Lett.*, 1990, vol. 10, pp. 250–55.

[48] Matthew A. Payne, James B. Miller, and Andrew J. Gellman: *Corros. Sci.*, 2015, vol. 91, pp. 46–57.

[49] Deepika Priyadarshini, Petro Kondratyuk, Yoosuf N. Picard, Bryan D. Morreale, Andrew J. Gellman, and James B. Miller: *J. Phys. Chem. C*, 2011, vol. 115, pp. 10155–63.

[50] Justin P Freedman, Xiaoxiao Yu, Robert F Davis, Andrew J Gellman, and Jonathan A Malen: *Phys. Rev. B*, 2016, vol. 93.

[51] H G Tompkins and M R Pinnel: *J. Appl. Phys. J. Appl. Phys. Copp. J. Appl. Phys. Copper-Silver Copper-Gold Syst. J. Phys. Chem. Ref. Data*, 1976, vol. 47.

[52] J W Elmer, T A Palmer, and E D Specht: 2005.

[53] A. E. Austin and N. A. Richard: *J. Appl. Phys.*, 1962, vol. 33, pp. 3569–74.

Probing thermal transport across a thin nanostructured gap via FDTR

3.1 Abstract

In this chapter, we present a mechanical bonding approach to construct thermomechanically stable nanosized gaps for measurements of the near-field thermal radiative effect. We successfully fabricated the 10 nm and 50 nm gap samples sandwiched between the parallel silicon dioxide (SiO_2) layers or between gold (Au) and SiO_2 layers by pressing a patterned pillar structure onto an SiO_2 slide. The heat transfer coefficients across the gap (h_{ga}) in air and in vacuum for both cases are measured via optical frequency-domain thermoreflectance (FDTR) technique. Here, we observed distinct differences in experimentally obtained phase lags when FDTR is placed over the pillars that support the gap structure and when it is instead placed over the gap regions, which indicates that the gaps with intended thicknesses did not collapse. The experimentally obtained h_{gap} in each case are also reasonably close to the expected values under conditions where the gap was evacuated and infiltrated with air or helium. Large uncertainties in the obtained values using the conventional analysis necessitated a novel differential analysis to interpret the obtained phase lags; the differential analysis indeed enabled us to be more sensitive to h_{gap}.

3.2 Introduction

Thermal radiative transport between thermal source and surroundings occurs through exchange of heat energy via electromagnetic waves. In thermal radiation the electromagnetic

waves in both propagating and evanescent modes can contribute. The propagating modes can radiate freely from a thermal source into the surrounding space while the evanescent modes are confined to the surface with characteristic decay lengths (d) that represent how far the evanescent modes will extend vertically out from the surface to the surroundings. [1–3] These evanescent modes are generated through total internal reflection of electromagnetic waves and surface polaritons. [1] The propagating modes follow Planck's theory, which states that the radiative thermal transport cannot exceed black body radiation, - i.e., $\phi(T_1^4 - T_2^4)$, where ϕ is Stefan-Boltzmann constant (5.67×10^{-8} W/m^{2}K^4), and T_1 and T_2 represent the temperatures of object 1 and object 2. This holds true when the thermal source and the surrounding are separated such that evanescent modes do not overlap. However, as we keep decreasing the separation distance between the thermal source and the emitter, approaching the value of d that is in nanometers, the evanescent modes start contributing to radiative heat flux. This enhancement of radiative heat flux due to a very narrow gap is called near-field thermal radiation. Both experimentally and theoretically, the radiative heat transfer enhancement in orders of magnitude has been confirmed. Hu et al. experimentally confirmed that when the distance between two SiO2 plates decreased from 2 mm to 1.6 μm, the radiative heat flux increased by approximately twice [3]. Park et al. computed that the heat flux through a vacuum gap between the two silicon carbide (SiC) plates will increase by 100 times when the vacuum gap distance decreases from 100 nm to 10 nm [4]. Song et al. also observed through both experiments and simulations that the thermal conductance due to the near-field radiative effect could enhance by three times at maximum when the size of the gap between the parallel SiO_2 plates decreases from 100 nm to 20 nm [5].

Near-field thermal radiation has been actively studied for useful applications including thermophotovoltaics, thermal circuits, thermal imaging and heat-assisted magnetic recording (HAMR) technology. [6,7] In this study, HAMR is of specific interest. In HAMR, a near-field transducer (NFT) that is typically composed of gold focuses energy beyond the diffraction limit onto the media bygeneration of surface plasmon polaritons (SPPs) [7]. As shown in Chapter 1, a sharp tip of the NFT and a short distance between the NFT and the recording media that is typically in a couple of tens of nanometers creates very strong local heating. The recording media heated near or above its curie temperature will turn paramagnetic which requires a significantly less strong magnetic field for writing than its ferromagnetic room temperature state [8]. This enables the use of magnetically coercive materials for the media, which is beneficial to overcome a superparamagnetic effect that becomes evident when decreasing the grain sizes of less coercive magnetic media down to a few tens of nanometers for increased storage density [9].

While the short distance between the NFT head and the media is desirable to maximize local heating of the media as desired, it may help the heated media radiate heat back to the head. This "back-heating" of the NFT head from the heated media through a thin head-media air gap may contribute to thermal breakdown of the NFT. Therefore, understanding the extent of back-heating near-field radiative heat transport through a nano-sized gap is important. More specifically, the temperature dependent near-field thermal radiative behavior needs to be understood given that the actual HAMR device will operate at a temperature range of approximately 800-1000K. [10] This will be scientifically interesting as well because experimental measurements of near-field thermal radiation as a function of temperature up to sufficiently elevated temperatures have not been conducted. This lack of temperature-dependent study could be attributed to hardship associated with bulkiness of measurement apparatuses. For

example, Kim et al. observed significant enhancement in thermal conductance (× 2,000 at maximum) across the gaps sandwiched between various materials including silicon dioxide (SiO_2), Au and silicon nitride (SiN) as the gap sizes decrease as small as ~1 nm via scanning thermal probes [11]. While this technique enables measurements across an extremely small 1 nm gap, heating or cooling the whole probing system by placing it inside a temperature-controlling chamber or furnace would be challenging. In this perspective, our laser-based frequency-domain thermoreflectance technique is promising because it enables temperature-dependent thermal property measurements by shooting lasers on a sample of interest placed inside a cryostat that can be both pressure and temperature-controlled.

Therefore, our objective in this study is first to fabricate nanostructured gap samples that mimic the actual HAMR NFT geometry and that enable measurements of the near-field radiative effect. The most challenging issue is to fabricate thermomechanically stable gaps that the nanometer gaps will not collapse due to temperature or pressure change. In addition, accurately measuring thermal transport properties across a thin gap is another issue. These two issues are very critical as further measurements would not be meaningful if we cannot confirm the robustness of our gap structure and our ability to successfully measure thermal properties of the nanostructured gap. Thus, while the ultimate goal is accurately measuring the temperature-dependent near-field radiative behavior, we focused heavily on designs and fabrications of such gap structures along with the gap thermal property measurement analysis. Moreover, even if we are not able to single out the near-field radiative effect, an attempt to measure thermal properties of the gap filled with different gases via an optical technique has not been performed in prior studies. As already explained in Chapter 1, because the near-field radiative effect is maximized when we have identical materials across a thin gap [5,12–14] due to the matching resonances in

evanescent modes, we chose to assemble a SiO_2-SiO_2 bonded structure with a nano-sized gap in between. We also chose to assemble a 'non-matching' structure as a contrasting example where the gap exists between a gold (Au) and SiO_2 layers.

3.3 Sample structure designs

One of the important aspects that needed to be considered for the successful FDTR measurements is to create a sufficiently thin gap structure that is mechanically stable and thermally sensitive so that we can accurately measure the gap's heat transfer coefficient. For the mechanical stability, we relied on fixed-fixed beam deflection analysis to decide what thicknesses (t) and widths of the top structure (L) that define the span of the cavity, as shown in Fig.3.1–(a), should be targeted to prevent the gap from collapsing. The details of the deflection analysis are given in the Supporting Information with the analysis results shown in Fig. 3.1-(b).

(a)

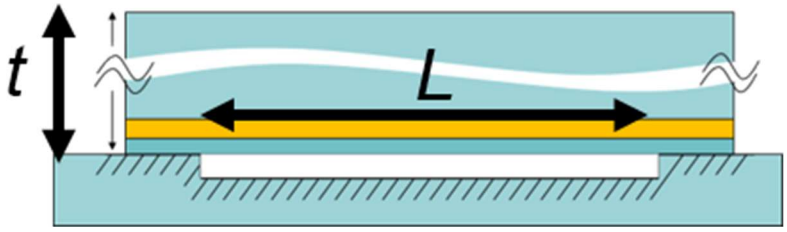

(b)

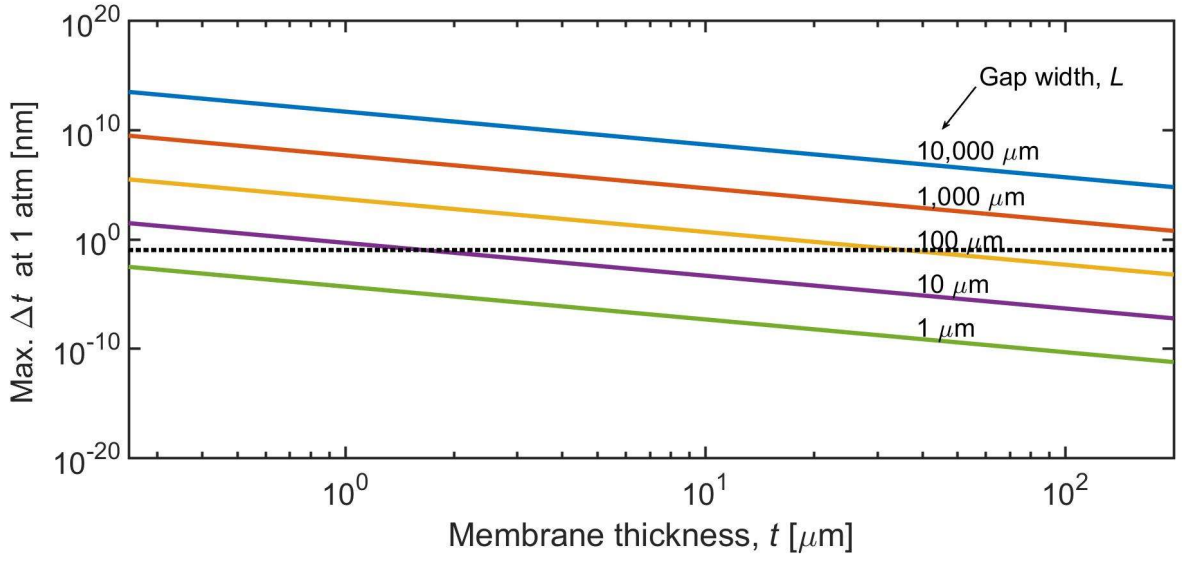

Fig.3.1. (a) A schematic of the assembled SiO_2-SiO_2 gap structure where the top membrane with a thickness t is attached to the bottom structure with the supporting pillars that are separated by a width of L (b) The maximum deflection of the top SiO_2 layer (Δt) as a function of different t values for different sizes of L when the whole assembly is subjected under 1 atm pressure. A pressure of 1 atm is chosen because the gap will be subjected to a cycle of evacuation and venting to the ambient pressure. The dashed line shows the chosen Δt_{max} critical value of 1 Å, which is chosen for being a fraction of the smallest gap size of 1 nm.

According to this analysis, as L increases, the maximum deflection of the top structure (Δt_{max}) increases while increasing t will decrease Δt when the assembly is subjected to a 1 atmosphere of pressure from the top. We set a sufficiently small value of Δt_{max} at 1 Å as a critical value below which the gap will not collapse. It is chosen as a fraction of the smallest

possible gap size of 1 nm and is represented as a dashed line in Fig. 3.1-(b). This means that Δt_{max} value on the y-axis should be below the dashed line to meet the criterion. The bowing of the top membrane should be considered because they cannot be perfectly flat. However, the bowing that exists in the regions where the distance between the support pillars, L, is sufficiently large will be removed by applying sufficient pressure as seen by very large Δt in Fig.3.1. For example, when the bowing exists over 10 mm of L, the corresponding Δt is approximately 10 meters when t is 10 μm and subjected under 1 atmospheric pressure. On the other hand, the gaps that exist in the narrowly spaced pillar regions will not collapse; when L is much smaller at 100 μm, Δt will only deflect about 1 nm for the 10 μm-thick top membrane under 1 atmospheric pressure.

Based on our separate FDTR sensitivity analysis, it is beneficial for us to have a thinner membrane to be more sensitive to the change in thermal conductance across the gap.

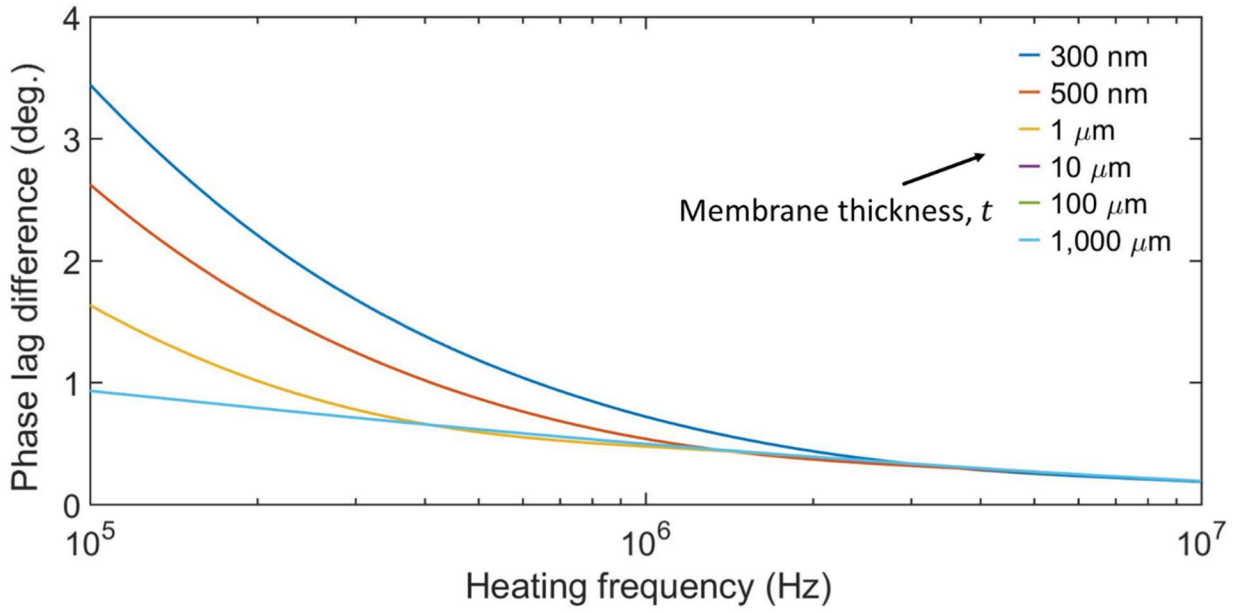

Fig.3.2. The calculated phase lag difference when the thermal conductance across the gap changes from 24 KW/m^{2}K to 120 KW/m^{2}K as a function of heating frequency for different t values. The 10 μm, 100 μm and 1,000 μm curves are identical to one another.

The analysis of how the calculated phase lag values would change when the thermal conductance across the gap assembled between two parallel quartz layers changes from 24 KW/m^{2}K to 120 KW/m^{2}K is shown in Fig.3.2 for various t; 24 KW/m^{2}K is chosen as it was a reported computation value when the 10 nm gap between two parallel SiO_2 plates is under vacuum and show the near-field effect [5]. This value changed to 120 KW/m^{2}K when the gap is exposed to the ambient air environment [100]. It is apparent that as t increases, the calculated phase lag change decreases. However, with decreasing t, L also should decrease as well to minimize Δt_{max}. Specifically, for our chosen critical value of 1 Å, L should be approximately 10 μm when the top membrane's t is about 2 μm.

To fully maximize our sensitivity to the thermal properties of the gap, we need to consider lateral heat spreading. Later heat spreading occurs when the heat absorbed from the laser spreads radially and interacts with the supporting pillars, creating a thermal short that obscures parallel radiative pathways. This is problematic because we will lose our sensitivity to solely measure the gap's thermal properties. To analyze how far the heat would spread radially for given *t,* we relied on an annular fin analysis. The results of annular fin analysis are shown in Fig. 3.3 with the detailed descriptions about the analysis in Supporting Information. According to this analysis, *L* cannot be smaller than approximately 40 μm. Thus, we used commercially available SiO_2 slides as received with their thicknesses of approximately 1,000 μm.

Accordingly, the supporting pillars should be separated at least 40 μm apart to ensure minimal heat spreading, but not more than 200 μm for better mechanical stability. Thus, we decide to use commercially available SiO_2 slides as received with their thicknesses of approximately 1,000 μm, despite we lose our thermal sensitivity with a thicker membrane.

3.4 Sample fabrications

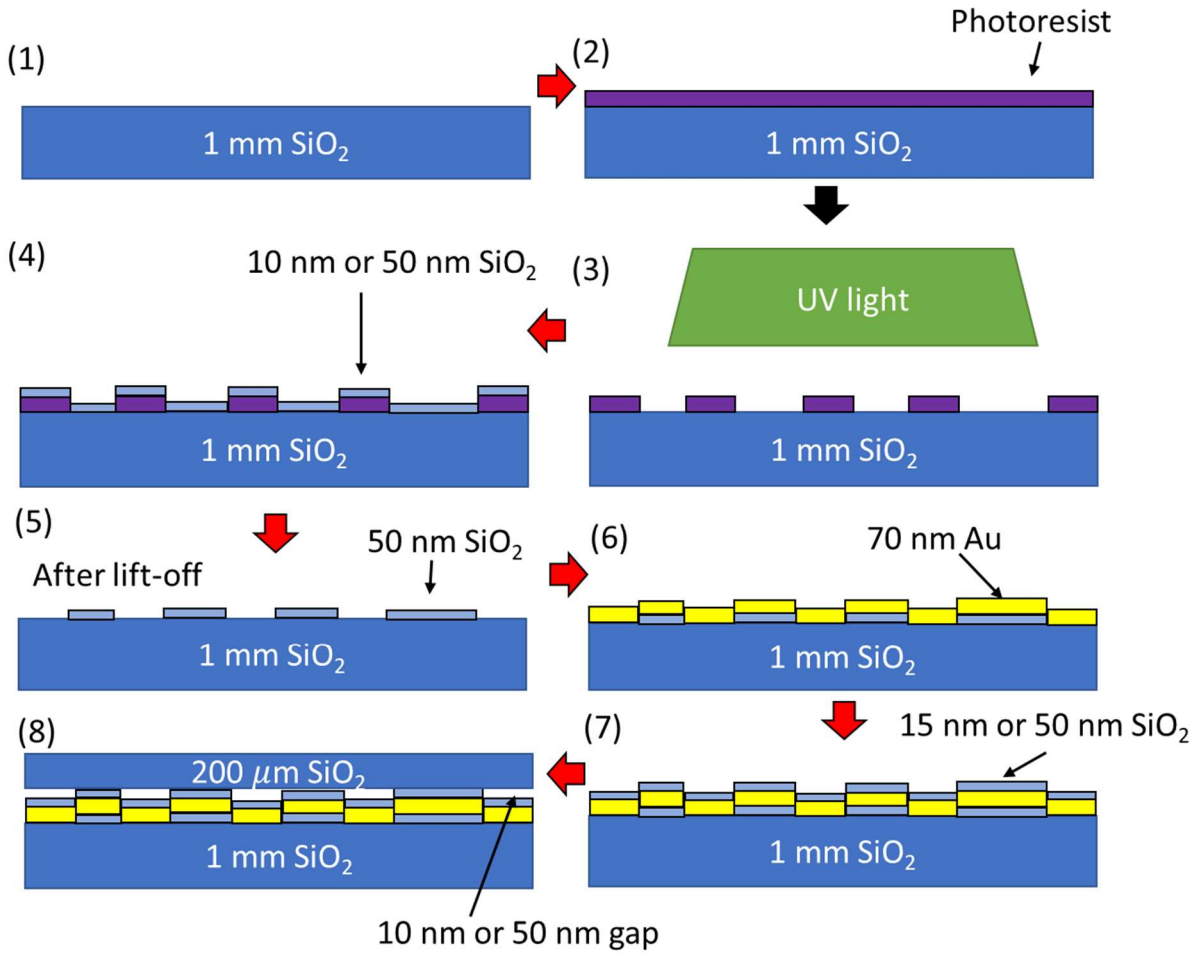

Fig. 3.4. The layer by layer schematics for the 50 nm SiO_2-SiO_2 gap sample fabrication process. The 10 nm SiO_2-SiO_2 gap sample requires 10 nm SiO_2 deposition at step (4) and step (7). The Au-SiO_2 gap sample does not require step (7).

For the top membrane, a 200 μm thick round-shaped (18 mm in diameter) GE 124 quartz coverslip is purchased from SPI Supplies. For the bottom substrate, a 1-mm thick square-shaped (10 mm in length) GE 124 slide is purchased from SPI Supplies. To fabricate supporting pillars

on the bottom substrate, a photoresist pattern is created by first spin-coating hexamethyldisilazane (HMDS) at 3000 RPM for 30 seconds followed by 1-minute baking at 95 ℃. After baking, the AZ 4110 positive photoresist is spin-coated at 3000 RPM for 40 seconds on top of the baked sample. The photoresist covered slide is then patterned using a Karl Suss MA6 mask aligner with a designed chromium (Cr) mask. The mask is designed to block certain regions from the incoming flux of ultraviolet (UV) light. With the positive photoresist, the UV-exposed regions are removed after development in AZ 400K developer. In our case, we exposed those regions where we wanted to create gaps. The detailed mask layout is included in Supporting Information. Using this mask, a range of different lengths of gap span, L, from 15 μm to 60 μm with a 5 μm increment are created. The sizes of the supporting pillars changed accordingly as the value of L changed to ensure the same areal fraction of pillars across the whole structure (15 μm to 90 μm with a 5 μm increment). Because air needs to leave the assembly successfully for radiation measurements, the gap regions are not surrounded by the pillars as shown in the mask layout. The developed sample is then transferred to a sputtering chamber for the initial 50 nm SiO_2 deposition. This initial SiO_2 layer thickness will define the gap thickness, L_g. Thus, the 10 nm gap sample can be fabricated by depositing 10 nm SiO2 first. After this deposition, the sample went through a lift-off process in acetone, isopropyl alcohol and distilled water for 5 minutes each to create 50 nm SiO_2 pillars on the bottom substrate. The SiO_2 patterned sample is then transferred to the sputtering chamber again where the 70 nm Au and 50 nm SiO_2 layers are deposited in order. For the 10-nm Au-SiO_2 gap sample, only 70 nm Au is deposited on top. The overall layer formation process is shown in Fig. 3.4. The thickness of each layer is confirmed with XRR (X-ray reflectivity) with the analysis results included in Supporting Information. Finally, the 1mm-thick quartz slide is placed on top of the patterned structure,

which created a 50 nm gap sample. The assembled structure is then held tight together by being placed in a specially designed holder. Both assembly and holder insertion processes are done in a class 10 clean-room environment to avoid contamination. The holder has a hex-screw that applied pressure to the 200 μm SiO_2 coverslip, thus pushing onto the bottom structure for the measurements. Fig.3.5-(a) and (b) show an optical microscope image of the fabricated 50-nm Au – SiO_2 structure and a camera picture of the sample assembled inside a holder. Fig.3.5-(c) illustrates how our measurements are performed with the lasers.

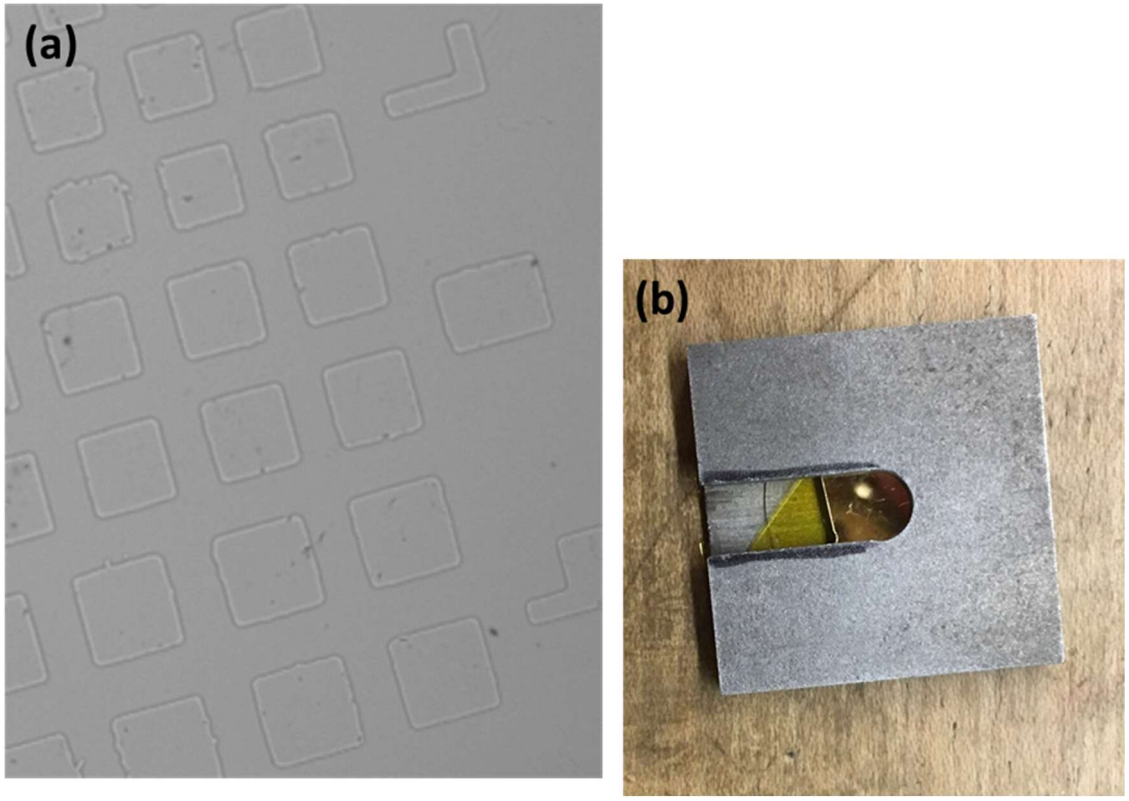

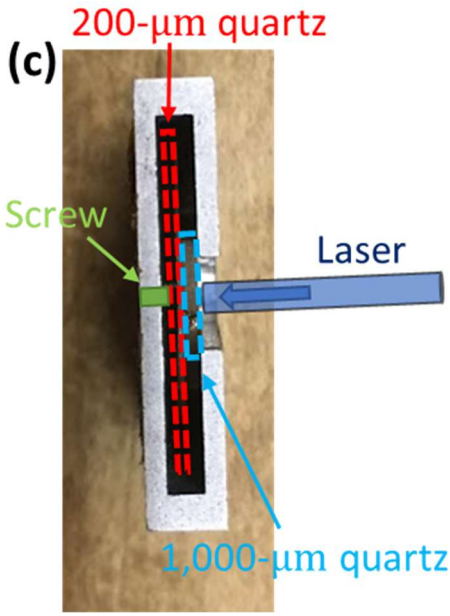

Fig.3.5. (a) A 5X optical microscope image of the 50-nm gap patterned structure (b) a holder pressing the top and bottom structure together for measurements (c) illustration of sample and laser configurations for measurements

3.5 Computations of h_{gap}

To estimate heat transfer coefficient across the gap (h_{gap}) for different conditions in the non-near-field and near-field cases, the conductive and radiative contributions to gas heat transfer coefficient (h_{gas}) as a function of pressure are used. The convective contribution is not considered; it is negligibly small because the Rayleigh number, which scales as t^3 is negligibly small for nanoscale gaps [15]. The conductive contribution to h_{gas}, h_{cond}, as a function of pressure is calculated based on the following equation established by Ref. [16,17] :

$$h_{cond} = \left(\frac{\kappa^*_{gas}}{1+\frac{\frac{2-a}{\sqrt{2a}}\left(\frac{9\gamma-5}{\gamma+1}\right)\frac{k_b T}{\pi\xi^2 P}}{L_g}} \right) * \frac{1}{L_g} \tag{3.1}$$

where κ^*_{gas} is the thermal conductivity of gas at standard temperature and pressure (STP) condition, a is the thermal accommodation coefficient, γ is the specific heat ratio of the gas, k_b is the Boltzmann constant, T is the temperature of air, ξ is the gas molecule's effective collision diameter, P is the pressure of air, and L_g is the thickness of the gap that contains air gas molecules. Because air is mostly composed of nitrogen (N_2), each of the material-specific values used N_2's properties as shown in the following Table 3.1 [15,16,18,19]. The results with the varying P from 10^{-4} Torr to 10^7 Torr and L_g (10 nm, 50 nm and 3.6 μm) are shown in Fig.3.6. T is set at 300K. Based on Fig. 3.6, the h_{cond} when it is in the ambient condition (760 Torr) for each different L_g are 6.53 X 10^3 W/m^{2}K, 7.22 X 10^4 W/m^{2}K, and 8.13 X 10^4 W/m^{2}K for the 3.6 μm, 50 nm and 10 nm cases respectively.

Table 3.1. Air-specific values used to calculate h_{cond} [15,16,18,19]

Parameters	Values
κ^*_{gas}	0.026 W/m·K
a	0.800
γ	1.400
ξ	375 pm

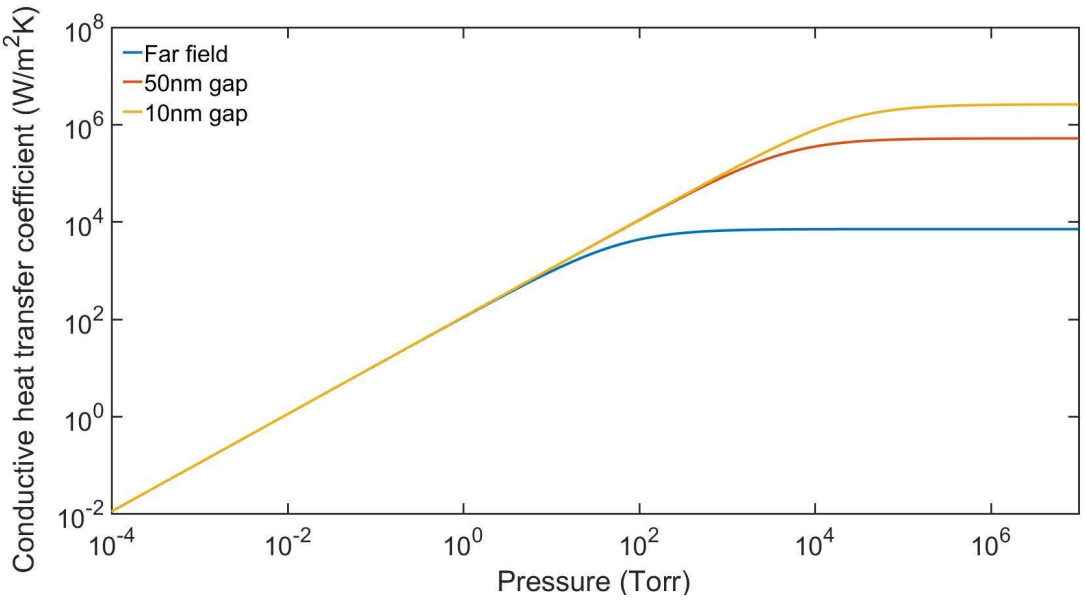

Fig.3.6. Heat transfer coefficient across the air gap due to conduction, h_{cond} as a function of pressure for different air gap thicknesses, L_g. The far-field assumed L_g of 3.6 μm and labeled "Far field".

The radiative contribution, h_{rad}, for different L_g in different cases is extracted from the reported values given in Ref. [5] and represented below in Table 3.2. These values of h_{rad} are then added to the previous h_{cond} for each case of L_g across the whole frequency range to obtain "total" thermal conductance of air, $h_{total}(= h_{cond} + h_{rad})$. The result is shown in Table 3.2 and illustrated in Fig.3.7.

Table 3.2. The effect of gap thicknesses, L_g on h_{rad} h_{cond} and h_{to} $(h_{rad} + h_{cond})$

Cases	**Gap thickness (L_g)**	**h_{rad} [5] (W/m^{2}K)**	**h_{cond} at 1 atm (W/m^{2}K)**	**h_{total} at 1 atm (W/m^{2}K)**
SiO_2-SiO_2	10 nm	2.60 X 10^4	8.13 X 10^5	1.07 X 10^5
	50 nm	1,000	7.22 X 10^4	7.32 X 10^4

	3.6 μm	10	6.53 X 10^3	7.01 X 10^3
Au-SiO_2	10 nm	10	8.12 X 10^4	8.12 X 10^4
	50 nm	1	7.22 X 10^4	7.22 X 10^4
	3.6 μm	1.00 X 10^{-4}	6.53 X 10^3	6.53 X 10^3

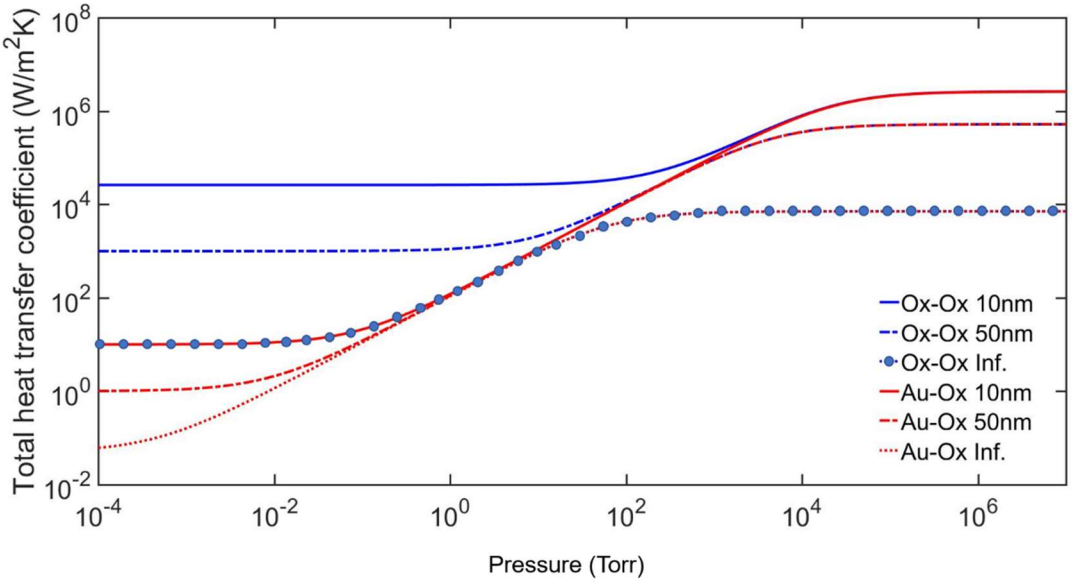

Fig.3.7. The total heat transfer coefficient of air, h_{total} as a function of pressure between 10^{-4} and 10^7 Torr. 'Ox-Ox' in the label represents the SiO_2-SiO_2 gap system and 'Au-Ox' represents the Au-SiO_2 gap system.

In this study, our objective is to attempt to measure h_{gap} for different conditions specified in Table 3.2 and compare it to the expected h_{total}. We excluded the far field measurements and focused on the nanostructured gaps of 10 nm and 50 nm. For the 50 nm gap, we performed the vacuum measurements only in the SiO_2-SiO_2 paired case as measuring h_{gap} of a very small value (1 W/m^{2}K) would be very challenging with the current measurement setup

and sample geometry. The ambient measurements for the 50 nm gap sample are performed only in the Au-SiO_2 case as its h_{total} is almost the same as that in the 50 nm SiO_2-SiO_2 case.

3.6 Experimental measurements of h_{gap}

The change in h_{gap} for different conditions is experimentally measured using a non-contact optical technique called frequency-domain thermoreflectance (FDTR). The detailed information about FDTR is provided in Chapter 1.6. In FDTR, a sample surface will be heated up with a laser beam called a pump laser. The pump laser beam is an initially continuous wave laser beam and is intensity modulated by an electro-optic modulator at different frequencies. Another laser beam called a probe laser will be co-aligned with the incoming pump beam and measure the change in temperature induced by periodic pump beam heating at the sample surface. The thermal response of the sample is affected by sample thermal property and is denoted in the phase-lag between the incoming pump and reflected probe lasers. After obtaining the experimental phase-lag values as a function of pump modulation frequencies, they are fitted to analytically calculated values using the three-dimensional heat diffusion equation until the best-fit is achieved where the only fitting parameter is the desired sample thermal property. The biggest advantage of using FDTR is that the lasers can pass through a viewport of a cryogenic device, cryostat, that can be temperature controlled and evacuated to create a radiation-only vacuum environment.

To experimentally quantify that the near-field radiative heat transfer, an increase in h_{gap} when only radiation is present should be measured for the SiO_2-SiO_2 relative to the SiO_2-Au gap. Good contact between the top membrane and bottom patterned structure is essential to guarantee the gap size and measure the near-field effect accurately. Contact can be confirmed by observing

distinctively different phase lag behavior between the pillar and gap regions. The experimentally obtained phase lags on the pillar and the gap region of the 50 nm Au-SiO_2 gap sample in the ambient and high vacuum (5×10^{-5} Torr) environments are shown in Fig.3.8-(b) with their analytically predicted fits to h_{gap}. If the structure is in poor contact due to a dust particle or uneven surfaces, there would be an unintended gap across the structure even on the supporting pillars, which would result in undistinguishable phase lag behaviors between pillars and the gap regions. For the fitting processes, G between the Au and SiO_2 layers is left unknown as a fitting parameter for the pillar region. For the gap region, h_{gap} is set as a fitting parameter. The known material parameters used for the fitting process for each case are described in more detail in Supporting Information. The obtained fits between the experimentally acquired and theoretically calculated phase lag values are sufficiently high with mean squared error (MSE) values of approximately 0.03 on average for all sets of data.

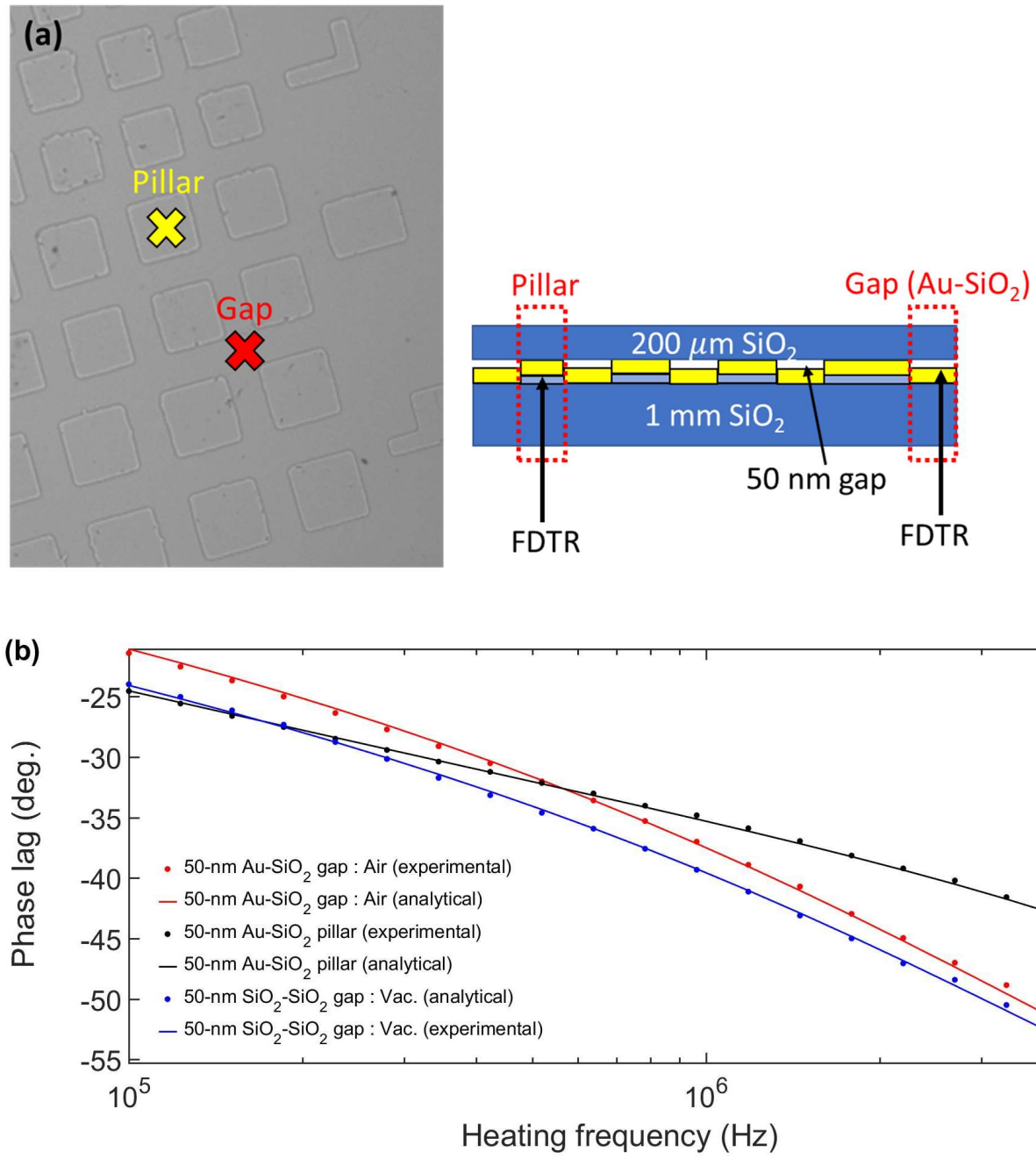

Fig.3.8. (a) A schematic of where the measurements are performed for the gap and pillar region data in an actual sample. (b) The experimentally obtained phase lag values along with their fits to the analytically calculated values in the pillar and gap regions (ambient) of the 50-nm Au-SiO_2 gap sample and the gap in vacuum of the 50 nm SiO_2-SiO_2 sample.

Through fitting, the thermal interface conductance between Au-SiO_2 of approximately 27.3 ± 6.49 MW/m^{2}K is obtained. This value is lower than the reported value between Au and SiO_2 of ~55 MW/m^{2}K because the Au and SiO_2 contact in our sample is formed roughly by pressing together the top and bottom structures, not by physical vapor deposition [21,24]. The fact that the two values are of the same order of magnitude and reasonably close to each other confirms a good contact in the assembled structure and that the heat from the lasers could reach pillars without being hindered by air or contaminants. The fitted h_{gap} when the 50 nm Au-SiO_2 gap is in the ambient environment is approximately $9.69 \pm 10.92 \times 10^4$ W/m^{2}K, a value close to the expected h_{gap} of 7.32×10^4 W/m^{2}K, but the uncertainty in our analysis is very large. Even though there is a different in the fitted values, the large uncertainties associated with our fitting process prevents us from proclaiming any discrepancies between these data sets. The 50 nm SiO_2-SiO_2 gap sample in the high vacuum environment yielded an unrealistic negative value when fitted, suggesting that the actual value cannot be identified within our uncertainty. As seen in Fig.3.8, there are clear differences between the data sets, which is further evidence that we obtained a 50 nm gap with good sensitivity to distinguish the pillar region from the gap region filled with the ambient air and with vacuum.

The 10 nm gap samples, either sandwiched between the parallel Au and SiO_2 layers or SiO_2 and SiO_2 layers are measured in the same way. Because of the reduced dimension and the optical property matching effect, the 10-nm SiO_2-SiO_2 gap sample is expected to exhibit the largest value of h_{gap}. Fig.3.9-(a) shows the illustrative difference in sample configurations between the 10 nm Au-SiO_2 and SiO_2-SiO_2 gap samples. Fig. 3.9-(b) shows the difference in the experimental phase lag data as a function of heating frequency between the 10-nm SiO_2-SiO_2 and

Au-SiO_2 gap samples in high vacuum (5×10^{-5} Torr) and in the ambient environment with their fits to the analytically calculated phase lag values.

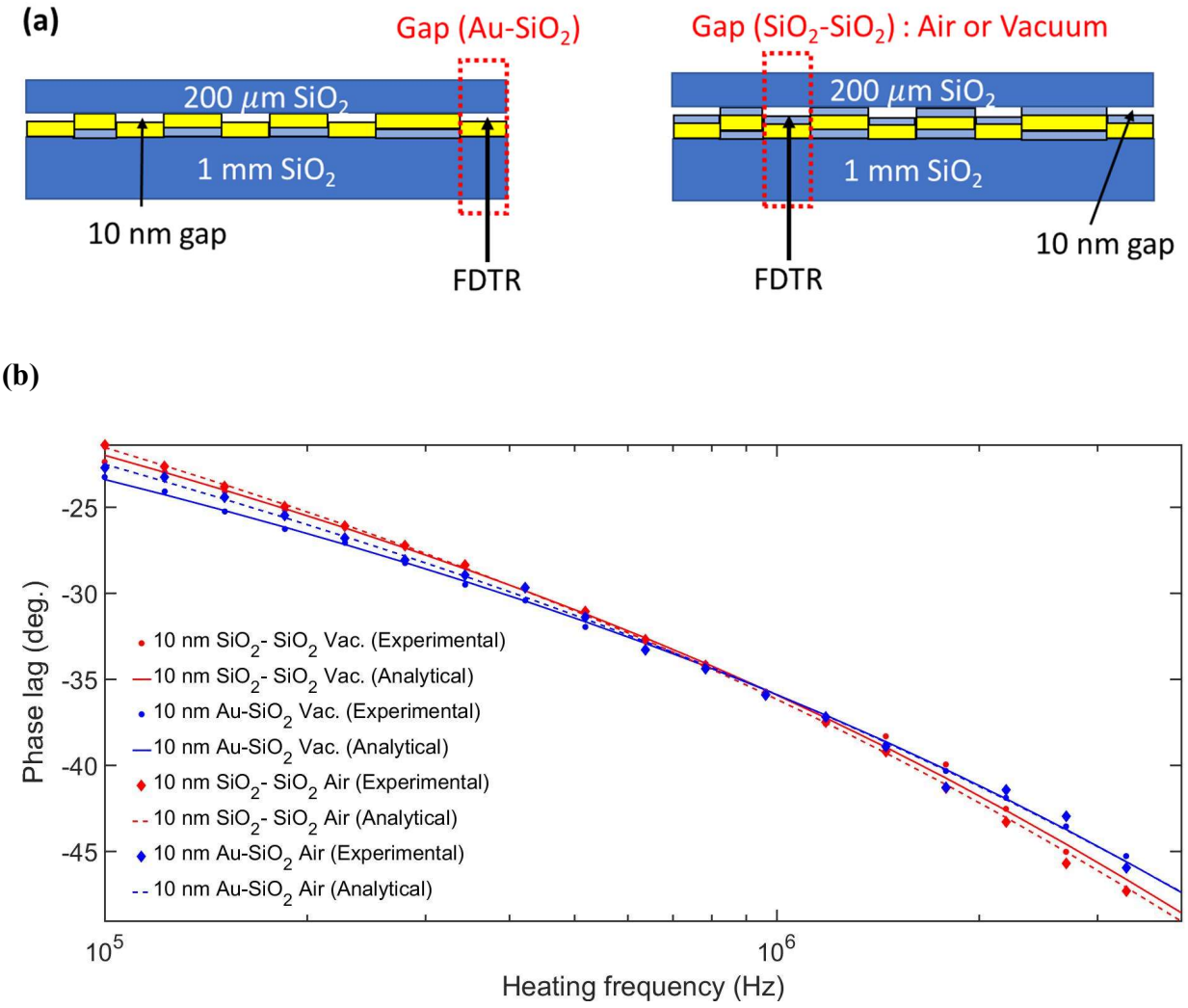

Fig.3.9. (a) Illustrations of where the measurements are performed (b) Experimentally obtained phase lag data as a function of frequency for 10 nm SiO_2-SiO_2 and Au-SiO_2 gap cases in vacuum and in the ambient air with their fits to the analytically calculated phase lag

The fitted values of h_{gap} are negative in the 10 nm Au-SiO2 gap case in vacuum, similar to the 50 nm SiO2-SiO2 gap case in vacuum. This again suggests that the actual value cannot be clearly identified within our uncertainty. h_{gap} of $3.23 \pm 9.73 \times 10^4$ W/m^{2}K in vacuum is obtained for the 10 nm SiO_2-SiO_2 case in vacuum. Even though it is promising that the fitted value is not negative and is close to what we predicted in Table 3.2, the large uncertainty in our fitting analysis does not help us to accurately report a final value. In the ambient environment, the 10 nm Au-SiO_2 sample showed h_{gap} of $4.27 \pm 9.12 \times 10^4$, while the 10 nm SiO_2-SiO_2 case showed that of $1.43 \pm 1.51 \times 10^5$ W/m^{2}K. Here, we again have an issue of large uncertainties for all the fitted values, which prevents us from claiming that we accurately measure the near-field radiative effect via FDTR. However, we are at least able to confirm good contact with intended gap thicknesses between the top and bottom structures based on the different phase lag behaviors on the pillar and the gap regions. Moreover, the fact that the phase lags shown in Fig.3.9 differ from one another despite of large uncertainties in the fitted values holds promise that the different fitting analysis can yield better results.

3.7 Differential analysis for phase lags

As explained previously, even though we obtain the fitted h_{gap} both in vacuum and in the air that are close to the analytically calculated h_{gap}, the uncertainties in the fitted values are very high. Based on the uncertainty analysis, this could be primarily attributed to high sensitivity to the spot sizes of our lasers in our measurements. As shown in Fig.3.10-(a), when the spot size changes by 5% from 3.2 μm, the fits do not change very significantly with ~ 0.5-degree change in phase lags. On the other hand, the fitted h_{gap} values change significantly at least by an order

of magnitude. Given this issue of high sensitivities in our data sets, we can fit for the differences in the phase lags between two data sets instead of fitting for the experimental phase lags in each data set.

(a)

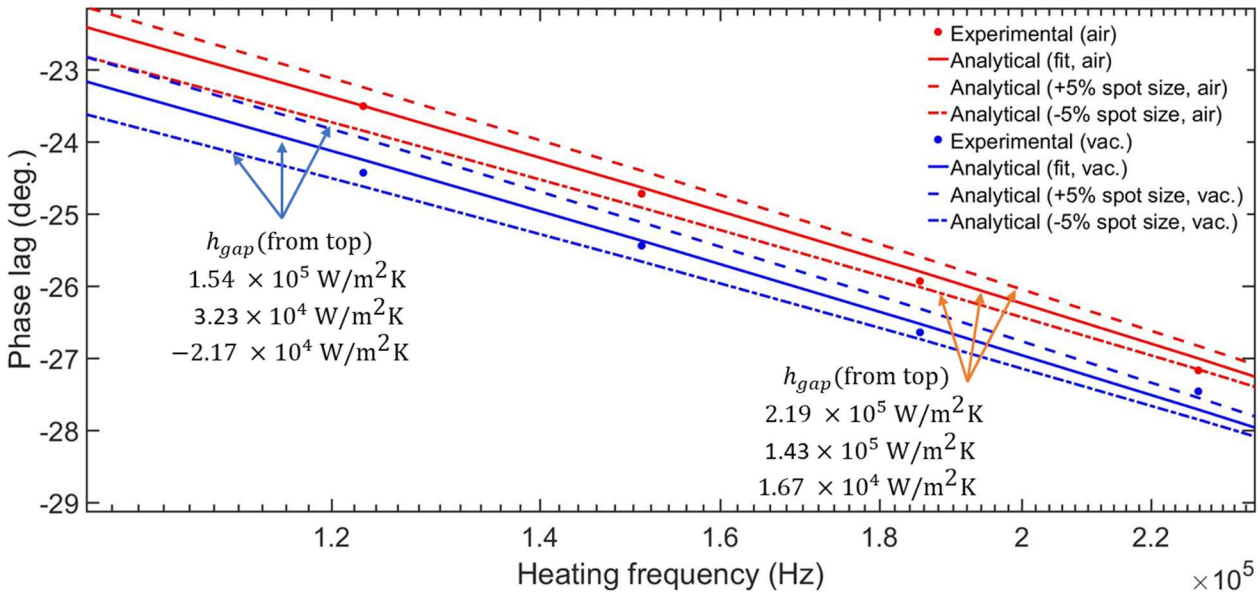

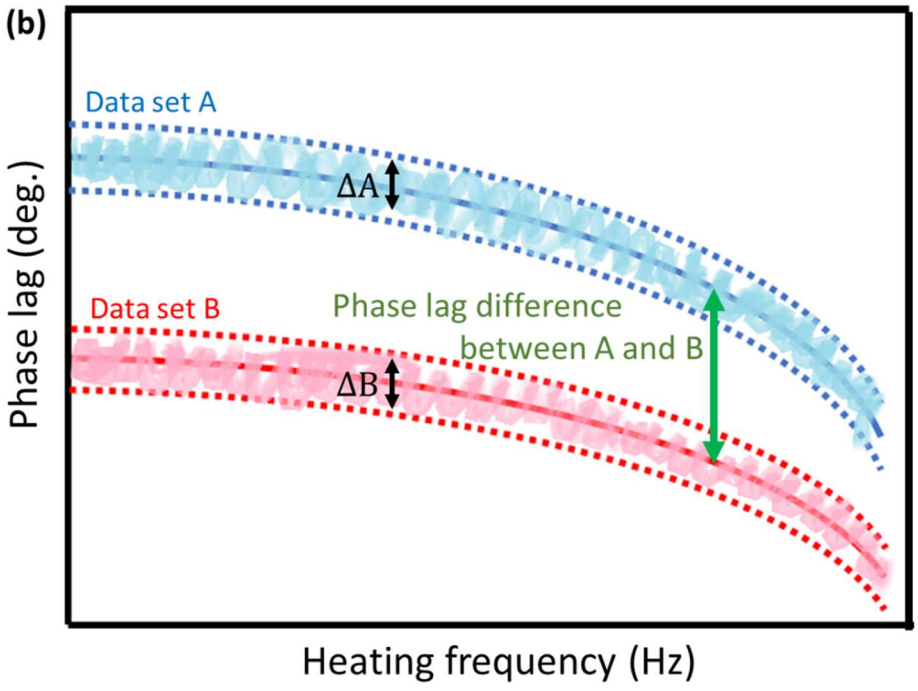

Fig.3.10. (a) The experimentally obtained phase lag values of the 10 nm SiO_2-SiO_2 gap sample in vacuum and in the ambient environment shown with the analytically calculated ones. The analytically calculated phase lags and the corresponding fitted values change when the spot size change between 3.05 μm and 3.35 μm with 0.15 μm increment. (b) An illustrative description of the phase lag differential analysis for two different data sets with associated uncertainties.

Let us imagine a data set A containing a set of phase lag values that relatively stay constant as a function of frequency for simplicity, and another data set B that behaves the same way. Both A and B will have associated uncertainties, ΔA and ΔB. If ΔA and ΔB are sufficiently small, the difference in phase lags between A and B will not vary no matter how sensitive each data set is. An illustrative description is shown in Fig.3.10-(b). Because we observed that the differences in experimentally obtained phase lags between the air and the vacuum data are existent, fitting for the difference in phase lags between the air and vacuum data to obtain h_{gap} can be attempted to reduce large uncertainties.

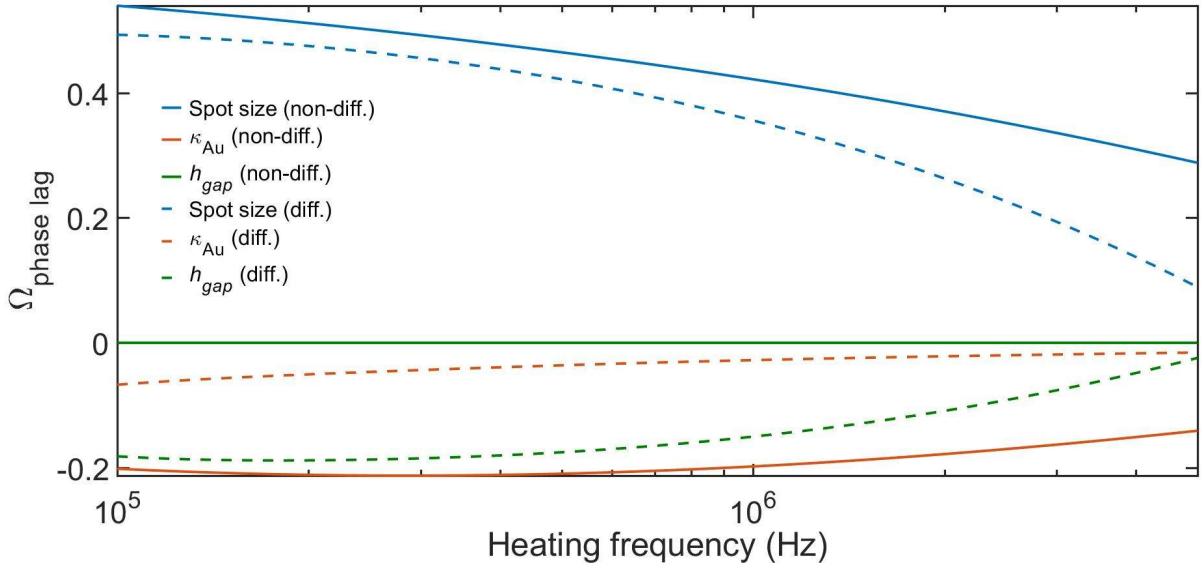

Fig.3.11. The degree of change in phase lags, Ω, due to 0.1% change in fitting parameters (spot size, κ_{Au}, h_{gap}) plotted as a function of heating frequency for two different fitting processes; non-differential and differential fitting for phase lags.

Fig.3.11 shows the degree of change in analytically predicted phase lags when some of the fitting parameters (spot size, κ_{Au}, h_{gap}) change by 0.1 % as a function of heating frequency. The analysis is performed for two situations when the regular phase lag fitting process (non-diff.) is performed or when the phase lag differential fitting process (diff.) is performed. This analysis follows the same analytic methods reported in Refs. [22,23]. Ω in Fig.3.11 represents the degree of change and can be mathematically represented as $\frac{d(\text{phase lag})}{d\ln(\text{fitting parameters})}$. If the absolute value of Ω is high, it means that we have a high sensitivity to that particular parameter. While it is good to have high Ω for h_{gap} because we want to be sensitive to it to differentiate a near-field radiative effect, high Ω in other parameters such as κ_{Au} or spot size is not ideal as our fitting result will be highly dependent on it. From Fig.3.11, it is apparent that the change in spot size will have the

most significant influence on fitting based on the highest Ω involved. However, Ω due to the spot size change decreases when we use the differential fitting process. The same happens in κ_{Au}. Moreover, Ω due to the h_{gap} change increases when the differential fitting is used. This shows a possibility that our large uncertainties in the fitted values may decrease when we fit for the difference in phase lags between the vacuum and the ambient data sets.

(a)

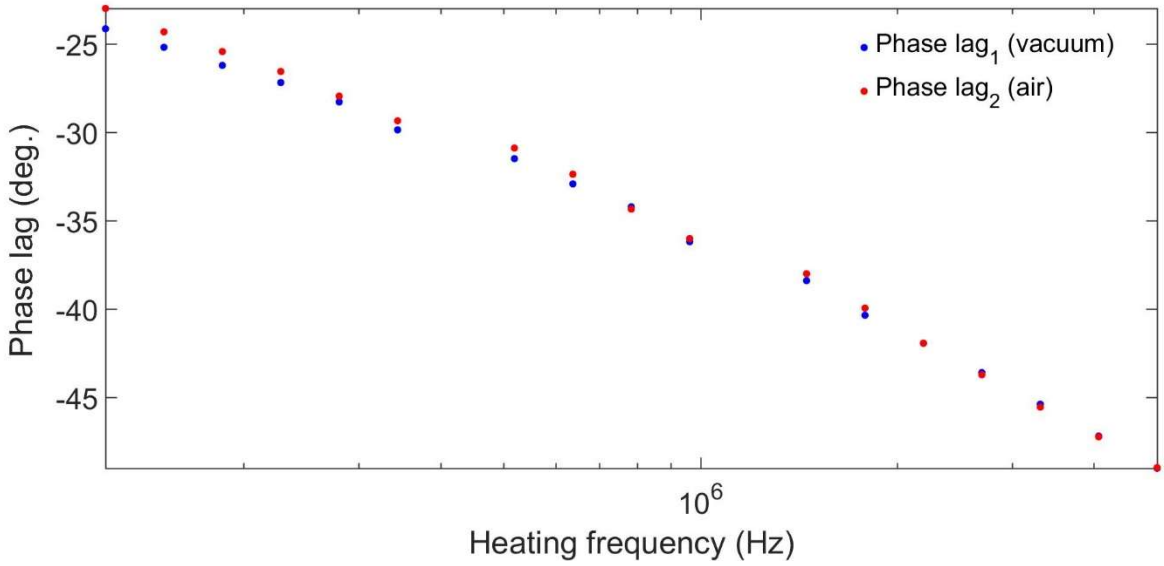

(b)

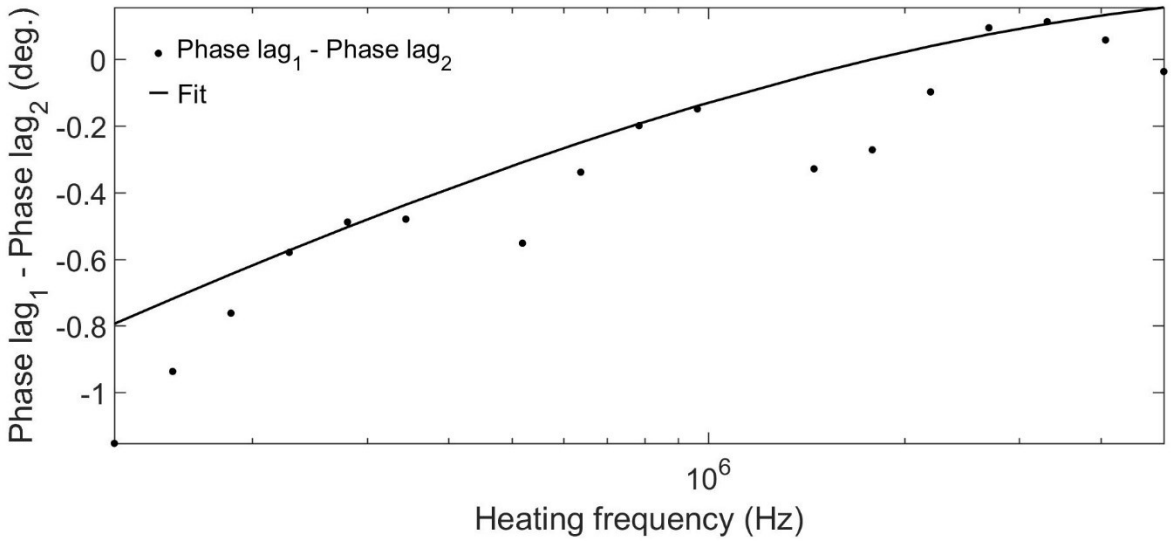

(c)

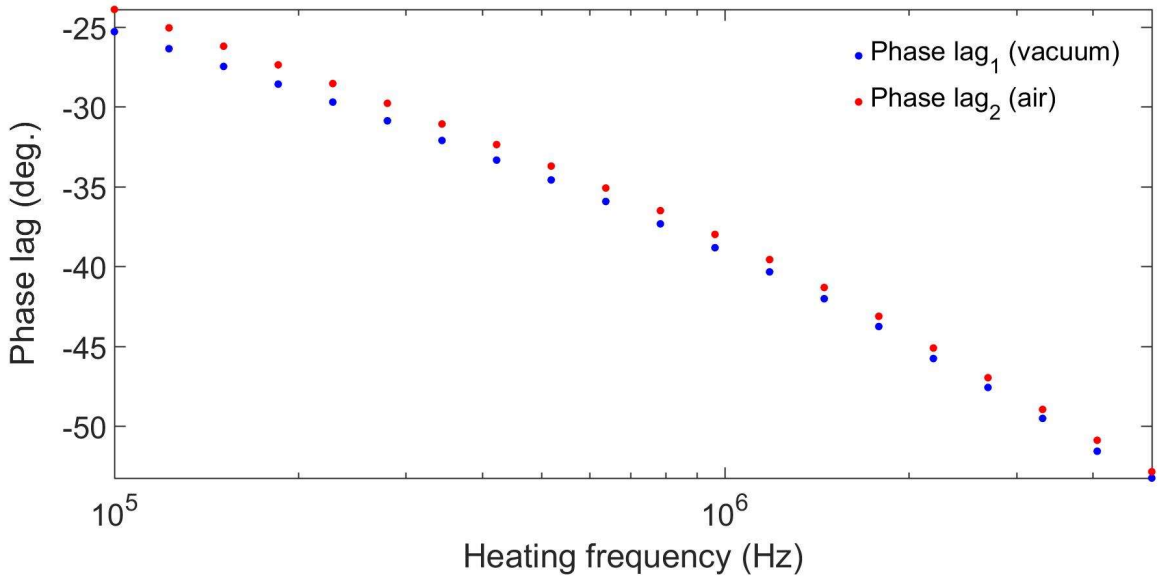

(d)

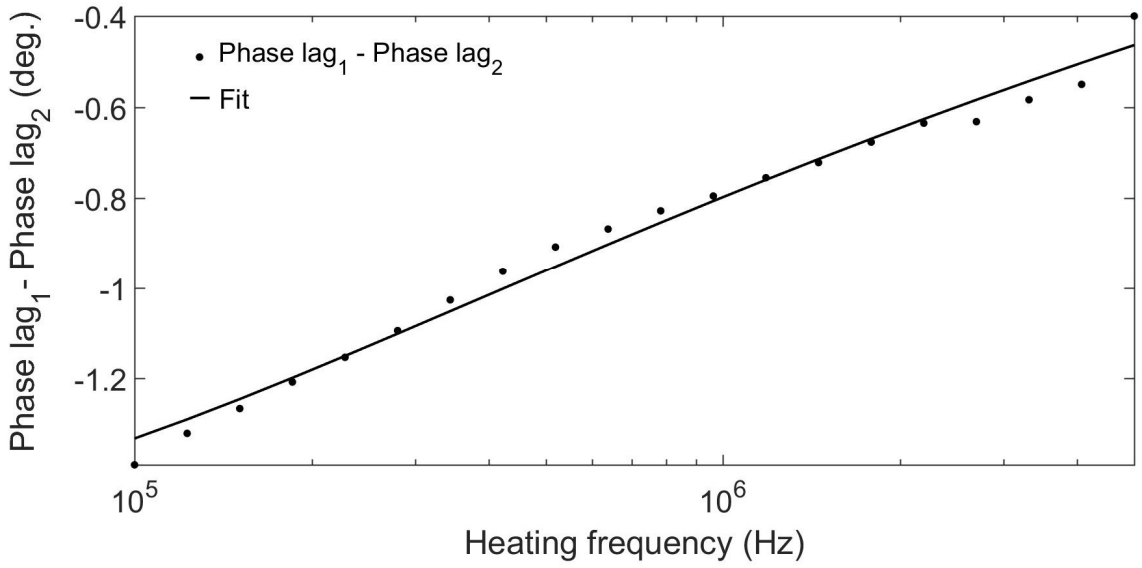

Fig.3.12. (a) The experimentally obtained phase lags in vacuum and air on the 10 nm Au-SiO_2 gap sample and (b) their difference with the analytical fit. (c) and (d) represent the same analysis results on the 10 nm SiO_2-SiO_2 gap sample. Some of the outliers are excluded in fitting.

The results of the differential analysis of the 10 nm Au-SiO_2 and 10 nm SiO_2-SiO_2 gap samples when they are exposed to air are shown in Fig. 3.12. The minuends (a quantity from which another is to be subtracted) for both cases are the phase lags when the gap samples are in high vacuum (1×10^{-5} Torr), while the subtrahends (a quantity to be subtracted from another) are the phase lags in the ambient air atmosphere. The minuends are obtained by assuming that h_{gap} will be the same as expected values shown in Table 3.2; 1 W/m^{2}K and 2.6×10^4 W/m^{2}K for the Au-SiO_2 and SiO_2-SiO_2 cases, respectively. As a result of the differential fitting process, the 10 nm Au-SiO_2 shows h_{gap} of $1.15 \pm 0.34 \times 10^5$ W/m^{2}K and the 10 nm SiO_2-SiO_2 shows $1.65 \pm 0.49 \times 10^5$ W/m^{2}K. As expected, the large uncertainties decrease significantly for both cases. Moreover, the resultant fitted h_{gap} are very close to the expected values shown in Table 3.2. From this, it can be concluded that we were able to observe enhancement in h_{gap} with a decreasing gap size and with matching SiO_2 materials, which could be attributed to the near-field radiative effect. Fig.3.13 shows overall experimental results of the non-differential and differential analysis for different gap samples.

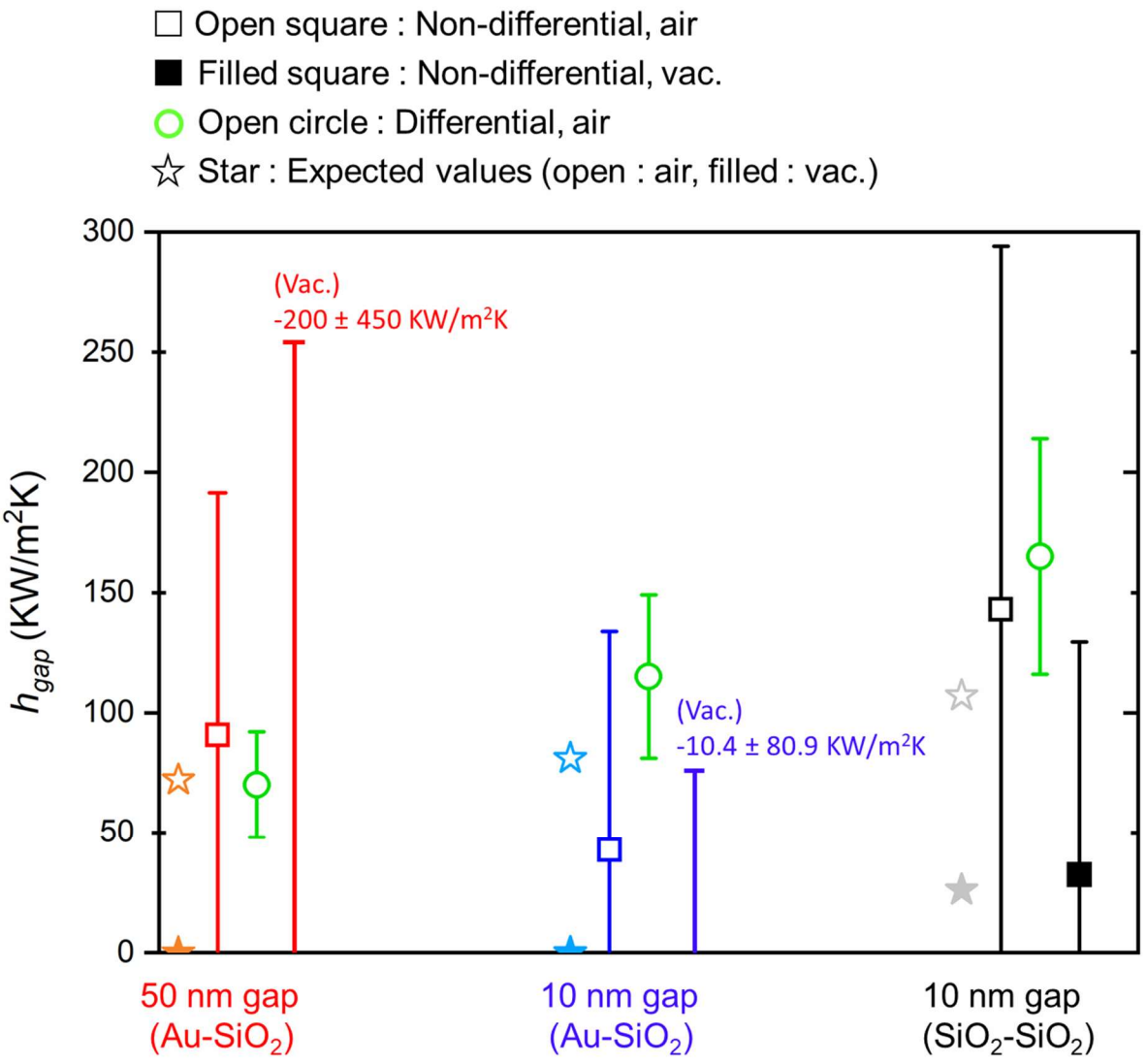

Fig.3.13. Overall analysis results for different gap samples. Both non-differential and differential analysis results are shown in squares and circles, respectively. The open symbols represent the air case and the filled symbols represent the vacuum case. The expect values for the air and vacuum cases are shown for each case.

3.8 Conclusions

In this study, we fabricate a thermomechanically stable nanostructured gap to enable measurements of the near-field radiative effect via the optical FDTR technique. By mechanically pressing the top and bottom patterned structures, we are able to construct a 10 nm and 50 nm gap structure that is sandwiched either between Au and SiO_2 or SiO_2 and SiO_2 layers. The existence of nanostructured gap with the intended thicknesses is confirmed by the measurement results of h_{gap} in the air and in vacuum that match reasonably well with the analytically calculated values despite of large uncertainties. For the 10 nm gaps where the near-field radiative effect is supposed to be strongly present, we measure h_{gap} of $4.09 \pm 9.73 \times 10^4$ W/m^{2}K and $1.43 \pm 1.51 \times 10^5$ W/m^{2}K in the vacuum and ambient environment for the SiO_2-SiO_2 case. For the Au-SiO_2 case, $-1.38 \pm 8.95 \times 10^4$ W/m^{2}K and $4.27 \pm 9.12 \times 10^4$ are measured in the vacuum and the ambient environment, respectively. However, there are large uncertainties in these fitted values. This issue was resolved by fitting for the difference in the phase lags between the vacuum and air data sets; through this differential analysis, h_{gap} for the 10 nm Au-SiO_2 gap sample is 1.15 ± 0.34 W/m^{2}K and 1.65 ± 0.49 W/m^{2}K for the 10 nm SiO_2-SiO_2 gap sample in the ambient air environment. We confirm that the large uncertainties decrease significantly with the fitted values matching very close with the expected ones.

3.9 Supporting information

3.9.1 Stress analysis

Under a uniform pressure load over the top surface, a cantilever beam fixed at both ends as shown in Fig.3.S1 can deflect by $\delta_{max.}$ at maximum according to Equation (3.S1) as follows :

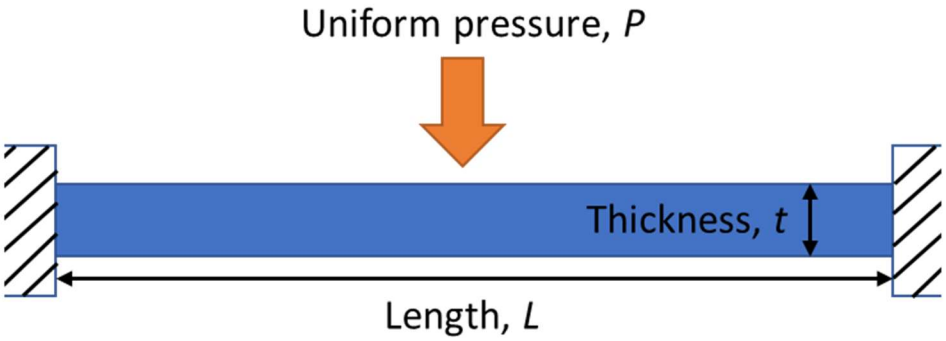

Fig. 3.S1. A cantilever beam fixed at both ends with uniform pressure load applied over top surface. Adapted and used with permission from T. Ganapathy

$$\delta_{max} = \frac{PL^5}{384E_0 I} \ , \tag{3.S1}$$

where P is the uniform pressure load, L is the total length of the beam, E_0 is the elastic modulus of the material, and I is the moment of inertia of the beam defined by Equation 3.8.2 as :

$$I = \frac{Lt^3}{12} \ , \tag{3.S2}$$

where t is the thickness of the beam. The width of the beam is assumed to be equal to its length. These equations are used to plot Fig.3.1-(b) in the main text.

3.9.2 Annular fin model

The annular fin model can explain how far the heat spreads radially on top of the gap when heating is induced by the laser within the sample as shown in Fig.3.S2.

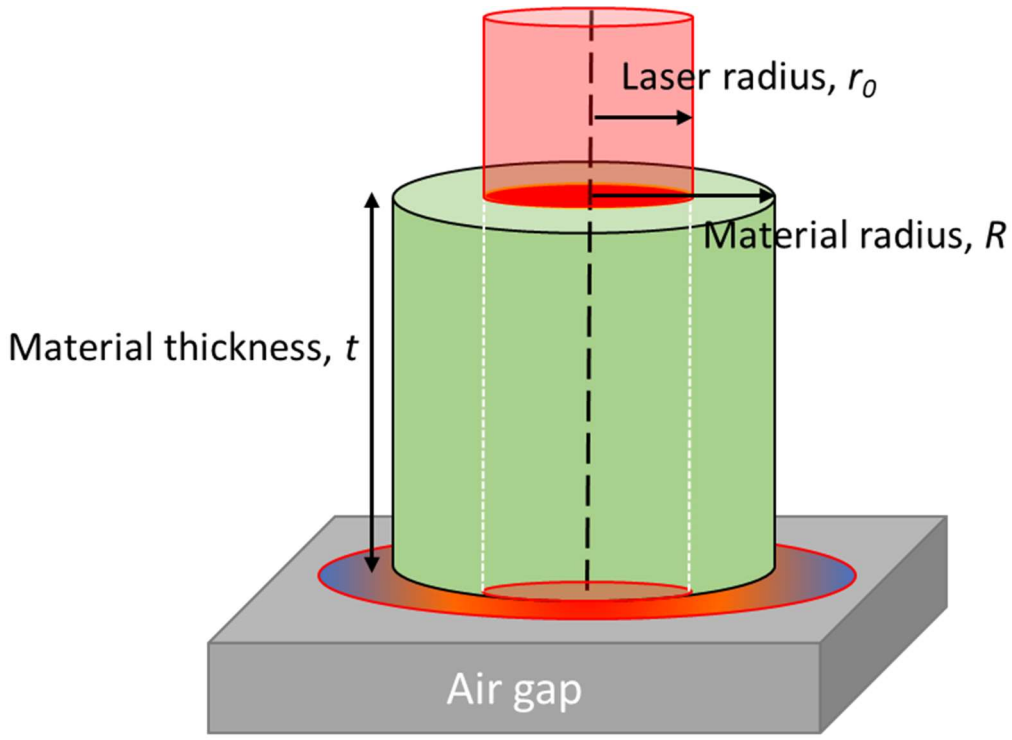

Fig. 3.S2. A schematic of a sample assumed in annular fin analysis with effective properties used to describe radial spreading of heat. Here, R represents the material radius; r_0, the laser spot size; and t, the material thickness. The material's outer surface is assumed to be adiabatic with the air assumed at the bottom. Adapted and used with permission from T. Ganapathy.

To explain the radiative heat exchange between the two parallel plates across the gap, two SiO_2 layers in our case, a heat transfer coefficient boundary condition is applied to the bottom-most side of the control volume. In addition, because we use the modulated heating with the laser, sinusoidal time dependence of temperature was assumed. Then, the following Equation 3.S3 can be established as :

$$\frac{d^2\theta}{dR^2} + \frac{d\theta}{RdR} - \left(\frac{h_{total}}{\kappa_{eff} \cdot t} + \frac{i\omega}{\alpha_{eff}}\right)\theta = 0 \quad , \qquad (3.S3)$$

where θ is the difference between local and ambient temperatures, *r* is the material radius, h_{total} is the total heat transfer coefficient which captures both conductive and radiative effects across the air gap, k_{eff} is the effective thermal conductivity of the material, t is the material thickness, ω is the laser modulation frequency, and α_{eff} is the effective thermal diffusivity of the material. For our study, the material is chosen to be 80 nm thick Au only. This is a conservative approximation because heat will also travel axially into the substrate with a penetration depth of $\sqrt{2 \cdot \alpha_{eff}/\omega}$ where α_{eff} will now be dependent on the SiO_2 plate's properties. Accordingly, the fin decay length, m^{-1}, which describes how far the heat will travel radially before it decays to 1/e of the original heating amplitude can be identified from Equation 3.S3 and is given by Equation 3.S4.

$$\mathrm{m}^{-1} = \left[\frac{\sqrt{\left(\frac{h_{tot.}}{t \cdot \kappa_{eff}}\right)^2 + \left(2\pi f \alpha_{eff}\right)^2} + \frac{h_{total.}}{t \cdot \kappa_{eff}}}{2} \right]^{-1/2} \tag{3.S4}$$

If we plot the normalized temperature rise, θ, for different heating frequencies f (0.1 MHz, 1 MHz and 10 MHz) as a function of radial position away from the laser spot, *r*, at given heat transfer coefficients h_{total} of 1.0×10^5 W/m^{2}K in the air gap, the corresponding results in Fig.3.S3 can be obtained.

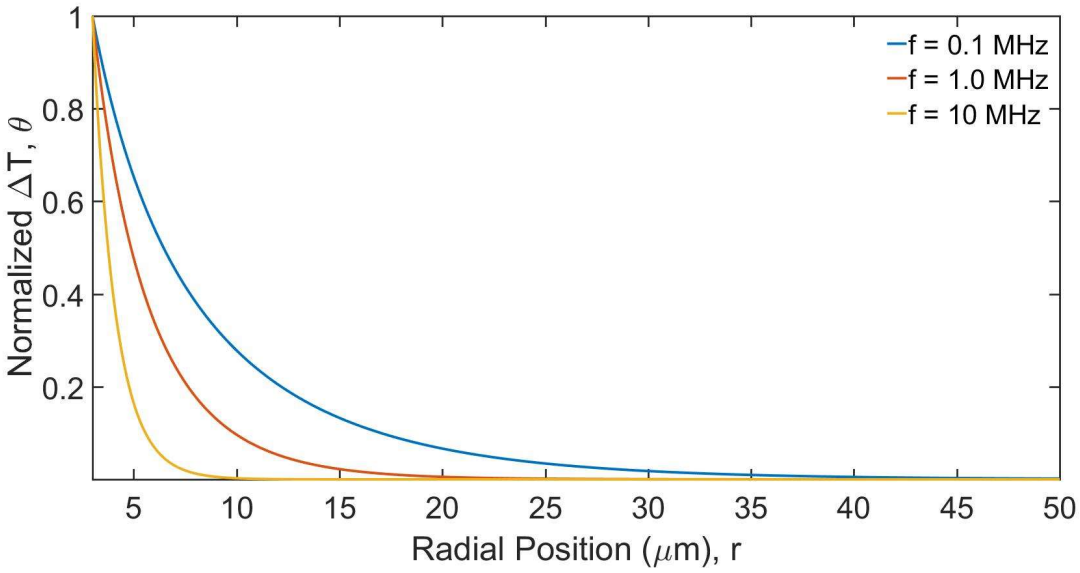

Fig.3.S3. Normalized temperature rise on the 80 nm Au layer due to modulated laser heating, θ, as a function of radial position away from the laser spot, r, for different frequencies, f (0.1 MHz, 1 MHz, 10 MHz) when the air gap has a total heat transfer coefficient of 1.0×10^5 W/m^{2}K.

According to Fig.3.S3, θ drops to 0 when the radial position r reaches ~40 μm away from the laser when the heating frequency is the lowest. This shows that when the supporting pillars are separated at least by ~40 μm away from each other with the think top membrane, the heat will not reach the pillars, making us wholly sensitive to the gap thermal properties. We used this number as a guideline for the pillar structure fabrication.

3.9.3 Mask configuration

To create an array of supporting pillars to support the gap structure, optical photolithography is used. To expose only certain areas to the ultraviolet (UV) light, a chromium mask that has a configuration as shown in Fig.3.S4 is used. The shaded squares define the pillars where the positive photoresist will stay. The white, clear space defines a channel where the positive photoresist will be exposed to the UV light and disappear. This cleared channel is needed to let the air in and out through the structure for vacuum measurements. The first column "I" in Fig.3.S4 had a spacing of 15 μm. The pillar spacing thereafter increases with a 5 μm spacing and goes up to 60 μm in column "9". Even though we identify 40 μm as the minimum pillar spacing in Section 3.9.2, we decide to go as small as 15 μm for better mechanical stability.

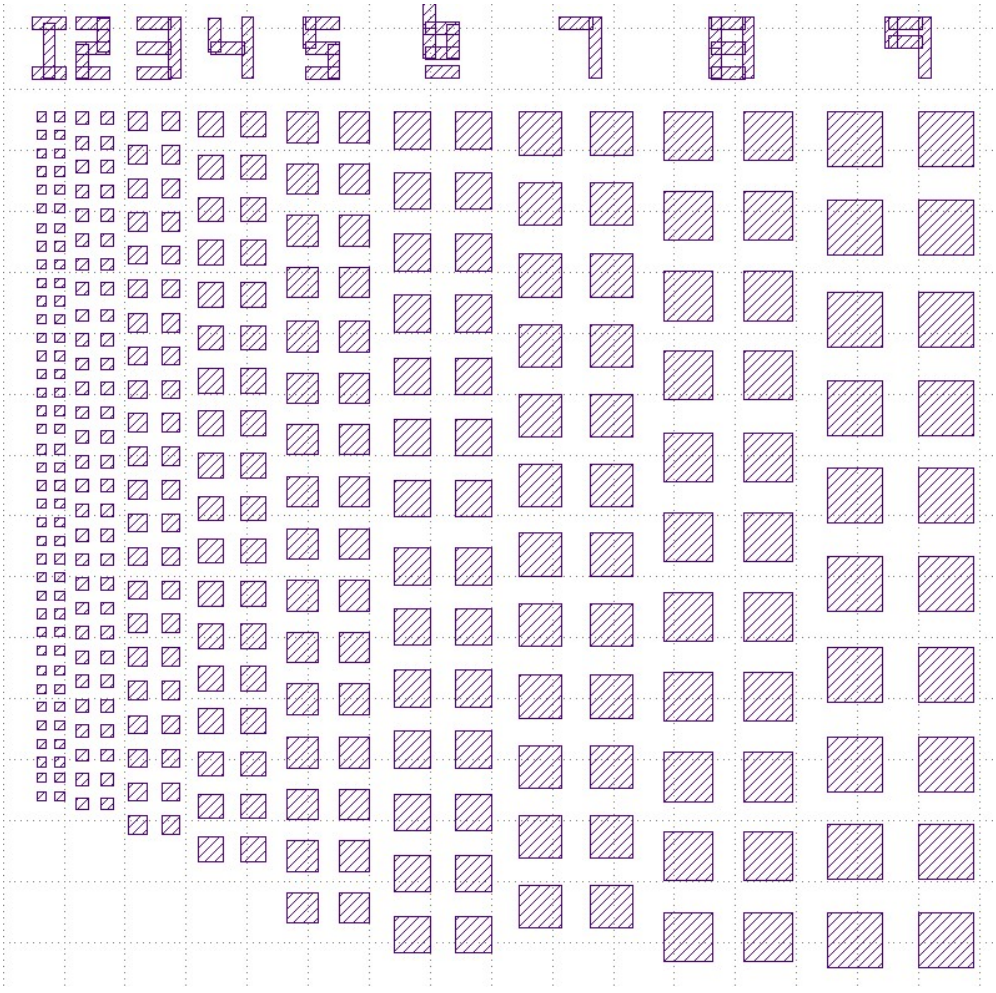

Fig.3.S4. A layout of the mask that is used in the photolithography process to construct supporting pillars

3.9.4 Thickness analysis

The X-ray reflectivity (XRR) fit agreed very well with the original data as presented in Fig.3.S5. The fitted result indicated the initial SiO_2 layer thickness of 10.3 nm, Au thickness of 66 nm and the final SiO_2 layer thickness of 14.1 nm. When these thicknesses changed by 2 nm, the quality of fit worsened appreciably.

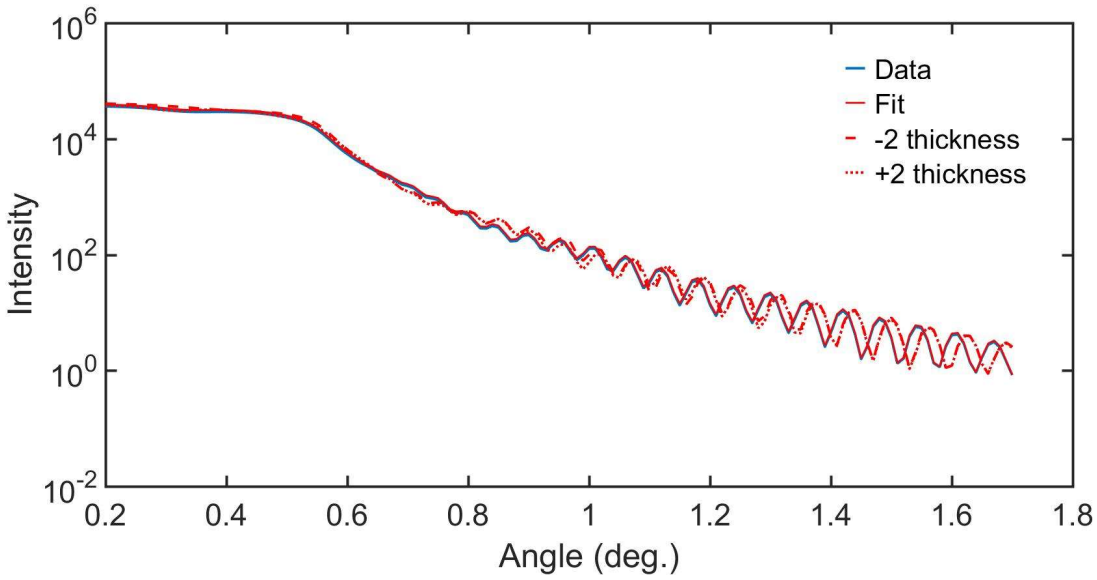

Fig.3.S5. The X-ray reflectivity (XRR) thickness analysis data for the 10 nm SiO_2-SiO_2 gap sample. The "-2 thickness" and "+2 thickness" lines represent when the fit is attempted with the intentionally wrong SiO_2 thickness with the 2 nm deviation.

3.9.5 Fitting parameters

Because the structure the heat travels differs when the measurements are made on the pillar region or the gap region, this needs to be considered when fitting the experimental data to the analytical solution. In the gap measurement case, the heat path also differs when the gap

exists between two parallel SiO_2 plates or Au and SiO_2 plates. How the fitting parameters are defined for each different case is represented in Table 3.S1.

Table 3.S1. Fitting parameters for each different measurement case

Gap (3.15 μm spot size)							
SiO_2-SiO_2 case	Top SiO_2	Au/SiO_2 interface	Au	Au/SiO_2 interface	Deposited SiO_2	Gap	Bottom SiO_2
Thermal conductivity (W/m·K)	1.38	0.0060	145	0.0060	1.4	Fitting	1.38
Density (kg/m^3)	2210	1	19,300	1	2210	1.2* Pressure	2210
Heat capacity (J/kgK)	670	1	129	1	750	710	670
Length (nm)	10^6	0.1	68	0.1	15 or 50	10 or 50	2×10^5
Au-SiO_2 case	Top SiO_2	Au/SiO_2 interface	Au	Au/SiO_2 interface	Deposited SiO_2	Gap	Bottom SiO_2
Thermal conductivity (W/m·K)	1.4	0.0055	145	N/A	N/A	Fitting	1.4
Density (kg/m^3)	2210	1	19,300	N/A	N/A	1.2* Pressure	2210
Heat capacity (J/kgK)	670	1	129	N/A	N/A	710	670
Length (nm)	10^6	0.1	66	N/A	N/A	10 or 50	2×10^5
Pillar (3.2 μm spot size)							
Au-SiO_2 case	Top SiO_2	Deposited SiO_2	Au/SiO_2 interface	Au	Au/SiO_2 interface	Bottom SiO_2	
Thermal conductivity (W/m·K)	1.4	1.4	0.0060	145	Fitting	1.4	
Density (kg/m^3)	2210	2210	1	19,300	1	2210	
Heat capacity (J/kgK)	670	750	1	129	1	670	
Length (nm)	10^6	0.1	68	N/A	0.1	2×10^5	

In Table 3.S1, "Top SiO_2" is the thick quartz slide that is exposed to the laser and the "Bottom SiO_2" is the thin quartz coverslip that is pushed by the holder screw. "Fitting" indicates that it is a fitting parameter. The "15 or 50" or "10 or 50" indicates different thicknesses that are intended for the 10 nm gap or 50 nm gap samples. The "Pressure" means that the density changed accordingly as the measurement pressure changes. The thermal conductivity of the Au layer is measured using the four-point probe measurements where the measured resistivity would be used to calculate the corresponding thermal conductivity based on the Wiedemann Franz law. The SiO_2 properties are obtained from the manufacturer and assumed to be the same for the deposited SiO_2 layers. The thicknesses of each layer are confirmed using the X-ray reflectivity technique except the gap thicknesses. When calculating uncertainties, 5% deviations in each parameter in Table 3.S1 are assumed and propagated through the calculations.

[1] Mathieu Francoeur: *Nat. Nanotechnol.*, 2015, vol. 10, pp. 206–8.

[2] S. Basu and Z. M. Zhang: *J. Appl. Phys.*, 2009, vol. 105, p. 093535.

[3] Lu Hu, Arvind Narayanaswamy, Xiaoyuan Chen, and Gang Chen: *Appl. Phys. Lett.*, 2008, vol. 92, p. 133106.

[4] Keunhan Park and Zhuomin Zhang: *Front. Heat Mass Transf.*, 2013, vol. 4.

[5] Bai Song, Yashar Ganjeh, Seid Sadat, Dakotah Thompson, Anthony Fiorino, Víctor Fernández-Hurtado, Johannes Feist, Francisco J. Garcia-Vidal, Juan Carlos Cuevas, Pramod Reddy, and Edgar Meyhofer: *Nat. Nanotechnol.*, 2015, vol. 10, pp. 253–58.

[6] Bai Song, Anthony Fiorino, Edgar Meyhofer, and Pramod Reddy: *AIP Adv.*, 2015, vol. 5, p. 053503.

[7] Xianglei Liu, Liping Wang, and Zhuomin M. Zhang: *Nanoscale Microscale Thermophys. Eng.*, 2015, vol. 19, pp. 98–126.

[8] Sajid Hussain, Shreya Kundu, Hyunsoo Yang, Aaron J. Danner, and Charanjit S. Bhatia: in *2015 Int. Conf. Opt. MEMS Nanophotonics*, IEEE, 2015, pp. 1–2.

[9] Sonali Mukherjee: *IEEE Trans. Magn.*, 2012, vol. 48, pp. 1704–9.

[10] S. N. Piramanayagam and Tow C. Chong: *Developments in Data Storage: Materials Perspective*, John Wiley & Sons, n.d.

[11] Kyeongtae Kim, Bai Song, Víctor Fernández-Hurtado, Woochul Lee, Wonho Jeong, Longji Cui, Dakotah Thompson, Johannes Feist, M. T. Homer Reid, Francisco J. García-Vidal, Juan Carlos Cuevas, Edgar Meyhofer, and Pramod Reddy: *Nature*, 2015, vol. 528, pp. 387–91.

[12] M. Laroche, R. Carminati, and J.-J. Greffet: *J. Appl. Phys.*, 2006, vol. 100, p. 063704.

[13] Hideo Iizuka and Shanhui Fan: *J. Appl. Phys.*, 2012, vol. 112, p. 024304.

[14] Raphael St-Gelais, Linxiao Zhu, Shanhui Fan, and Michal Lipson: *Nat. Nanotechnol.*, 2016, vol. 11, pp. 515–19.

[15] T. L. Bergman and Frank P. Incropera: *Fundamentals of Heat and Mass Transfer.*, Wiley, 2011.

[16] Lien Chin Wei, Lili E. Ehrlich, Matthew J. Powell-Palm, Colt Montgomery, Jack Beuth, and Jonathan A. Malen: *Addit. Manuf.*, 2018, vol. 21, pp. 201–8.

[17] Shinobu Masamune and J. M. Smith: *Ind. Eng. Chem. Fundam.*, 1963, vol. 2, pp. 136–43.

[18] Ray E. (Ray Emil) Bolz and George L. (George Lewis) Tuve: *CRC Handbook of Tables for Applied Engineering Science.*, CRC Press, 1973.

[19] E H Kennard: *Kinetic Theory of Gases : With an Introduction to Statistical Mechanics*, McGraw-Hill Book Co., New York; London, 1938.

[20] Bai Song, Yashar Ganjeh, Seid Sadat, Dakotah Thompson, Anthony Fiorino, Víctor Fernández-Hurtado, Johannes Feist, Francisco J Garcia-Vidal, Juan Carlos Cuevas, Pramod Reddy, and Edgar Meyhofer: 2015.

[21] Yibin Xu, Haitao Wang, Yoshihisa Tanaka, Masato Shimono, and Masayoshi Yamazaki: *Mater. Trans.*, 2007, vol. 48, pp. 148–50.

[22] Aaron J Schmidt, Ramez Cheaito, and Matteo Chiesa: n.d.

[23] Bincheng Li, J. P. Roger, L. Pottier, and D. Fournier: *J. Appl. Phys.*, 1999, vol. 86, p. 5314.

[24] Dong-Wook Oh, Seok Kim, John A. Rogers, David G. Cahill, and Sanjiv Sinha: Adv. Mater., 2011, vol. 23, pp. 5028–33.

Experimental measurements of thermal conductivity of HKUST-1 Metal-organic framework under different chemical loading conditions

4.1 Abstract

In this chapter, we present how κ of the HKUST-1 metal-organic framework (MOF) single crystal sample changes when it adsorbs different liquids (methanol, ethanol and water) via FDTR technique. κ of the thermally activated, pristine HKUST-1 sample yielded a value matches well with the simulated value. After full liquid adsorption, apparent changes in the crystal surfaces are observed in all cases as well as in κ. κ reduced significantly in all adsorption cases, nearly by 70% at maximum in ethanol adsorption, suggesting that the phonons are scattered more with the liquid molecules filled inside the HKUST-1 pores. Moreover, the sharp point contact between the liquid molecules may explain why κ reduces even though it seems more reasonable to increase based on the effective medium theory.

4.2 Introduction

Adsorption is a process where molecules in a multi-component fluid, such as a gas or a liquid are attached to a solid adsorbent (the solid that adsorbs the incoming gas or liquid) surface via the formulation of weak physical or strong chemical bonds [1,2]. Due to the possibility of developing simplest and most economically viable approaches to solve pollution, heath, and energy issues, adsorption has attracted a great deal of attention [1,3]. Ideal solid adsorbents will have large surface area and high porosity to capture as many molecules as possible. Of all the currently studied adsorbents, metal-organic frameworks (MOFs) have been actively considered

for their ultra-high porosity, large surface area, controllable properties, and uniform structure [4,5]. MOFs are organic-inorganic hybrid materials that are composed of metal ions and organic ligands linked together by coordination bonds [6,7]. There are numerous opportunities to use MOFs for chemical separations, hydrogen storage, drug delivery, water treatment and sensing [5,8,9]. Yet, before MOFs can be practically applied, a more sophisticated understanding of their thermal properties is needed due to the heat released by exothermic adsorption processes.

When an atom or a molecule is located on the surface, it has higher free energy than when it is inside the bulk material. Therefore, the unbonded atoms on the surface want to lower their free energy by forming bonds, making them readily accept atoms or molecules from gases or liquids that permeate the solid. This surface attraction governs overall gas-solid or liquid-solid adsorption processes [2]. Thermodynamically, the entropy of freely moving atoms or molecules in gases or liquids also decrease when they are adsorbed to solid surface. Based on the fundamental Gibbs free energy equation, $\Delta H = \Delta \dot{G} + T\Delta S$, the decrease in both free energy, $\dot{G}$, ($\Delta \dot{G} < 0$) and entropy S ($\Delta S < 0$) will entail a decrease in enthalpy, H, ($\Delta H < 0$) meaning that the adsorption process is typically exothermic. Consequently, the desorption process will be endothermic [2]. Therefore, it is obvious that effective heat exchange in the solid adsorbent is needed to control temperature and enhance adsorption and desorption processes for practical applications. Thus, developing higher thermal conductivity solid adsorbents including MOFs, is very important. Unfortunately, accurate analysis, specifically experimental measurements of MOF thermal conductivity is lacking as there are only a limited number of reports [10–12]. Huang et al., measured MOF-5's κ in a single crystal form at 300K and showed temperature-dependent data in 2007 [11]. In 2012, Liu et al. reported the thermal conductivity of a composite

made from MOF-5 and expanded natural graphite (ENG) at 300K, followed by Gunatilleke et al.'s work on the MOF-1 thermal conductivity measured as a function of temperature from 12K to 300K in 2017 [10]. Sun et al. reported κ of $Ni_3(HITP)_2$ MOF in a pressed-pellet form along with other thermoelectric properties in 2017 [13]. In 2017, another group reported cross-plane κ of ZIF-8 MOF thin films loaded with perfluorohexane (C_6F_{14}) using 3-omega method [14]. These previously reported results are shown in Fig.4.1. As yet, HKUST-1 has only been measured by two groups; the first article reported κ of 0.26 ± 0.02 W/m·K for HKUST-1 microcrystals that were deposited via printing technique on a zinc selenide (ZnSe) prism and stored in methanol until the measurements [15]. The other article reported κ of the HKUST-1 thin-film sample deposited by solution-based method before and after it was loaded with tetracyanoquinodimethane (TCNQ) molecules; 0.58 ± 0.04 W/m·K and 3.84 ± 0.27 W/m·K before and after loading, respecctivley [16]. Other interesting aspects such as the effect of pore size and shape on MOF thermal conductivity were reported where the increase in the effective pore size decreases the thermal conductivity on molecular dynamics (MD) simulations, but experimental results are needed to verify such claim [17].

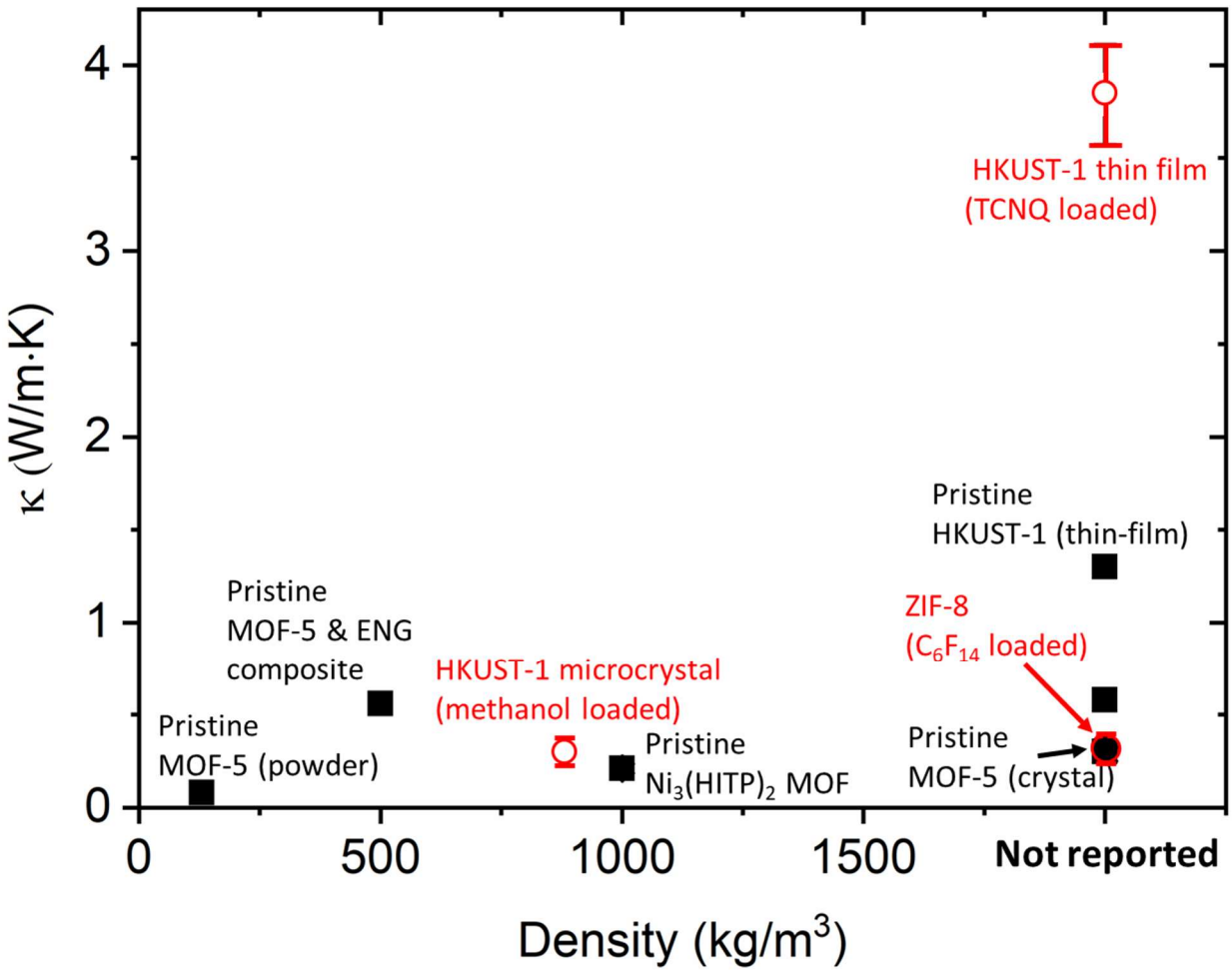

Fig.4.1. The reported κ as a function of density for various MOFs in different conditions. Error bars are not shown when the associated uncertainties are not reported. The "Not reported" values represent those values reported without any reported densities [10–16].

Moreover, there are ongoing debates and conflicting results regarding the change in MOF thermal conductivity under gas loading [18,19]. The authors of Ref. [18] performed MD simulations for idealized porous crystal structures to analyze how the thermal conductivity would change as carbon dioxide (CO_2) permeates the pores. They found that because of the increased phonon scattering as a function of the gas density the thermal conductivity drops from 0.75 ±

0.08 W/m·K down to 0.5 ± 0.05 W/m·K with the gas density of 8 CO_2 molecules per nm^3. However, another group reported a contradictory simulation result where they claimed an increase of thermal conductivity of MOF-5 as a function of hydrogen or deuterium gas density. Thus, it becomes our objective to conduct accurate thermal conductivity measurements for high-quality single crystal MOFs under different adsorption conditions.

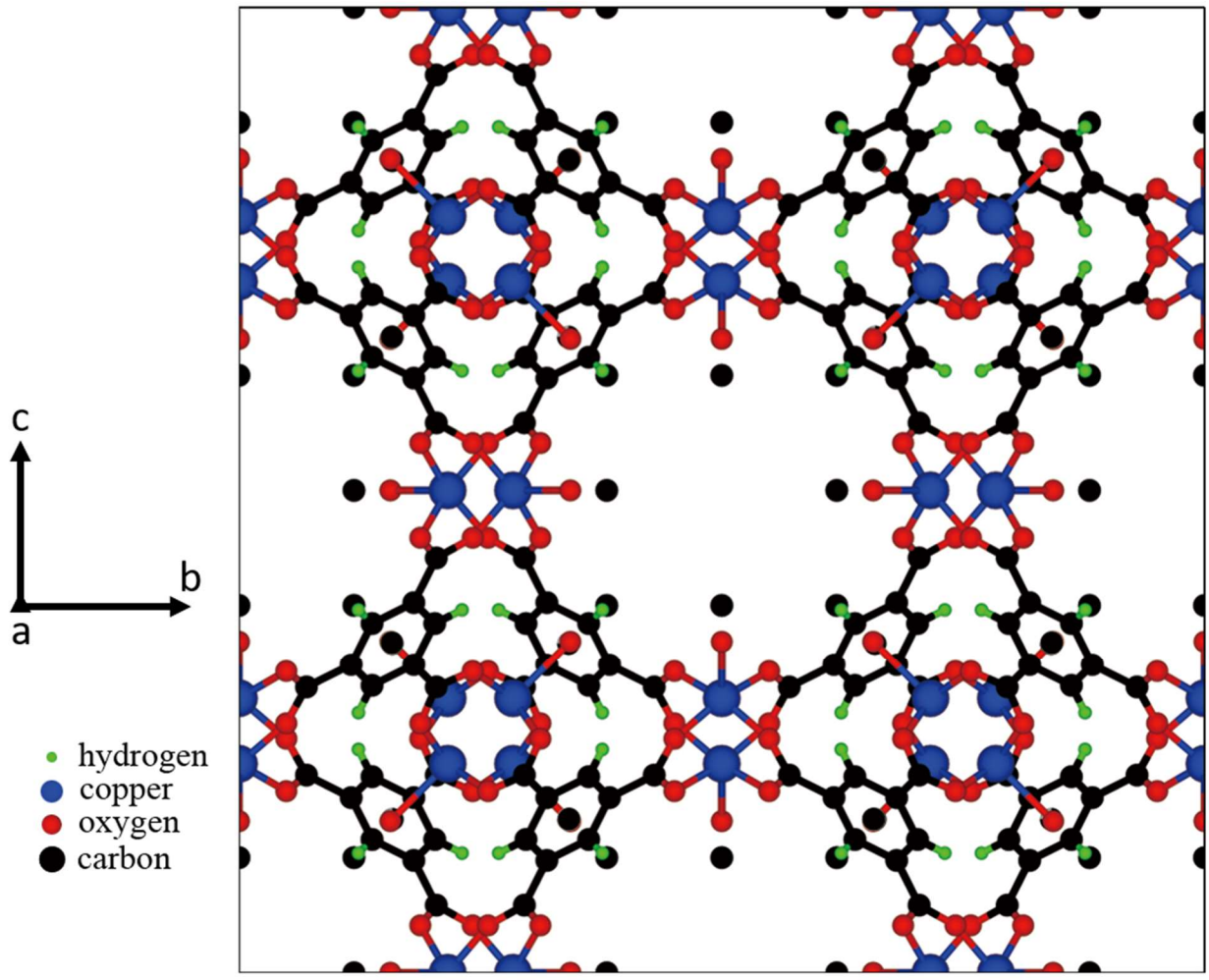

Fig. 4.2. An atomic structure of HKUST-1 MOF with green, blue, red and black spheres representing H, Cu, O and C atoms, respectively created on VESTA 3. The structural information (*.cif file) is obtained from Crystallography Open Database [20–23].

In this study, HKUST-1 is selected for thermal conductivity measurements because it can be synthesized as high-quality single crystals of large size. HKUST-1, also called 3D-{[$Cu_3(BTC)_2(H_2O)_3$]·~$10H_2O$} (BTC = benzene-1,3,5-tricarboxylate) as shown in Fig. 4.2 is composed of a periodic array of metal−organic complexes made by combining the BTC linker molecule with Cu_2^+ ions [24–27]. It is well known for its relatively simple synthesis that can be achieved with readily available reagents, large surface area and high chemical stability [28]. Because of simplicity in fabrication and distinguishable adsorption properties, HKUST-1 has become a reference MOF material as shown by nearly 3,000 related scientific articles based on Google Scholar search until June 2018 [28].

4.3 Experimental procedures

High-quality HKUST-1 single crystals are obtained from the Farha group at Northwestern University. The average crystal size is approximately 150 microns based on optical microscope images. Because it is important to have large, flat and smooth surfaces for laser-based frequency domain thermoreflectance (FDTR) measurements, good candidate crystals are carefully selected under the optical microscope. The detailed information about FDTR is provided in Chapter 1.6. FDTR is a non-contact optical technique where continuous wave pump and probe lasers are used to measure thermal transport. The pump laser beam (488 nm) is intensity modulated by an electro-optic modulator at different frequencies and acts as a periodic heat source when it is absorbed at the sample surface. This periodic heating causes oscillations of the temperature on the surface at the same frequency as the pump beam, but with a phase lag due to the sample's inherent thermal impedance. The probe laser (532 nm) is co-aligned with the

pump beam and measures the change in optical signal which is directly related to the temperature change of the sample based on thermoreflectance [29–31]. The temperature change of the sample is affected by the sample's thermal properties and is denoted in the phase-lag between the incoming pump and reflected probe lasers. The experimental phase-lag, as a function of pump modulation frequency, are fitted by an analytical solution to the three-dimensional dimensional heat diffusion equation for periodic surface heating of a layered solid by a radially Gaussian source [29]. The best-fit is achieved where the only fitting parameter is the desired sample thermal property – in this case, the HKUST-1 thermal conductivity.

(a)

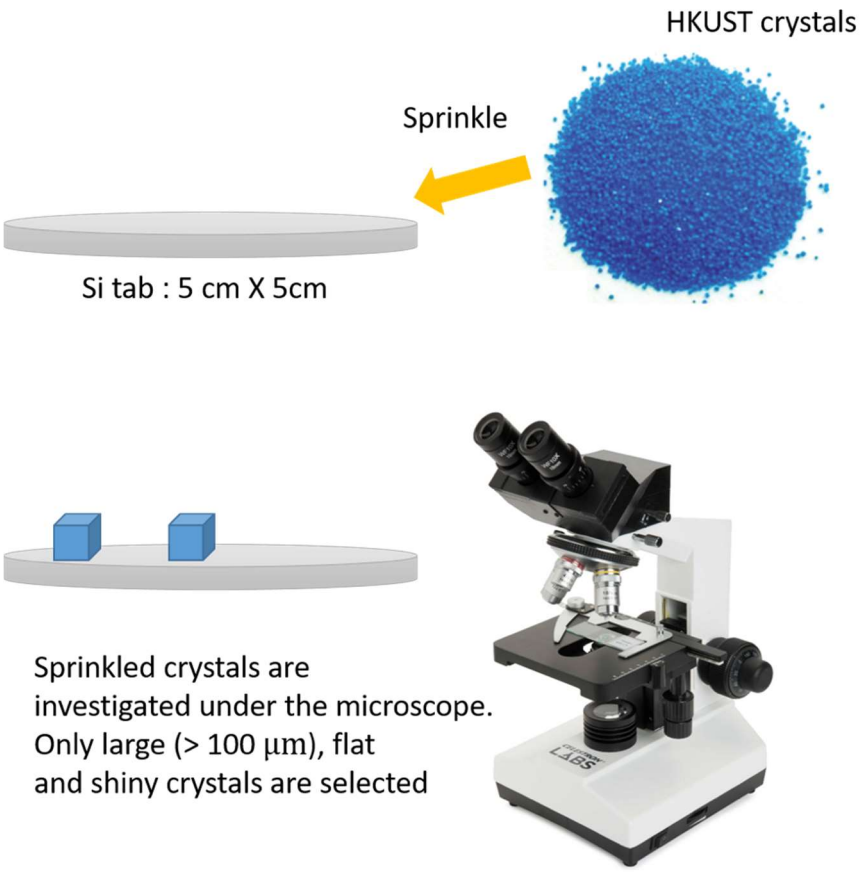

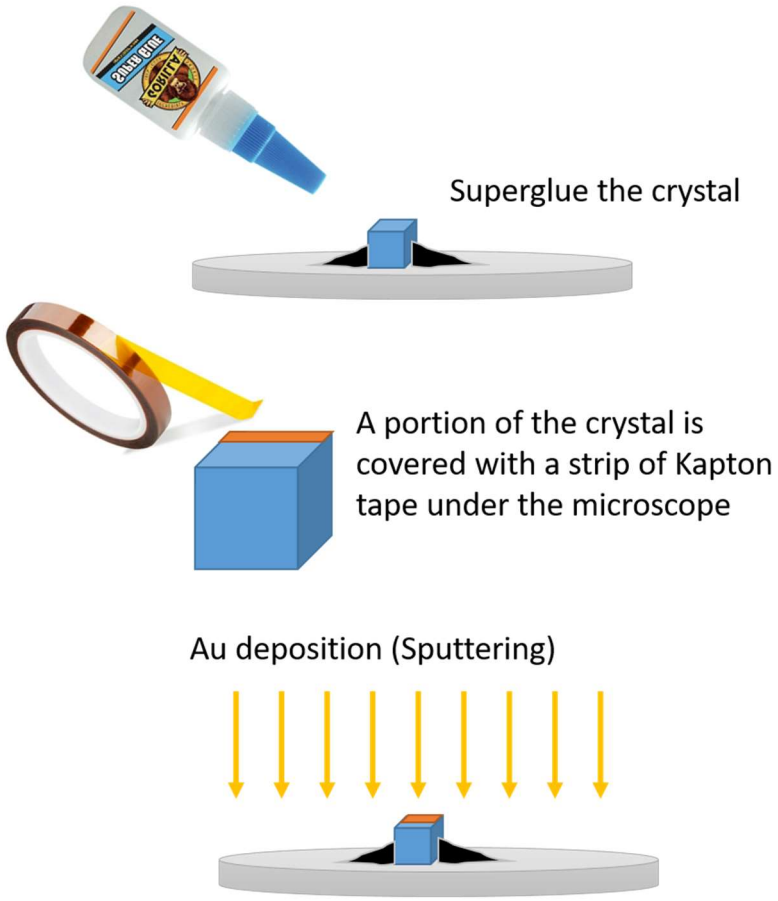

(b)

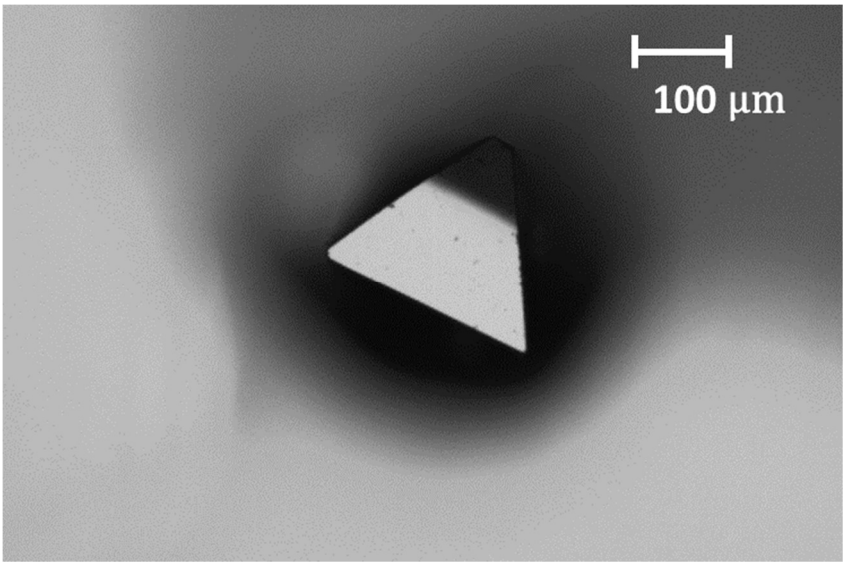

Fig. 4.3. (a) Illustrative descriptions of HKUST-1 MOF sample fabrication steps (b) 10X optical microscope image of the HKUST-1 MOF sample partially covered with Au-Pt layer.

In FDTR measurements, optical lasers are converted to a thermal source by the transducer layer. Typically, a gold (Au) layer of ~60 nm thick is used for this purpose, but our sensitivity analysis indicated that we gain more sensitivity on the change in thermal conductivity of MOF crystals when we have a lower thermal conductivity transducer layer. Therefore, we attempted to lower the thermal conductivity of the transducer by layering Au with platinum (Pt) due to Pt's low thermal conductivity and we specifically used a 30 nm Au (top) - 20 nm Pt (bottom) stacked transducer layer. The Au-Pt layer is sputtered on top of the HKUST-1 crystals at 1×10^{-5} Torr base pressure with an argon flow of 5×10^{-3} pressure and 25 sccm flow rate at room temperature. To ensure liquid adsorbates can enter the inner HKUST-1 crystal structure during later adsorption measurements, a portion of the crystal is covered with a strip of Kapton tape under the optical microscope for exposure to incoming liquids before sputtering. Fig.4.3 – (a) shows the illustration of overall experimental sample fabrication steps and Fig.4.3 – (b) shows the optical microscope image of the HKUST-1 crystal that is partially covered with the Au-Pt layer. The HKUST-1 MOF has an octahedron crystal structure. Because we observe the facet of such octahedral structure that is normal to the surface, we can conclude that the (111) face of HKUST-1 is exposed [47].

The thermal conductivity of pristine HKUST-1 crystals are measured by FDTR after activating them by vacuum thermal annealing at 150 ℃ for 12 hours and cooling back to room temperature, to remove adsorbed moisture. To measure how the thermal conductivity of HKUST-1 changes with liquid adsorption, three liquids (99% J.T Baker methanol, 99% Sigma Aldrich ethanol and deionized water) are considered. Methanol and ethanol are specifically chosen because of potential methanol and ethanol storage for bio-fuel purification technology; water adsorption is also an interesting subject for water filtration or separation applications [32–

34]. For adsorption, the partially coated HKUST-1 single crystal is immersed in methanol or ethanol for 1 hour, or 20 minutes for water, immediately following the thermal activation process. Full liquid adsorption in HKUST-1 is assumed as these times are already verified to yield full adsorption in a prior study [8]. After taking each crystal sample out of the liquids and briefly drying their surface with N_2, FDTR measurements are conducted at room temperature to determine their thermal conductivities.

4.4 Results and Discussion

The fits between the experimentally obtained phase lag values and the analytically calculated values for each adsorption case are shown in Fig. 4.3-(a) for selected FDTR measurements.

(a)

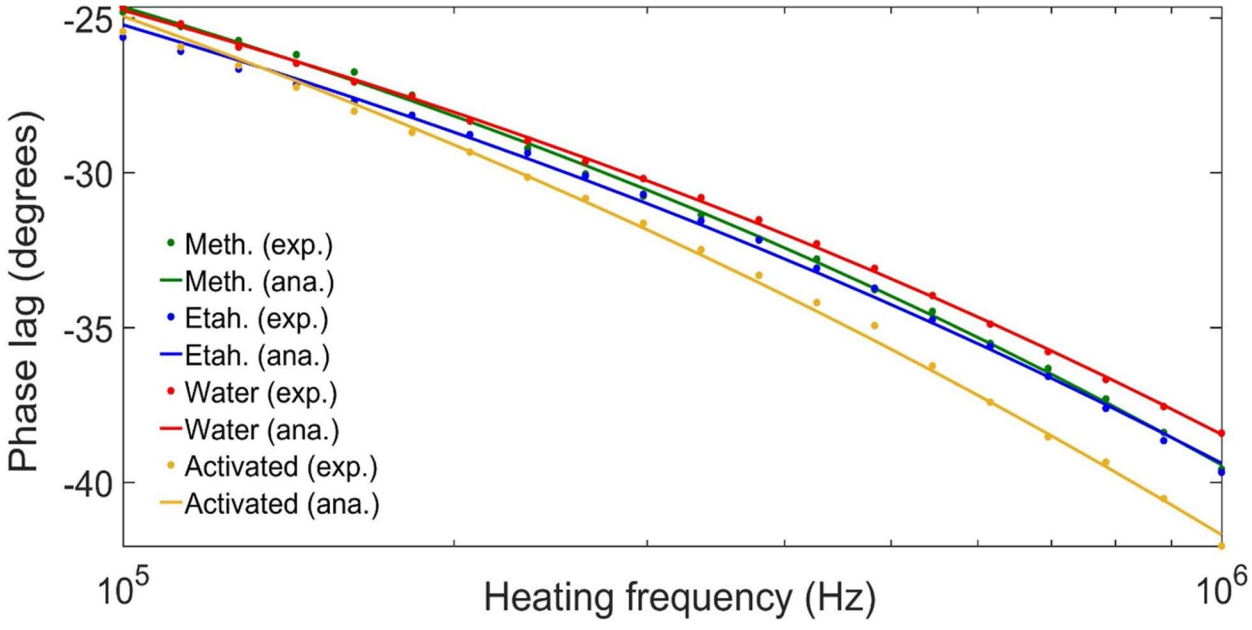

(b)

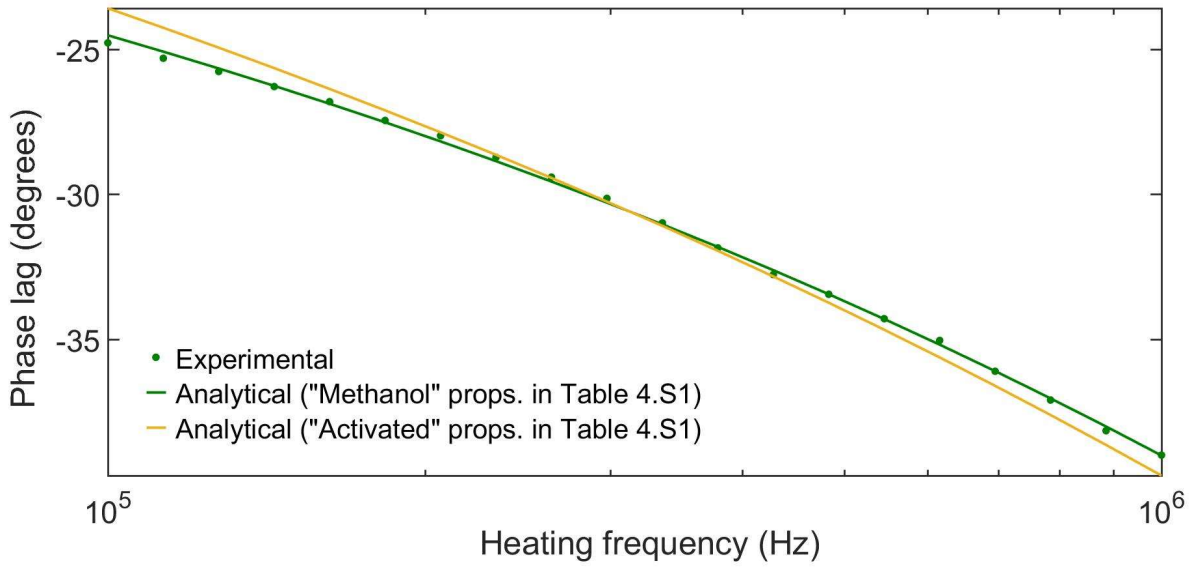

Fig. 4.4. The experimental phase lag values obtained via FDTR plotted as a function of heating frequency along with the analytically calculated phase lag values for (a) each adsorption case in different colors where "exp." and "ana." represent experimentally obtained phase lag value and analytical fits, respectively. (b) The methanol adsorption case (green) with the yellow line showing the analytically calculated phase lag values when the "Activated" vs. "Methanol" HKUST-1 MOF properties from Table 4.S1 in Supporting Information are used.

Only those data sets that showed relatively similar κ in the Au – Pt layer ($\pm$ 5%) in fitting with the reference Au – Pt layer sample deposited on a glass substrate are chosen. For fabrication of the reference Au-Pt layer, the glass substrate is placed inside the deposition chamber along with each crystal sample to ensure that the same Au-Pt layer material properties can be shared between the reference and the actual samples. The comprehensive material parameters that are used in fitting are included in Supporting Information.

As shown in Fig.4.4-(a), the experimentally obtained phase lag values and the analytically calculated values agreed very well with good fits for each case. Also, appreciable differences in phase lags are resulted when the HKUST-1 crystal adsorbs different liquids. This confirms that the liquid adsorption affects thermal properties of HKUST-1 crystal. Moreover, we could not achieve a good fit when the fitting is attempted with the properties of the pristine HKUST-1. For example, the experimental phase lags obtained for the methanol adsorption case (green dots in Fig. 4.4-(b)) did not yield a good fit when the fitting is attempted with using the activated HKUST thermal properties (yellow line in Fig. 4.4-(b)) as the MSE in fitting increased from 0.02 to 0.10. This provides an additional evidence that liquid adsorption occurred and shows that our obtained phase lag values for each adsorption case are unique.

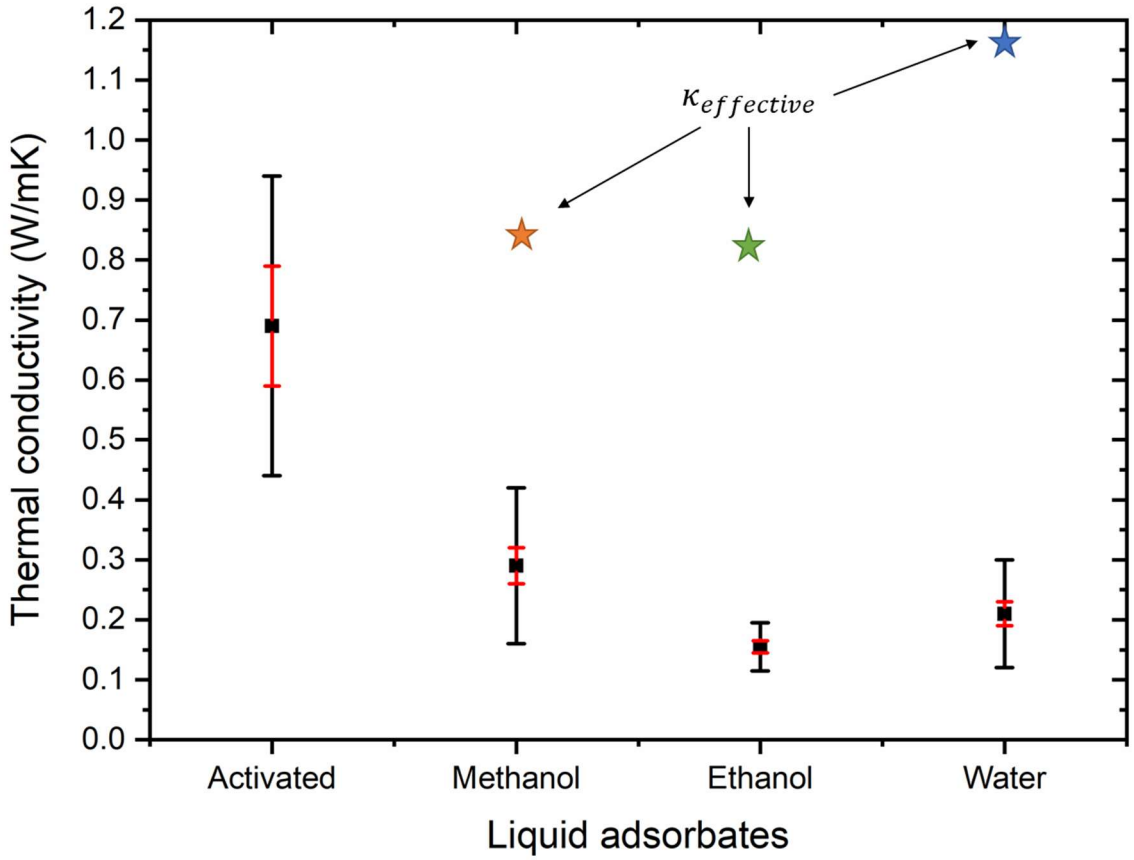

Fig. 4.5. Thermal conductivities of each adsorption case plotted with standard deviation error bars where the red error bars are for the standard deviations in each different thermal conductivity value and the black error bars are for the effective standard deviations of the whole set of data points resulted from propagation of uncertainties in fitting parameters. The stars represent effective thermal conductivity, κ_{eff}, for each liquid adsorption case computed based on the effective medium theory.

Fig.4.5 shows that as the HKUST-1 crystal sample adsorbs liquid molecules, its thermal conductivity decreases significantly. Each thermal conductivity value represents an average of fitted values of the FDTR data sets selected with the selection process mentioned earlier with standard deviations shown as error bars. The red error bars in Fig.4.4 represent standard deviations in different values of thermal conductivity in each case. On the other hand, the black error bars indicate the standard deviations resulted from propagation of uncertainties in fitting parameters in Table 1. These standard deviations are now the "effective" standard deviations that represent the standard deviations of multiple number of data points, accounting for a standard deviation of each independent measurement based on the uncertainty in a single measurement. Such effective standard deviations are calculated by first obtaining an average of the final reported value, $\bar{x}$, as follows :

$$\bar{x} = \frac{1}{N}\sum_{i=1}^{N} x_i \quad , \tag{4.1}$$

where N is the total number of independent measurements x_i. Then, the effective standard deviation, $\bar{\sigma}^2$, is :

$$\bar{\sigma}^2 = [\frac{1}{N}\sum_{i=1}^{N}(\sigma_i{}^2 + x_i{}^2)] - \bar{x}^2 \quad , \tag{4.2}$$

where the σ_i represent the uncertainty of each independent measurement x_i. The uncertainties in fitting parameters relied on variations in reported material properties, sensitivity in XRR thickness measurements and the spot size variations based on a knife-edge technique [22,35–38]. The FDTR measurement values with uncertainties are given in Supporting Information.

The decreasing trend in thermal conductivity as adsorption occurs is consistent with published simulation data on carbon dioxide (CO_2) gas adsorption, where the drop in thermal conductivity is attributed to increased phonon scattering as the vacant HKUST-1 crystal pores are filled with the adsorbate molecules [18]. The most significant decrease is observed in the ethanol adsorption cases although water and methanol both showed similar drops in thermal conductivity. This indicates that the heat-carrying phonons in the HKUST-1 MOF crystal are more scattered as the liquid molecules fill in the crystal pores, and this affects any benefit of parallel conduction through the liquid alone. The effective thermal conductivity (κ_{eff}), assuming that the HKUST-1 MOF and permeated liquid are parallel conduction channels, is calculated and is plotted in Fig.4.5. For the effective thermal conductivity calculations, the following relationship, $\kappa_{eff} = \kappa_{MOF} + \kappa_{adsorbate} \cdot F_{void}$, is used where F_{void} is the volume fraction of the pores and $\kappa_{adsorbate}$ is the bulk thermal conductivity of each liquid. For HKUST-1, κ_{MOF} and F_{void} are estimated at 0.7 W/m·K and 70 %, respectively [18,39]. For liquid ethanol, water and methanol, $\kappa_{adsorbate}$ is assumed as 0.17, 0.60 and 0.20 W/m·K, respectively [40,41]. The measured thermal conductivities are lower than these estimates, which is only partly explained by liquid molecules scattering phonons in the HKUST-1. In addition, conduction through the liquid is lower than expected, possibly because although the liquids form a continuous network, there are constrictions that inhibit the flow of heat. One of the possibilities is when the liquid molecules are connected via sharp point contacts as explained in Ref. [42]. As shown in Fig.4.5-

(b), the authors described that when the molecules have a less contact area between each molecule during heat conduction (lower contact size ratio), the effective κ of the system in various crystal structures is lower than when they have a higher contact size ratio. The contact size ratio was defined by the authors as the ratio of the length of the contacted region ($2\cdot A$) to the diameter of each molecule ($2\cdot R$) as described in Fig.4.5-(a).

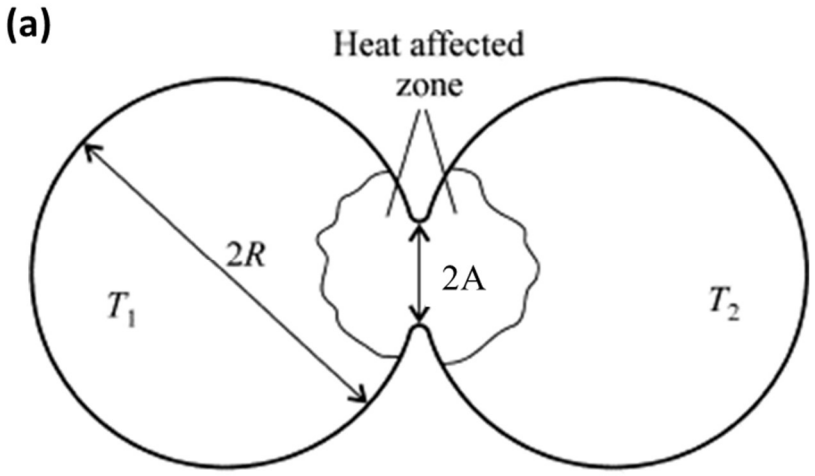

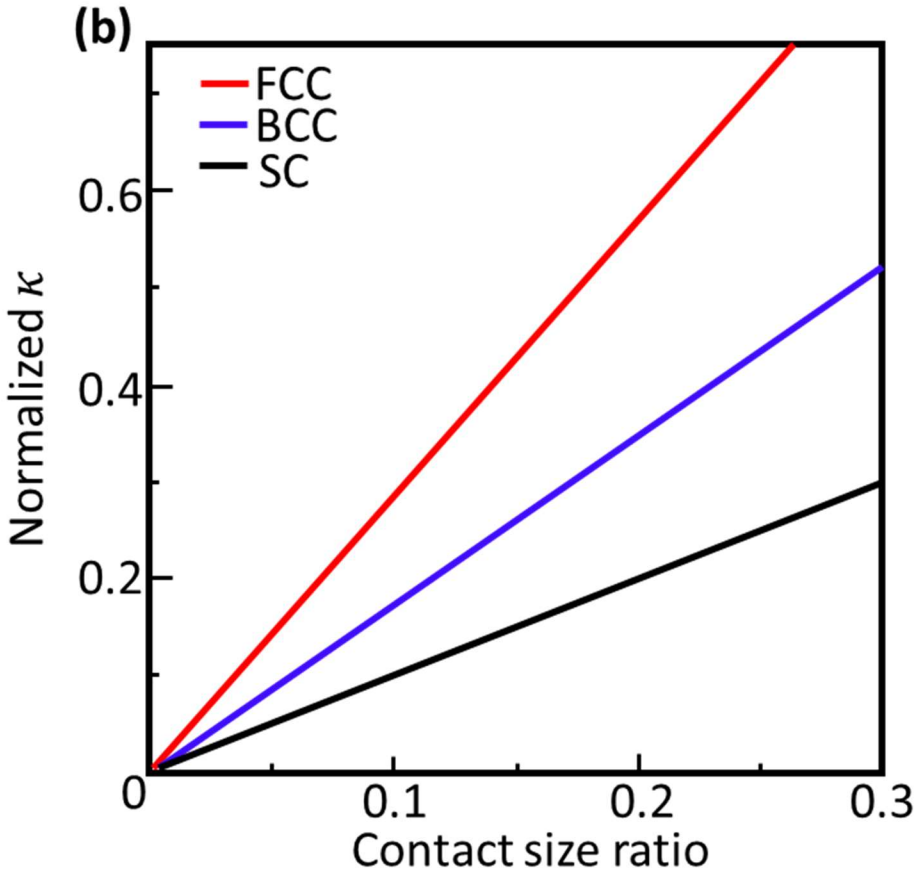

Fig.4.6. (a) An illustration of spherical molecules with a radius of R forming a neck with a contact length of 2A when connected together (b) The effective κ of different crystal structures (FCC : face-centered cubic, BCC : body-centered cubic, SC : simple cubic) as a function of contact size ratio (=A/R) [42]. Reprinted and adapted from, Vol. 46 (6) , A.V. Gusarov et al., *"Contact thermal conductivity of a powder bed in selective laser sintering,* 1103-1109, Copyright 2003, with permission from Elsevier.

Furthermore, the possible existence of thermal interface resistance between the adsorbate molecules and the MOF structure can explain why our experimental values are lower than the parallel channel-based effective medium theory values. If we use Hasselman-Johnson model

[46], a different effective medium theory-based model that considers the filler particle size and thermal interface resistance ($1/G$) between the filler and the matrix in a composite material, relevant G can be estimated to match with our experimental values. The corresponding G is 0.5 ± 0.4 ,800 ± 150 and 80 ± 20 MW/m^{2}K for ethanol, methanol and water respectively. While these values provide some insights, they may not represent accurate interfacial resistances because Hasselman-Johnson model is not a bicontinuous . Moreover, the adsorbed molecules are likely to affect the inherent κ of the MOF.

Because it is well known that HKUST-1 is very susceptible to moisture, the change in surface morphology in the water adsorption case shown in a red circled area in Fig. 4.7-(a) is not surprising [36,43–45]. However, complete disintegration of the HKUST-1 crystal is not observed. The methanol adsorbed HKUST-1 crystal, shown in Fig. 4.7-(b), did not show a change in surface features as HKUST-1 has been reported to be relatively stable in alcohols [37,38], but more surface damage than the water adsorption case such as cracks could be observed on the Au-Pt covered surface. The ethanol adsorbed crystal, shown in Fig. 4.7-(c), exhibited the most significant degree of change in surface features, much more appreciable than the methanol adsorption case, even though it was previously reported to be benign to the HKUST-1 crystal structure [38]. Hence, while the crystals' surface morphology is influenced significantly by the liquid alcohols, the structural-integrity has not changed as the previous report already confirmed structural integrity preserved before and after ethanol and methanol adsorption through X-ray diffraction (XRD) analysis [8].

(a)

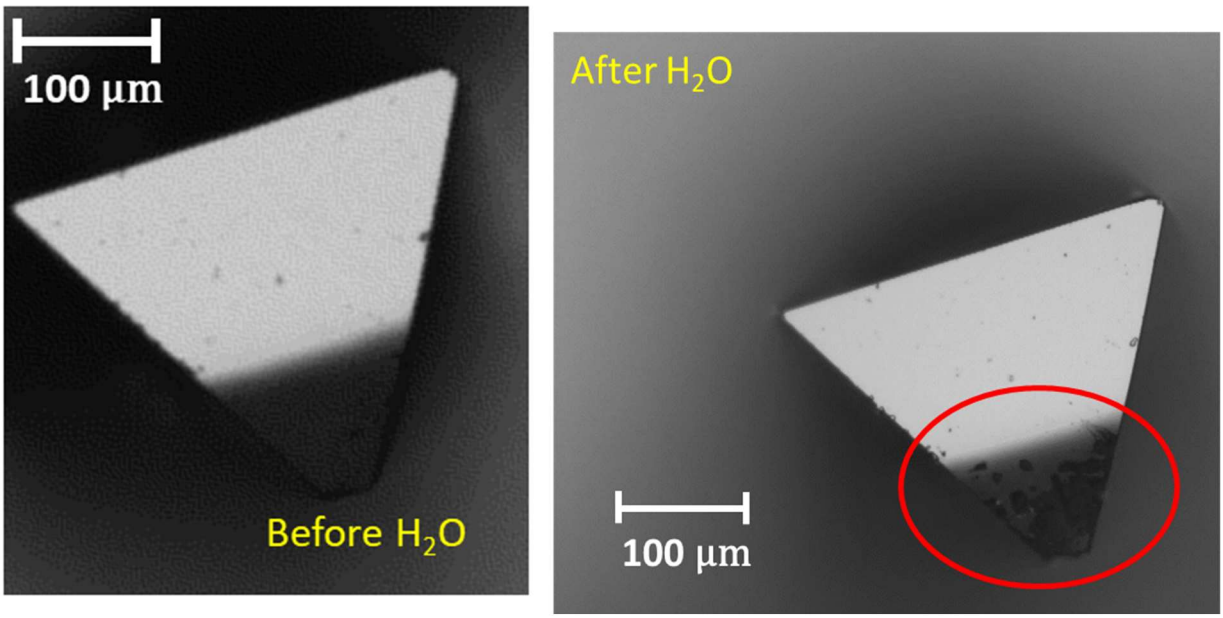
100 µm
Before H_2O
After H_2O
100 µm

(b)

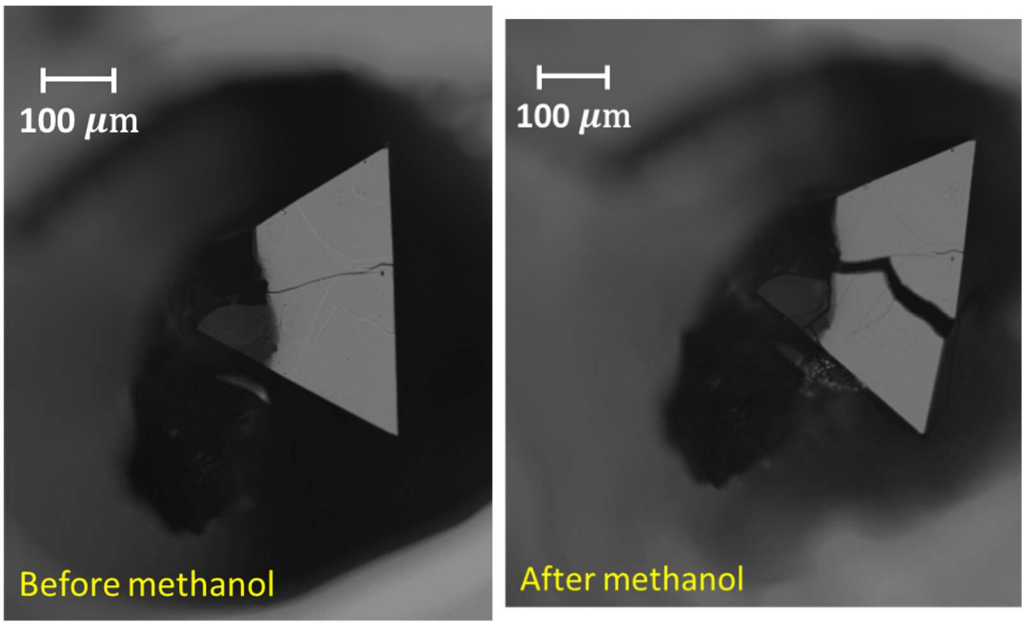
100 μm
Before methanol
100 μm
After methanol

(c)

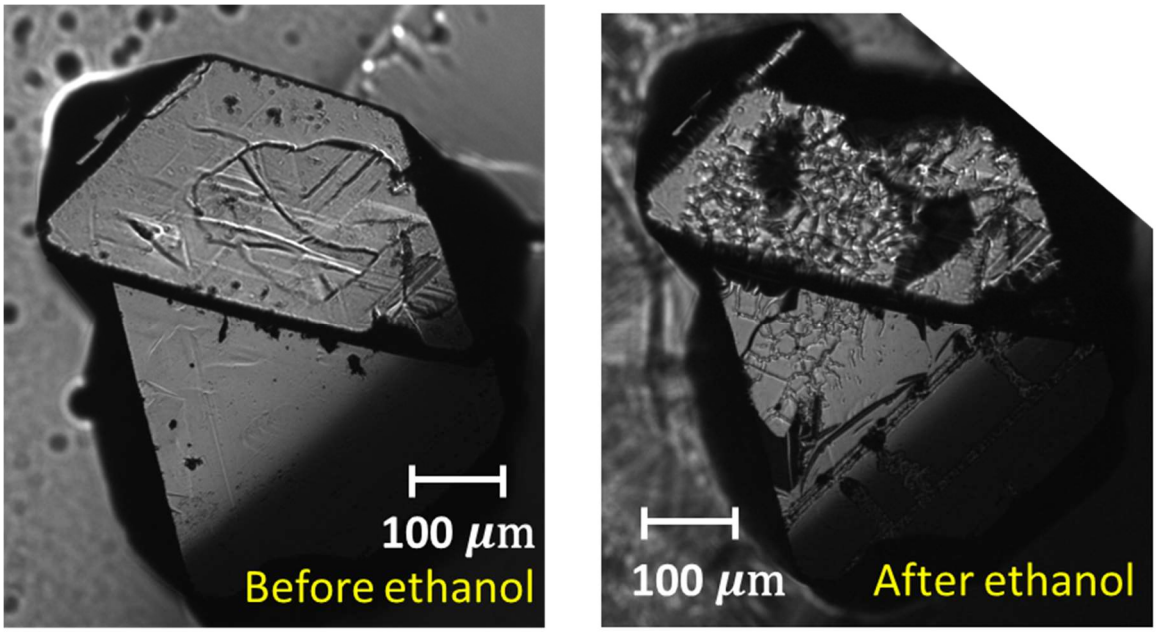

Fig. 4.7. Optical microscope images taken before and after (a) water adsorption (10X & 20X) (b) methanol adsorption (20X) and (c) ethanol adsorption (20X) occurred in HKUST-1 crystal samples. The red circle in (a) is for a visual aid.

The reason the ethanol and methanol adsorption cases exhibited lower κ than water adsorption case could be attributed to the lower κ in intrinsic ethanol and methanol liquids; 0.17 and 0.20 W/m·K in ethanol and methanol, respectively, as opposed to 0.60 W/m·K of water [40,41]. Moreover, the kinetic diameters of ethanol liquid molecules are the largest (4.7 Å), followed by methanol (3.6 Å) and water (2.7 Å) [43,44]. Being the largest, the ethanol molecules in HKUST-1 pores may scatter phonons more effectively than other smaller molecules. From these kinetic diameters, we can also estimate how many molecules would fit in the HKUST-1 pores. The average pore volume for the HKUST-1 has been reported as approximately 0.71 cc/g [48]. If we assume perfectly spherical liquid molecules for simplicity, there can be approximately 1.3×10^{22}, 2.9×10^{22}, and 6.89×10^{22} molecules per a gram of HKUST-1 for

ethanol, methanol and water, respectively. These different numbers of adsorbate molecules inside the MOF structure also could provide insights about the thermal behaviors of the MOF as more molecules may lead to more interfaces and sharp contacts between them.

4.5 Conclusions

In this study we experimentally measured thermal conductivity of the thermally activated pristine HKUST-1 MOF single crystal by using a non-contact optical FDTR technique. Then, a change in thermal conductivity as the crystal adsorbs different liquids (ethanol, methanol and water) is measured. We confirmed a significant decrease in thermal conductivity with full liquid adsorption, which suggests that phonons are more scattered by the liquid molecules occupying the crystal pores. The highest thermal conductivity reduction of 70 ± 9% is seen in the ethanol adsorbed sample, which can be attributed to the lowest thermal conductivity of intrinsic liquid ethanol and its largest kinetic diameter.

4.6 Supporting Information

4.6.1 Table 4.S1 below shows fitting parameters that are used for fitting the experimental phase lags to the analytically calculated values. “Fitting” indicates that they are the unknown fitting parameters.

Table 4.S1. Material properties used for fitting in each case

Layer materials	Thermal conductivity (W/m·K)	Heat capacity (J/kg·K)	Density (g/cm^3)	Length (m)
Au (top)	Fitting	126 ± 3	19.3 ± 0.4	(30 ± 2) E -9
Pt	Fitting	133 ± 2	21.4 ± 0.1	(20 ± 2) E -9
Activated (crystal)	Fitting	720 ± 7	1 ± 0.1	(150 ± 10) E -6
Ethanol (crystal)	Fitting	$1{,}430 \pm 140$	1.43 ± 0.1	(150 ± 10) E -6
Methanol (crystal)	Fitting	$1{,}430 \pm 140$	1.44 ± 0.1	(150 ± 10) E -6
Water (crystal)	Fitting	$2{,}290 \pm 230$	1.58 ± 0.1	(150 ± 10) E -6

Only those data sets that show relatively similar κ in the Au – Pt layer ($\pm$ 5%) in fitting with the reference Au – Pt layer sample deposited on a glass substrate are chosen. The reference sample's κ is measured by using Wiedemann Franz law. For Au-Pt layer, the same thermal conductivity is assumed between Au and Pt as both are highly conductivity metals yet very thin. The actual thickness of the transducer layer is measured using X-ray reflectivity (XRR) technique and that of the crystal is assumed from the average crystal size from optical microscope images. For the density and heat capacity values of the activated HKUST-1 crystal before liquid adsorption, published experimental values are used [39] while theoretically calculated values are used for each liquid adsorption case. The uncertainties in heat capacity and density in HKUST crystal are set conservatively at 10% due to a lack of experimental data available for these properties.

4.6.2 Thickness analysis

The X-ray reflectivity (XRR) fit agreed very well with the original data as presented in Fig.4.S1. The fitted result indicated that the Pt thickness is 21 nm and Au thickness is 30 nm. When these thicknesses changed by 2 nm, the quality of fit worsened appreciably.

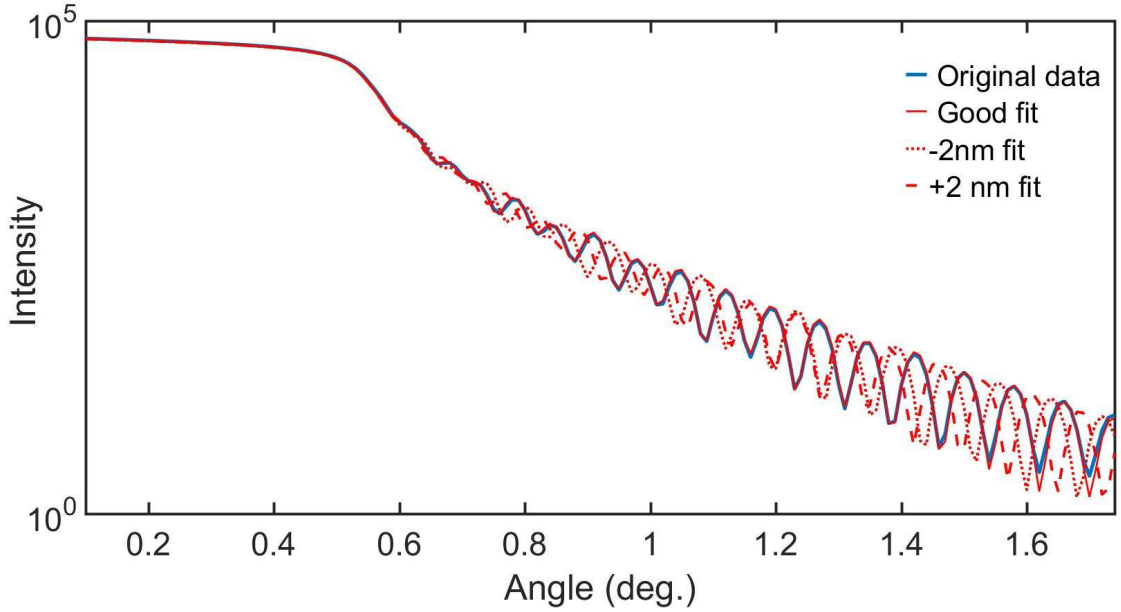

Fig.4.S1. The XRR thickness analysis result. The -2 nm and +2 nm lines show the sensitivity in fits with ± 2 nm change in the Au layer.

4.6.3 Sensitivity analysis

(a)

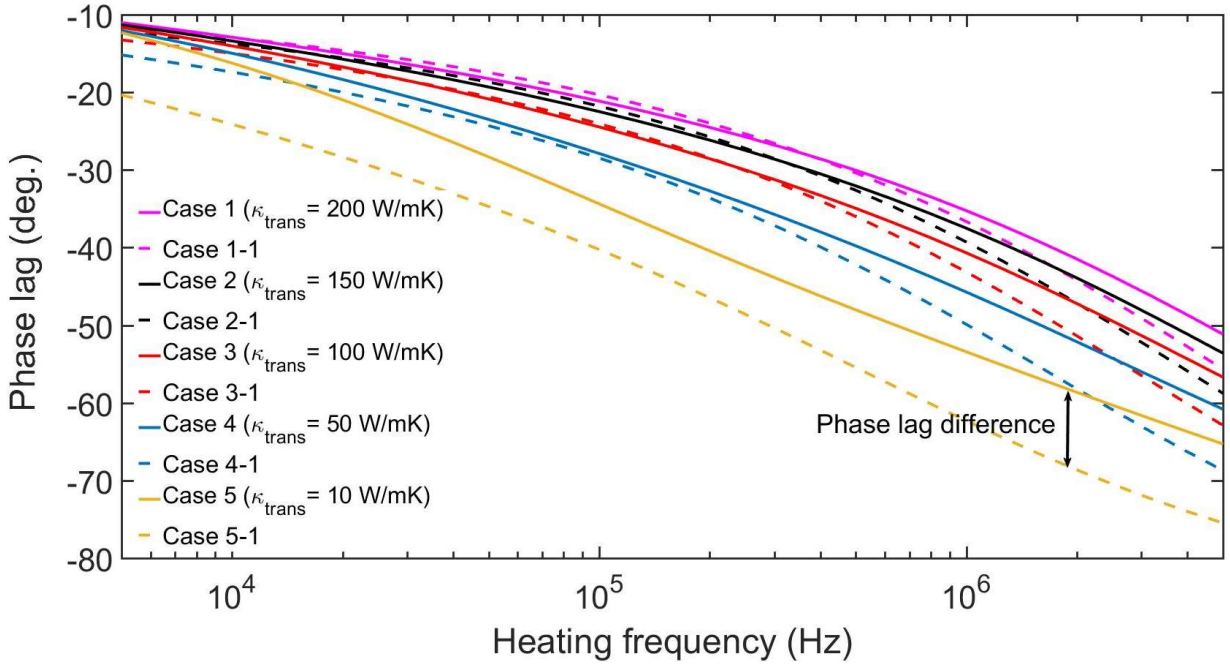

(b)

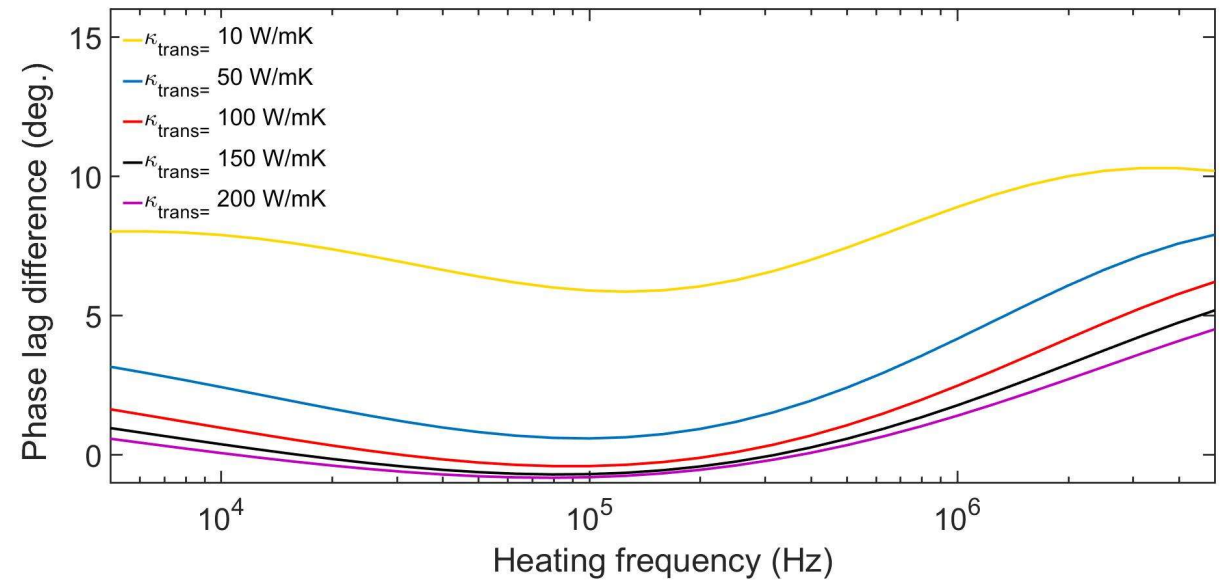

Fig.4.S2. (a) Analytically calculated phase lags as a function of heating frequency for different κ_{trans} when the MOF thermal conductivity changed from 0.7 W/m·K (solid lines) to 0.1 W/m·K

(dashed lines). (b) The difference in phase lags represented with the solid and dashed lines as a function of heating frequency.

The phase lags as a function of heating frequency are analytically calculated when the thermal conductivity of MOF crystal is assumed to be 0.7 W/m·K and 0.1 W/m·K for different top transducer layer thermal conductivities (κ_{trans}). The calculation results are shown in Fig.4.S2-(a). The transducer layer thermal conductivity ranged between 10W/m·K (Case 5) and 200W/m·K (Case 1) where the solid lines represent the 0.7 W/m·K case and the dashed lines represent the 0.1 W/m·K case. Fig.4.S2-(b) shows the difference in phase lags between the higher and lower MOF thermal conductivity cases for different κ_{trans} as a function of heating frequency. It is clear that the lower κ_{trans} yields a higher phase lag difference, which is equivalent to higher sensitivity for measuring the thermal properties of MOF crystals.

4.6.4 Measurements data table

While each crystal under the same loading conditions yielded thermal conductivity values that are not significantly deviated from one another, some of the best-fit yielding data sets that also meet our selection criteria described in the main text based on the fitted $\kappa_{trans.}$ are chosen and presented in Table 4.S2. Different numbers in crystals and data points in the second and third columns mean that the data collection is performed on different crystals and multiple spots on the crystal. The uncertainties in each data point in the last column resulted from the propagation of uncertainties in material properties used for fitting. Fig.4.S3 shows a histogram of all the measurement results of the activated HKUST-1 crystal samples to show that the whole data sets

did not yield severely scattered κ. This data set represents a total of 8 crystals and 21 measurement spots.

Table 4.S2. Selected measured κ of HKUST-1 crystals under different conditions

Activated HKUST	Crystal 1	Data point 1	0.72 ± 0.27 W/m·K
		Data point 2	0.69 ± 0.26 W/m·K
		Data point 3	0.69 ± 0.27 W/m·K
	Crystal 2	Data point 1	0.75 ± 0.24 W/m·K
		Data point 2	0.61 ± 0.25 W/m·K
Methanol	Crystal 1	Data point 1	0.31 ± 0.24 W/m·K
		Data point 2	0.28 ± 0.26 W/m·K
		Data point 3	0.25 ± 0.23 W/m·K
		Data point 4	0.34 ± 0.33 W/m·K
Ethanol	Crystal 1	Data point 1	0.15 ± 0.08 W/m·K
		Data point 2	0.16 ± 0.08 W/m·K
Water	Crystal 1	Data point 1	0.19 ± 0.09 W/m·K
		Data point 2	0.24 ± 0.09 W/m·K

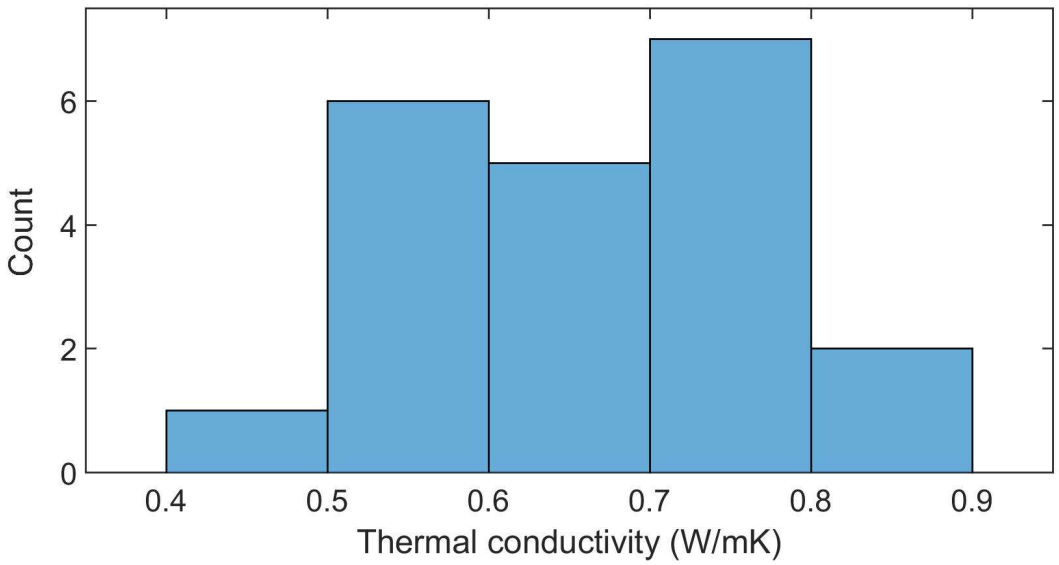

Fig.4.S3. A histogram of thermal conductivity measurements of HKUST-1 crystals after thermal activation. This data set represents a total of 8 crystals and 21 measurement spots.

[1] K.Y. Foo and B.H. Hameed: *Chem. Eng. J.*, 2010, vol. 156, pp. 2–10.

[2] Stephen Brunauer and L. E. Copeland: in *Symp. Prop. Surfaces*, ASTM International, 100 Barr Harbor Drive, PO Box C700, West Conshohocken, PA 19428-2959, 1963, pp. 59-59–21.

[3] Loubna Nouri, Ilhem Ghodbane, Oualid Hamdaoui, and Mahdi Chiha: *J. Hazard. Mater.*, 2007, vol. 149, pp. 115–25.

[4] Ahmed Rezk, Raya Al-Dadah, Saad Mahmoud, and Ahmed Elsayed: *Int. J. Heat Mass Transf.*, 2012, vol. 55, pp. 7366–74.

[5] Jian-Rong Li, Ryan J. Kuppler, and Hong-Cai Zhou: *Chem. Soc. Rev.*, 2009, vol. 38, p. 1477.

[6] Filipe A. Almeida Paz, Jacek Klinowski, Sérgio M. F. Vilela, João P. C. Tomé, José A. S. Cavaleiro, and João Rocha: *Chem. Soc. Rev.*, 2012, vol. 41, pp. 1088–1110.

[7] Rob Ameloot, Frederik Vermoortele, Wim Vanhove, Maarten B. J. Roeffaers, Bert F. Sels, and Dirk E. De Vos: *Nat. Chem.*, 2011, vol. 3, pp. 382–87.

[8] Nak Cheon Jeong, Bappaditya Samanta, Chang Yeon Lee, Omar K. Farha, and Joseph T. Hupp: *J. Am. Chem. Soc.*, 2012, vol. 134, pp. 51–54.

[9] Myunghyun Paik Suh, Hye Jeong Park, Thazhe Kootteri Prasad, and Dae Woon Lim: *Chem. Rev.*, 2012, vol. 112, pp. 782–835.

[10] Wilarachchige D C B Gunatilleke, Kaya Wei, Zheng Niu, Lukasz Wojtas, George Nolas, and Shengqian Ma: *Dalt. Trans. Commun. Cite This Dalt. Trans*, 2017, vol. 46.

[11] B.L. Huang, Z. Ni, A. Millward, A.J.H. McGaughey, C. Uher, M. Kaviany, and O. Yaghi: *Int. J. Heat Mass Transf.*, 2007, vol. 50, pp. 405–11.

[12] D. Liu, J.J. Purewal, J. Yang, A. Sudik, S. Maurer, U. Mueller, J. Ni, and D.J. Siegel: *Int. J. Hydrogen Energy*, 2012, vol. 37, pp. 6109–17.

[13] Lei Sun, Bolin Liao, Dennis Sheberla, Daniel Kraemer, Jiawei Zhou, Eric A. Stach, Dmitri Zakharov, Vitalie Stavila, A. Alec Talin, Yicong Ge, Mark D. Allendorf, Gang Chen, François Léonard, and Mircea Dincă: *Joule*, 2017, vol. 1, pp. 168–77.

[14] Boya Cui, Cornelius O. Audu, Yijun Liao, SonBinh T. Nguyen, Omar K. Farha, Joseph T. Hupp, and Matthew Grayson: *ACS Appl. Mater. Interfaces*, 2017, vol. 9, pp. 28139–43.

[15] Jungseok Chae, Sangmin An, Georg Ramer, Vitalie Stavila, Glenn Holland, Yohan Yoon, A. Alec Talin, Mark Allendorf, Vladimir A. Aksyuk, and Andrea Centrone: *Nano Lett.*, 2017, vol. 17, pp. 5587–94.

[16] Kristopher J. Erickson, François Léonard, Vitalie Stavila, Michael E. Foster, Catalin D. Spataru, Reese E. Jones, Brian M. Foley, Patrick E. Hopkins, Mark D. Allendorf, and A. Alec Talin: *Adv. Mater.*, 2015, vol. 27, pp. 3453–59.

[17] Hasan Babaei, Alan J. H. McGaughey, and Christopher E. Wilmer: *Chem. Sci.*, 2017,

vol. 8, pp. 583–89.

[18] Hasan Babaei and Christopher E. Wilmer: *Phys. Rev. Lett.*, 2016, vol. 116, p. 025902.

[19] Luping Han, Makenzie Budge, and P. Alex Greaney: *Comput. Mater. Sci.*, 2014, vol. 94, pp. 292–97.

[20] Bin Mu and Krista S. Walton: *J. Phys. Chem. C*, 2011, vol. 115, pp. 22748–54.

[21] Nicholas C. Burtch, Himanshu Jasuja, and Krista S. Walton: *Chem. Rev.*, 2014, vol. 114, pp. 10575–612.

[22] Jaeyeon Bae, Jin-Woo Jung, Hyo Yul Park, Chang-Hee Cho, and Jinhee Park: *Chem. Commun.*, 2017, vol. 53, pp. 12100–103.

[23] Koichi Momma and Fujio Izumi: *J. Appl. Crystallogr.*, 2011, vol. 44, pp. 1272–76.

[24] Chui, Lo, Charmant, Orpen, and Williams: *Science*, 1999, vol. 283, pp. 1148–50.

[25] Hartmut Gliemann and Christof W?ll: *Mater. Today*, 2012, vol. 15, pp. 110–16.

[26] Stefan K. Henninger, Felix Jeremias, Harry Kummer, and Christoph Janiak: *ChemInform*, 2012, vol. 43, p. no-no.

[27] Ohad Fleker, Arie Borenstein, Ronit Lavi, Laurent Benisvy, Sharon Ruthstein, and Doron Aurbach: *Langmuir*, 2016, vol. 32, pp. 4935–44.

[28] Kun-Yi Andrew Lin and Yu-Tsung Hsieh: *J. Taiwan Inst. Chem. Eng.*, 2015, vol. 50, pp. 223–28.

[29] David G. Cahill: *Rev. Sci. Instrum.*, 2004, vol. 75, pp. 5119–22.

[30] Keith T Regner, Daniel P Sellan, Zonghui Su, Cristina H Amon, Alan J H McGaughey, and Jonathan A Malen: *Nat. Commun.*, 2013, vol. 4, p. 1640.

[31] Jonathan A. Malen, Kanhayalal Baheti, Tao Tong, Yang Zhao, Janice A. Hudgings, and Arun Majumdar: *J. Heat Transfer*, 2011, vol. 133, p. 081601.

[32] Zhou Kui and S. Chaemchuen: *International Journal of Environmental Science and Development*, IACSIT Press, 2017.

[33] A. Nalaparaju, X. S. Zhao, and J. W. Jiang: *Energy Environ. Sci.*, 2011, vol. 4, p. 2107.

[34] Marta Mon, Rosaria Bruno, Jesus Ferrando-Soria, Donatella Armentano, and Emilio Pardo: *J. Mater. Chem. A*, 2018, vol. 6, pp. 4912–47.

[35] † and Jeffery A. Greathouse* and Mark D. Allendorf‡: 2006.

[36] Michela Todaro, Gianpiero Buscarino, Luisa Sciortino, Antonino Alessi, Fabrizio Messina, Marco Taddei, Marco Ranocchiari, Marco Cannas, and Franco M. Gelardi: *J. Phys. Chem. C*, 2016, vol. 120, pp. 12879–89.

[37] Felix Jeremias, Dominik Frö, Christoph Janiak, and Stefan K Henninger: *New J. Chem. New J. Chem*, 1846, vol. 38, pp. 1846–52.

[38] J Raziel Álvarez, Elí Sánchez-González, Eric Pérez, Emilia Schneider-Revueltas, Ana Martínez, Adriana Tejeda-Cruz, Alejandro Islas-Jácome, Eduardo González-Zamora, and Ilich A Ibarra: *Dalt. Trans.*, 2017, vol. 46.

[39] Daniele Ongari, Peter G Boyd, Senja Barthel, Matthew Witman, Maciej Haranczyk, and Berend Smit: n.d.

[40] G.X. Chen, M.H. Hong, B. Lan, Z.B. Wang, Y.F. Lu, and T.C. Chong: *Appl. Surf. Sci.*, 2004, vol. 228, pp. 169–75.

[41] R M Mostafizur, U Bhuiyan, R Saidur, and A R Abdul Aziz: n.d.

[42] A.V. Gusarov, T. Laoui, L. Froyen, and V.I. Titov: *Int. J. Heat Mass Transf.*, 2003, vol. 46, pp. 1103–9.

[43] Tsolmon Borjigin, Fuxing Sun, Jinlei Zhang, Kun Cai, Hao Ren, and Guangshan Zhu: *Chem. Commun. Chem. Commun*, 2012, vol. 48, pp. 7613–15.

[44] Angelo (Angelo Bruno) Basile and Francesco Dalena: *Methanol Science and Engineering*, n.d.

[45] Di Wu, Xiaofeng Guo, Hui Sun, and Alexandra Navrotsky: *J. Phys. Chem. C*, 2016, vol. 120, pp. 7562–67.

[46] D.P.H. Hasselman and Lloyd F. Johnson: J. Compos. Mater., 1987, vol. 21, pp. 508–15.

[47] Miyuki Hashimoto, Satoshi Okajima, Toshihiro Kondo, Kenji Hara, and Wang-Jae Chun: Commun. Electrochem., 2014, vol. 82, pp. 335–37.

[48] Jarad A. Mason, Mike Veenstra, and Jeffrey R. Long: *Chem. Sci.*, 2014, vol. 5, pp. 32–51.

Concluding remarks

We are able to accurately measure thermal properties of different material systems using the optical FDTR technique. In Chapter 2, we first present the measurement results of thermal conductance at the interface, *G*, between Au metal and Al_2O_3 dielectric layers, which reflects the actual HAMR NFT material system. By inserting metal adhesion layers to bridge dissimilar phonon properties between the Au and Al_2O_3, specifically to have better phonon density of states overlap with Al_2O_3, we attempt to enhance *G*. We use Cu and Cr layers in this study, which results in two-fold and four-fold enhancement in *G.* The thickness that is required to achieve such enhancement is approximately 1 nm, suggesting that only a little amount is necessary to enhance thermal properties. The interdiffusion effect between Au and the interested Cu is also studied to see how the Cu adhesion layer inserted between Au and Al_2O_3 could affect the *G* behavior. We find that at higher annealing temperatures, we get intermixing between Au and Cu due to promoted interduffison between them. This results in depletion of Cu atoms at the metal-dielectric interface, which lowers *G* finally.

In Chapter 3, we present that the mechanical bonding approach is successful to create intended nano-gap structures to experimentally probe the near-field thermal radiative effect. To fabricate thermomehanically robust thin gap structures, we run design analysis to see how much of the top membrane will deflect when the top structure is subjected to certain pressure for various gap size configurations. Also, thermal sensitivity analysis to maximize our sensitivity to the near-field radiative effect is conducted. The samples created based on these design considerations show reasonable FDTR fitted values, but with very large uncertainties. These large uncertainties result from the high sensitivity of our data to variations in our fitting

parameters. Thus, we come up with a differential fitting analysis to fit for the phase lag differences in two data sets. This successfully reduces the large uncertainties, and the fitted values match well with the expected values. We also observe enhancement in h_{gap} with the decreasing gap thickness and the matching material case, which clearly suggests that we have measured the near-field thermal radiative effect.

In Chapter 4, we present the reduction in κ in HKUST-1 MOF single crystals through liquid adsorption. The FDTR-obtained κ when the HKUST-1 is fully activated matches well with the reported calculated value. Following the full adsorption in ethanol, methanol and water liquids, we observe the reduction in κ. This suggests that phonons are effectively scattered due to liquid adsorbate molecules inside the crystal structure. The experimental values are lower than the effective medium theory's expected values, which assumes parallel heat channel with respect to heat flow. This could be due to liquid adsorbate molecules populating the HKUST-1 MOF pores by forming sharp point contacts or the possible existence of thermal interface resistance between the adsorbate-containing pores and the MOF structure.